
[All ETDs from UAB](#)

[UAB Theses & Dissertations](#)

2019

Connection Strengthening Scheme For Coastal Bridges Under Hurricane Induced Surge And Wave Load Using C-Iepm

Li He

University of Alabama at Birmingham

Follow this and additional works at: <https://digitalcommons.library.uab.edu/etd-collection>

Recommended Citation

He, Li, "Connection Strengthening Scheme For Coastal Bridges Under Hurricane Induced Surge And Wave Load Using C-Iepm" (2019). *All ETDs from UAB*. 1905.

<https://digitalcommons.library.uab.edu/etd-collection/1905>

This content has been accepted for inclusion by an authorized administrator of the UAB Digital Commons, and is provided as a free open access item. All inquiries regarding this item or the UAB Digital Commons should be directed to the [UAB Libraries Office of Scholarly Communication](#).

CONNECTION STRENGTHENING SCHEME FOR COASTAL BRIDGES UNDER
HURRICANE INDUCED SURGE AND WAVE LOAD USING C-IEPM

by

LI HE

CHRISTOPHER WALDRON, COMMITTEE CHAIR
ABDULLAHI SALMAN
VIRGINIA SISIPIKU
VINOY THOMAS
NASIM UDDIN

A DISSERTATION

Submitted to the graduate faculty of The University of Alabama at Birmingham,
in partial fulfillment of the requirements for the degree of
Doctor of Philosophy

BIRMINGHAM, ALABAMA

2019

Copyright by
Li He
2019

RESEARCH ON CONNECTIONS STRENGTHENING SCHEME FOR COASTAL BRIDGE UNDER HURRICANE INDUCED SURGE AND WAVE LOAD USING C-IEPM

LI HE

CIVIL, CONSTRUCTION AND ENVIRONMENTAL ENGINEERING

ABSTRACT

Considerable damage to the highway bridge system in the Gulf Coast area was observed during the Hurricane Katrina disaster, of which the primary failure mode, caused primarily by the storm-induced loading, is believed to be the superstructure-substructure connection failure which caused further unseating and drifting of the decks. A new Carbon-fiber Interfacial Epoxy-Polyurea Matrix (C-IEPM) composite is investigated as a potential retrofit option for vulnerable girder-to-cap connection-details in coastal highway bridges. Six scaled concrete girders were tested using a modified simulated storm surge and slamming wave force function, derived using regional maps for a 100-year return-period Hurricane Katrina. Two girders, designed using current AASHTO field connection-details, failed catastrophically (concrete shear failure) in less than one-half load cycle. The CF/E-strengthened girder, failing in less than one load cycle, experienced severe damage to its girder-to-cap connection, including fiber and epoxy matrix breakage, delamination, unsustainable girder-end rotations, and transient hysteresis. However, after 12 load cycles, the C-IEPM-strengthened girder, providing substantial energy transferability (material damping) through its connection-details, experienced only local cracking.

For a more in-depth understanding of the material C-IEPM and improving material properties, a series of material investigations were conducted in a coupon-scale and nano-scale. Using Generalized Maxwell models, the viscoelastic properties of epoxy, polyurea, and C-IEPM are predicted, and results are verified using Dynamic Mechanical Analysis

(DMA). The Maxwell models for x-DC_{EP}I, as a function of t_c , are used in a finite element analysis (ABAQUS) to control performance of dynamically loaded structures.

Atomic Force Microscopy (AFM) and Scanning Electron Microscopy (SEM) elucidate interfacial nanoscale morphology and chemical structure via reaction kinetics of curing epoxy (as a function of time, t_c) and fast-reacting (pre-polymerized) polyurea. Nano-Infrared Spectroscopy (nano-IR) spectra, per non-negative matrix factorization (NMF) analysis, reveal that simultaneous presence of characteristic epoxy and polyurea vibrational modes, within a nanoscale region, along with unique IEPM characteristics and properties following thermomechanical analysis (TMA) and dynamic mechanical analysis (DMA), indicates chemical bonding, enabling IEPM reaction kinetics, as a function of t_c , to control natural bond vibrations and type / distribution of interfacial chemical bonds and physical mixtures, likely due to the bond mechanism between –NCO in polyurea, and epoxide and –NH₂ in epoxy hardener (corresponding to characteristic absorption peaks in nano-IR results), leading to enhanced IEPM quality (fewer defects/ voids). Test results of ballistics-resistant panels, integrated with thin intermediate layers of x-IEPM-b- t_c , confirm that lower t_c significantly enhances loss modulus (\propto material damping and per DMA) in impact dynamics environments.

Keywords: Hurricane; Coastal Bridge; AASHTO connection-details; FRP; Energy transferability; Polyurea; IEPM

ACKNOWLEDGMENTS

This dissertation would not have been finished without the help of many people. First of all, I would like to express my sincere gratitude to my former graduate advisor Dr. Thomas Attard for his substantial support and guidance. Dr. Thomas Attard was serious and enthusiastic in his research, which motivated me to work hard on this research project.

Most importantly, I would like to express my sincere appreciation to my Dr. Christopher Waldron, Dr. Fouad Fouad, and Dr. Lori McMahon, for assisting with the difficulties I met during my final semester. At the same time, I would like to appreciate my graduate committee members Dr. Virginia P. Sisiopiku, Dr. Vinoy Thomas, Dr. Abdullahi Salman and Dr. Nasim Uddin for taking time to review the dissertation and making valuable comments.

Special thanks should also be given Dr. Hongyu Zhou's support and guidance, who also provided his facility in UAH structural lab to conduct structure tests. I would also like to acknowledge Dr. Alison Pawlicki, Dr. Yangyang Wang, Dr. Shawn Reeves, Dr. Kunlun Hong, Dr. Alexei Belianinov, Olga Ovchinnikova at Center for Nanophase Materials Sciences (CNMS) in Oak Ridge National Laboratory (ORNL) and Dr. Weixing Sun for the help of access and training the material testing equipment.

I would like to thank UAB and thank all the members in the department of civil, construction and environmental engineering for providing a nice study and research environment. Thanks Ms. Jennifer Vinson, Ms. Mischell Massey, Mr. Thomas Foley and Mr. Richard Hawkins for their help.

Special appreciation should also be given to my friends, Adam Brooks and Dominic Hanna, who contributed a lot of effort and time helping build the concrete girders related to this research. I would also like to thank Zhenglai Shen, Babak Salarieh, Qian Huang, and Hector R. Orozco Avalos, Zhenhua Shi, Chenjun Tan for the help of the experimental work.

Finally, I would like to give my special gratitude to my wife, Zhenyu Lai, for her constant support, encouragement, and constant sacrifice, and to my family for all their good wishes and blessings, without them, I cannot achieve anything.

TABLE OF CONTENTS

ABSTRACT	iii
ACKNOWLEDGMENTS	v
LIST OF TABLES	ix
LIST OF FIGURES	xi
LIST OF ABBREVIATIONS	xv
INTRODUCTION	1
Background and Existing Problems.....	1
Hurricane induced surge and wave loads on bridges.....	3
Existing connections and its failure modes.....	5
Current solutions to the connection problems for coastal bridges.....	8
Carbon fiber reinforce Interfacial Epoxy / Polyurea Matrix (C-IEPM)	11
The objective of the research	12
Organization of Content.....	13
INTEGRATING ENERGY TRANSFERABILITY INTO THE CONNECTION-DETAIL OF COASTAL BRIDGES USING REINFORCED INTERFACIAL EPOXY-POLYUREA REACTION MATRIX COMPOSITE.....	15
VISCOELASTICITY OF CHEMICALLY BONDED INTERFACIAL EPOXY-	

POLYUREA MATRIX PER MIGRATION OF EPOXY SPECIES VIA CURING TIME PARAMETER.....	62
LINKING NANOSCALE CHEMICAL CHANGES TO BULK MATERIAL PROPERTIES IN IEPM POLYMER COMPOSITES SUBJECT TO IMPACT DYNAMICS	80
SUPPORTING INFORMATION.....	123
CONCLUSIONS.....	132
LIMITATION OF THE RESEARCH	136
LIST OF GENERAL REFERENCES	137
APPENDIX: MODIFIED DOUGLASS FUNCTION.....	139

LIST OF TABLES

Table	Page
INTEGRATING ENERGY TRANSFERABILITY INTO THE CONNECTION-DETAIL OF COASTAL BRIDGES USING REINFORCED INTERFACIAL EPOXY- POLYUREA REACTION MATRIX COMPOSITE	
Table 1. Comparison of AASHTO type III girder used in the field and $1/4$ - scale test-girder	26
Table 2. Design details and cyclic load-response features of the tested specimen	30
Table 3. Rotation angle of CF/ E and C-IEPM at the peak of each cycle.....	41
Table 4. Accumulated energy after the i th cycle (summed area under each hysteresis curve) for CF/E TG and C-IEPM_2 TG.....	47
Table 5. Fracture energy calculated from coupon-scale fracture tests	53
VISCOELASTICITY OF CHEMICALLY BONDED INTERFACIAL EPOXY- POLYUREA MATRIX PER MIGRATION OF EPOXY SPECIES VIA CURING TIME PARAMETER	
Table 1. DMA Test Specimen Details.....	66
Table 2. Prony Series Fitting Target (DMA Measured Data)	69
Table 3. Prony Series Parameters.....	70
LINKING NANOSCALE CHEMICAL CHANGES TO BULK MATERIAL PROPERTIES IN IEPM POLYMER COMPOSITES SUBJECT TO IMPACT DYNAMICS	
Table 1. Characteristic IR peaks of twelve points in 0-IEPM-0 in Figure 1.....	90
Table 2. Test results of C-IEPM-b- t_c ballistics-resistant panels; caliber range: .22LR to .44 Magnum.....	108

Table 3. Ballistics test results for Test Programs A and B.....	112
Table S1. Possible IEPM chemical reactions: curing epoxy / polyurea (pre-polymerized)	122
Table S2. Specimen names and corresponding parameters.....	124
Table S3. Five caliber-rated bullets used for ballistics-impact testing on x-IEPM-b- t_c	127

LIST OF FIGURES

Figure	Page
INTRODUCTION	
Figure 1. Typical ‘anchored’ spans: The underside of the I-10 East bay- way	6
Figure 2. Threaded inserts pulled out of girder bottom bulb.....	7
Figure 3. Spall and bent anchor bolts and concrete rupture at the end of bent cap	7
Figure 4. Damaged clip angles remaining after girders moved laterally.....	8
Figure 5. Post Katrina connection design.....	9
Figure 6. AASHTO Type III girder connections.....	10
Figure 7. (a) Connection that increases the lateral and uplift capacity; (b)shear block type connection; (c)connection to increase span continuity.....	10
INTEGRATING ENERGY TRANSFERABILITY INTO THE CONNECTION-DETAIL OF COASTAL BRIDGES USING REINFORCED INTERFACIAL EPOXY- POLYUREA REACTION MATRIX COMPOSITE	
Figure 1. (a) IEPM polymerization comprised of covalent bonds between polar -(NCO) and -(NH ₂)-epoxy moieties, and epoxide functional groups; and (b) curing reaction of epoxy	22
Figure 2. End view of AASHTO girders: (a) in the field; and (b) in the lab (dimension in mm).....	25
Figure 3. (a) Pre-Katrina connection-details; (b) Post-Katrina connection-details; and (c) options for strengthening existing mechanical connection-details using C-IEPM and CF/E.....	25
Figure 4. CF/E procedure for retrofitting the mechanical connection-detail in concrete girders, showing (a) sequential fiber lay-up; (b) carbon-fiber applied to a girder-end that has no existing mechanical connections; (c) final CF/E lay-up; and (d) CF/E applied around mechanical connections (note: following CF/E lay-up, C-IEPM may be manufactured by spraying polyurea to the wet (curing) epoxy surfaces in (c) and (d))	27
Figure 5. Laboratory test set-up, showing (a) actuator force applied to the test girder via rigid steel beam connected to the girder at three points;	

(b) profile view of the actuator loading angle; (c) J-plate; and (d) Modified (lab-scale) Hurricane Katrina wave forcing function produced by the actuator (red) that models the desired theoretical wave load according to the modified Douglass function.....	28
Figure 6. Force (mid-span) time-history of cycle 1 for the six test girders (TG).....	33
Figure 7. Dynamic response of Pre-Katrina and Post-Katrina connection.....	35
Figure 8. Shear failure modes of (a) and (b) Pre-Katrina TG; and (c) and (d) Post Katrina TG where ductile behavior of through-bolts allow maximum force of 88.2 kN to be recovered until concrete fails in shear	35
Figure 9. Comparison of force-displacement behavior of Pre-Katrina TG (as-is) and test girder 2 (post-Katrina).....	37
Figure 10. Actuator force-time history of C-IEPM_0 and C-IEPM_1.....	39
Figure 11. (a) Depiction of connection-detail strengthening system, comprised of either C-IEPM or CF/E composite and mechanical connectors joining the concrete girder and cap-beam; (b and c) Shear failure observed in C-IEPM (C-IEPM_0 TG); (d) concrete shear failure at non-mechanically connected left girder-end (cap-beam) of C-IEPM_1 TG; (e) C-IEPM shear failure at non-mechanically connected girder-end in C-IEPM_1 TG.....	40
Figure 12. Force time-histories of C-IEPM_2 TG at four loading cycle.....	42
Figure 13. (a) and (b) Damage observed in CF/E TG, showing that the connection-details fail at multiple locations, exhibiting fiber breakage, CF/ E delamination, concrete shear failure (at the locations of threaded inserts in the girder), and yielding of threaded anchor bolts (in the inserts); and (c) and (d): Local damage in C-IEPM_2 TG after 12 load cycles, seen only on one girder-end.....	44
Figure 14. (a, b) Hystereses of C-IEPM_2 TG and CF/E TG, where material damping in IEPM helps to stabilize the response in C-IEPM_2 TG after 3 or 4 cycles, thus preserving girder integrity and minimizing the service limit state (to local damage / cracking); (c) a comparison of peak mid-span girder deflections, per cycle, showing that C-IEPM_2 TG quickly stabilizes (constant) while CF/E TG deflections, without a substantial damping mechanism, consistently increase until sudden disengagement; and (d) Displacement recovered per cycle (%), calculated at end of cycle	

relative to gross cycle displacement.....	46
Figure 15. (a) Illustration of energy dissipated per cycle, i and $i+1$; and (b) Distinction of actual and recovered energy.....	50
Figure 16. Energy dissipation (J) and recovery per cycle of CF/E TG and C-IEPM_2 TG.....	50
Figure 17. Compact Tensile (CT) test load-displacement curves of coupon-scaled structures: (a) CF/ E and (b) C-IEPM.....	52

VISCOELASTICITY OF CHEMICALLY BONDED INTERFACIAL EPOXY- POLYUREA MATRIX PER MIGRATION OF EPOXY SPECIES VIA CURING TIME PARAMETER

Figure 1. Generalized Maxwell Model.....	67
Figure 2. The calibration of the fitting results.....	70
Figure 3. Epoxy/polyurea Generalized Maxwell Model Components.....	71
Figure 4. DMA results of (a) polyurea and (b) epoxy at 20°C.....	72
Figure 5. Loss modulus $E''(\omega)$: (a) $E''(\omega)_{x-DC_{EPI}}$ via DMA tests; and (b) $E''(\omega)_{DCI}$ via DMA tests and assuming Fig. 3 model.....	73
Figure 6. Tan (δ) results for: (a) $x-DC_{EPI}$ (via DMA); and (b) Epoxy + DCI system.....	74
Figure 7. FE Model of a cantilever beam in single-mode bending, (b) Difference between the response of displacement and force.....	75
Figure 8. Harmonic Response of the specimen.....	76

LINKING NANOSCALE CHEMICAL CHANGES TO BULK MATERIAL PROPERTIES IN IEPM POLYMER COMPOSITES SUBJECT TO IMPACT DYNAMICS

Figure 1. (a) Optical microscopy image of sample 0- <i>IEPM</i> -0; (b)-(c) AFM image of <i>IEPM</i> -0 topography, spanning a region from pure epoxy (I_{EX}) to pure polyurea (I_{PU}). (d)-(e): IR spectra of 100 points (12 are shown in red), revealing chemical bond characteristics as a function of t_c	91
---	----

Figure 2. Optical images, AFM topography, and <i>nano-IR</i> spectra (corresponding to the red points shown in each interfacial region) of: (a) – (j) : 0- <i>IEPM</i> - t_c for $t_c = 0.5, 1, 2.5$, and 24; and (k) - (m): <i>C-IEPM-0.5 v</i>	94
Figure 3. Magnified AFM images and chemical images of various types of <i>IEPM</i> : (a) – (i) : <i>IEPM-0.5, 1.0</i> , and 2.5; and (j) - (p): <i>IEPM-0</i>	98
Figure 4. NMF vectors and corresponding intensity loading maps for: (a) 0- <i>IEPM-0.5</i> ; (b) 0- <i>IEPM-2.5</i> ; (c) 0- <i>IEPM-0.5 v</i>	100
Figure 5. DMA results of six 0- <i>IEPM</i> - t_c test samples (with adjoined epoxy), measuring (a) loss modulus; and (b) storage modulus.....	103
Figure 6. Scanning electron microscope (SEM) images of: (a) - (c) <i>C-IEPM</i> - t_c for $t_c = 0; t_c = 2.5$, and $t_c = 24$; (d) - (e) fractographs of <i>CF/E</i> and <i>C-IEPM-4</i> ; and (f) - (g) comparison of uniformity and transitionality of <i>IEPM</i> - t_c for $t_c = 3$ and $t_c = 4$	104
Figure 7. TMA results for three <i>C-IEPM</i> - t_c test samples, where we observe T_g for epoxy and polyurea in each sample, but T_g for the interface (chemical bonding) only in <i>C-IEPM-2.5</i> and <i>C-IEPM-3.5</i> , not in the case when polyurea is applied to fully cured epoxy.....	111
Figure S1. Schematic of suggested reaction, where formation of chemical bonding within the <i>IEPM</i> (interface) consists of the three-part reaction: (epoxide) + (amine epoxy hardener) + (isocyanate).....	122
Figure S2. Manufactured 0- <i>IEPM</i> - t_c sample and SEM image of 0- <i>IEPM</i> - t_c	123
Figure S3. DMA results of pure polyurea and pure epoxy, Set-up of Test Program B, including wood-constructed support structure, chronograph, and <i>C-IEPM-b-t_c</i> test panel.....	125
Figure S4. Set-up of Test Program B, including wood-constructed support structure, chronograph, and <i>C-IEPM-b-t_c</i> test panel.....	128

LIST OF ABBREVIATIONS

AFM	Atomic Force Microscopy;
AL PU	aliphatic polyurea;
AR PU	aromatic polyurea
CF/E	Carbon Fiber-Reinforced Epoxy (for a carbon reinforced polymer, CFRP);
CT	Compact Tensile test;
DCI	Dynamic Covalent epoxy/polyurea Interface (indicate the same as IEPM);
DGEBA	Bisphenol A diglycidyl ether;
DMA	Dynamic Mechanical Analysis
IPDI	isophorone diisocyanate;
IEPM	Interfacial Epoxy-Polyurea hybridized-Matrix;
IR	Infrared;
MDI	methylene diisocyanate;
ME.T	Mechanical Energy Transfer;
NMF	Non-negative matrix factorization;
SEM	Scanning Electron Microscopy;
SV	Surface-to-volume ratio;
TG	Test Girder;
x-DC _{EPI}	Fiber (<u>x</u>) reinforced <u>D</u> ynamic <u>C</u> ovalent epoxy-polyurea <u>I</u> nterface;
x-IEPM- t_c	x-Hybrid-polymeric Matrix Composite (t_c indicates the epoxy cure time); x indicates the fiber-type, where x = 0 means ‘no fiber’)

INTRODUCTION

Background and Existing Problems

Hurricanes are one of the most terrible weather phenomena and have posed a serious threat to infrastructure security in coastal areas in recent years, which is also closely related to the national and individual economic benefits. Hurricane Katrina in 2005 remains the single costliest hurricane in U.S. history – \$161 billion [1]. In 2017, Hurricanes Maria, Irma, and Harvey comprised three of the top five costliest hurricanes in U.S. history, resulting in \$265 billion in total economic losses and culminating in the costliest year on record (\$306.2 billion) [2]. Facing the threat of these highly destructive hurricanes, increasing the hurricane resistance of infrastructure in coastal areas has become a significant safety and economic concern. The *Natural Hazard Mitigation Saves: 2018 Interim Report* found a public benefit of \$11 for every \$1 invested in the disaster mitigation on utilities and transportation infrastructure,[3] which highlighted the importance or the potential value of investing in disaster mitigation.

Highway bridges, as one kind of essential infrastructure related to people's daily life are threatened by hurricane-induced surge and waves in coastal areas. Because of the impact of Katrina in 2005, at least \$1 billion was allocated to the repair or replacement of the damaged bridges. [4] Primary damage of the US-90 bay St. Louis Bridge was the loss of the cap-to-girder connection resulting in the unseating of the girders. This damage resulted in a cost of \$267 million for the replacement of this bridge. Another bridge on US-90, the Biloxi-Ocean Springs Bridge, also suffered the same damage; that is the loss of cap-

to-girder connection with the bridge spans unseating from bent cap during Hurricane Katrina. In addition to the direct damage to the bridge, it took significant effort and expense to salvage and dispose of these damaged bridge spans.

The same situation also occurred to the I-10 bay way twin bridge in Mobile, Alabama both in 2004 and 2005. Hurricane Ivan destroyed the Mobile bay way bridge in 2004, and Hurricane Katrina devastated the same bridge again in 2005. Some of the bridge spans were wiped out by the surge and waves caused by Hurricane Ivan in 2004. Also, many of the spans were laterally dislocated by the hydrodynamic force of the surge and waves. Moreover, in 2005, some on-ramp spans of I-10 bay way bridge in Mobile were laterally dislocated due to the impact load created by Hurricane Katrina. [5]

There are 140,000 miles of coastline in the US, and many highway bridges along the coastline are comprised of simply supported spans. [6] The existing bearing connections of these bridges between superstructure and substructure are fragile with respect to the hurricane-induced surge and surface wave forces. Once the cap-to-girder connection is lost, the deck can be easily raised and pushed forward by the strong waves, leading to dislocation, flipping, and dropping the spans into the water, which are catastrophic damage to this type of bridge structures. It is generally believed that coastal highway bridges collapse in a hurricane because of the designs that did not take into account the hurricane-induced surge and wave loads: first, the clearance of the bridge was too small; second, the connections between the upper and lower structures of the bridge were too weak to against the loads.[7]

Alleviating the disaster caused by the hurricane to coastal highway bridges can be accomplished in two ways: (1) increasing the clearance of the bridge, which makes the

waves unable to impact the bridge span; and (2) strengthening connections between bridge superstructure and substructure, which allows the bridge spans to resist the forces due to surge and waves.

Technically, the first option to increase the elevation of the bridge is better as the elevation of the bridges contributes the most to the hurricane-induced wave loads. [8] But in reality, more factors need to be considered, for example, the budget. In July 2019, the Alabama Department of Transportation (ALDOT) planned to take the first solution and presented a project that estimated to spend \$2.1 billion to replace the old bridge and rebuild a new toll bridge in Mobile Bay which could withstand a 100-year hurricane[9]. However, a toll bridge means that the government does not have enough budget for the bridge, and many people will pay more for everyday transportation, which has caused a big argument in Alabama.

It does take much money to replace old bridges and construct new bridges. Moreover, it is a considerable waste to remove an old bridge if it is still within its service life. So, sometimes, it may be better to select the more economical option to strengthen the connections of these highway bridges in coastal areas, which makes the research on connections strengthening for coastal bridges to against hurricane-induced surge and wave loads vital and necessary.

Hurricane induced surge and wave loads on bridges

Due to the significant damage of coastal bridge caused by the Hurricane Karina in 2005, many researchers began to pay attention to the impact of waves on the coastal highway bridges. The Auburn report in 2008 [10], compared four different methods, which

included the AASHTO method, to calculate the maximum hurricane wave induce load on the bridge deck and recommended the modified Douglass function (attached in the appendix A) for the calculation of the maximum hurricane wave-induced load on coastal bridges. The Auburn report concludes that a Mock-C simulation would generate the following maximum surge/surface wave forces on the bay-way spans: F_v (vertical force) = 539 kips (2398 kN); F_h (lateral force) = 169 kips (752 kN); and M (moment) = 5,769 kip • ft (7822 kN • m). The calculation of load is based on the theoretical mechanics assumption in-plane, where a bridge cross section is taken for analysis and the main parameters are maximum wave elevation and bridge elevation (See Appendix). However, it does not take into account the dynamic characteristics and the three-dimensional distribution characteristics of the wave load.

Recent studies have focused on the forces acting on the bridge deck and the motion response of the deck under the impact of waves. For example, Bradner [11] et al. did an experimental model of a 1/5 scaled bridge span to study the reaction response at each connection of the deck under wave forces. Do [12] et al. built a large-scale 3D model using Abaqus to simulate the impact of waves on the coastal bridge model, and the reliability of the finite element simulation is verified by comparison experiments. Yalong Cai [13] build a 2D FSI model using Adina to investigate the bridge decks under a simulated wave impact, which indicates that the lack of capacity of the bridge connections.

Based on current research, the researchers are keener to observe the real-time response of the bridge under hurricane loads. They like to use the CFD simulation to perform their study. However, because of the limitation of the computing capacity, many of these researches use a small model instead of actual size, and the CFD simulation always

considers the bridge deck is a rigid body and assumes the connections of the bridge deck to the cap as either tied or free, which is not accurate. While computing capacity becomes greater and greater, future studies on this problem should consider the fluid-solid coupling effects. This research helps to understand the factors (for example, the wave's period and height) that influences the loads on the bridge deck. And the accurate simulation results can be used to direct the experiments on this particular topic.

Existing connections and its failure modes

Connections between the superstructure and the substructure of coastal highway bridges are liable to damage under the impact of hurricane-induced surge and wave action. It is crucial to determine how the connections are damaged as a result of the surge and wave loads, which would help to find the right solution to strengthening the connections. There were a few research works focused on these bridge connections, most of which involved on-site investigations.

Figure 1 shows the site investigation photos of the connections between the substructure and the superstructure of the I-10 bay way bridge. The bridge superstructure is connected to the bent cap using “L” clip angles with one side bolted to the girder, and another side bolted to the cap beam. Moreover, some of the girders were not bolted to the cap beam, see Figure 1(b), due to construction errors or difficult access. In some area, where the steel connection is exposed to the air and seawater without enough protection, the steel is easily corroded, which may allow the connections to fail when loaded with the hydraulic impact force. These weak connections make the bridges susceptible to catastrophic damage in the event of large hydrodynamic forces and hydrostatic forces,

where the latter may be caused by slamming forces from breaking waves which would subsequently entrap air and create large upward force on the superstructure. The resulting buoyant forces, effectively reducing the weight of the spans, may facilitate lift-up of the spans from their supports and sub-structures.



Figure 1. Typical ‘anchored’ spans: The underside of the I-10 East bay- way.

For the bolted girders, the most common failure mode is failure of the inserts embedded in girder failure. [14] Figure 2 depicts this type of failure mode, where the threaded inserts are pulled out by lateral dislocation, while the concrete on the bottom bulb of the girder is broken.

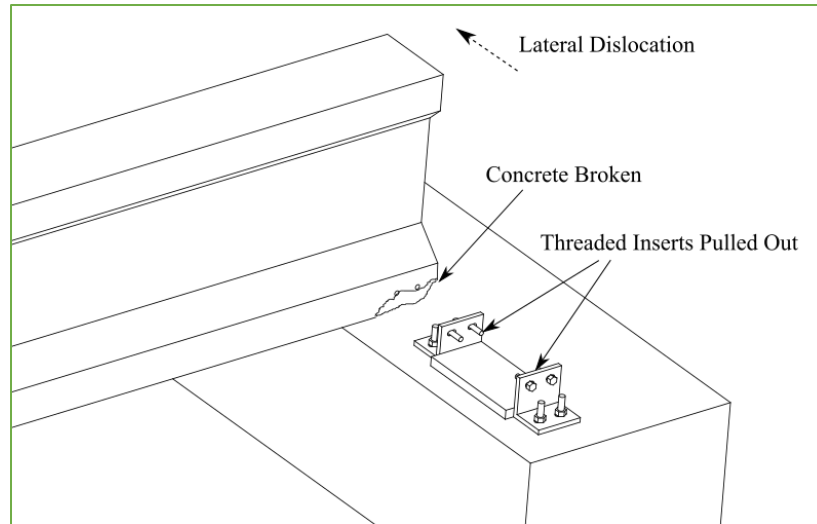


Figure 2. Threaded inserts pulled out of girder bottom bulb

Another failure mode is concrete spalling and subsequent failure of the embedded anchor bolts (in the cap) as shown in Figure 3. The cap beam concrete has spalled in these cases because of the tremendous stresses in the bent and its anchor bolts.

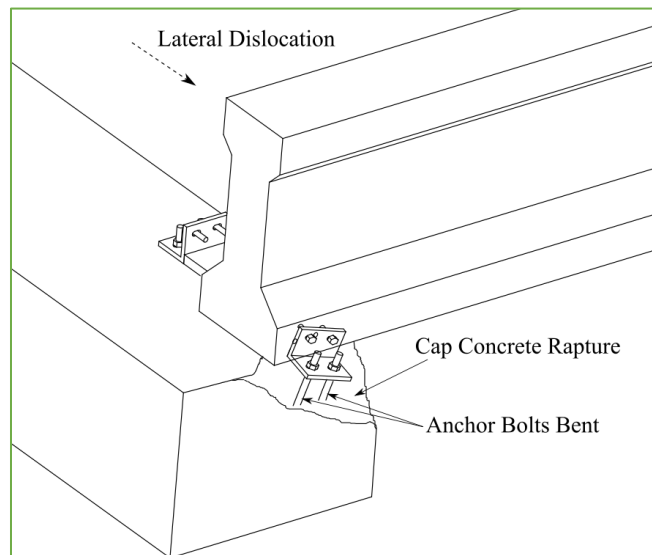


Figure 3. Spall and bent anchor bolts and concrete rupture at the end of bent cap

The last case of failure mode is the clip angle failure [14], which is shown in

Figure 4, indicating that angle failure may be induced by lateral forces, without weakening of the angle due to corrosion from seawater.

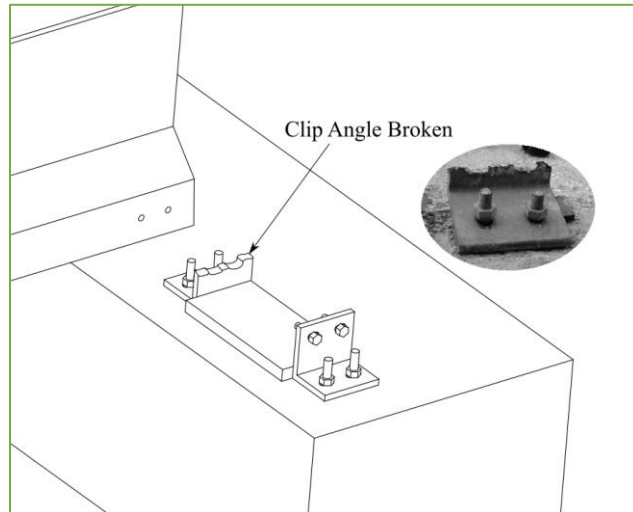


Figure 4. Damaged clip angles remaining after girders moved laterally

Current solutions to the connection problems for coastal bridges

Because the connections between the upper structure and the substructure of the I-10 Bayway Bridge are not reliable under the condition of Hurricane load, the bay bridge is likely to repeat the tragedy of 2005, causing billions of dollars in losses. Many researchers have proposed some new strengthening methods for the bay bridge structure to deal with this catastrophic damage. However, many of the proposed methods may lead to higher stress concentrations in the concrete of the connecting part, leading to the spalling of the concrete.

In 2008, ALDOT had a new plan for increasing the connection capacity, which utilizes through-bolts instead of the threaded inserts, see Figure 5. And in 2011, at the conference “*Solutions to Coastal Disasters 2011*” held by ASCE, Ian N. Robertson et al.

[14] recommended the same connection method for the solution. However, this type of connection may not be the ideal solution to the coastal bridges' problems caused by a hurricane.

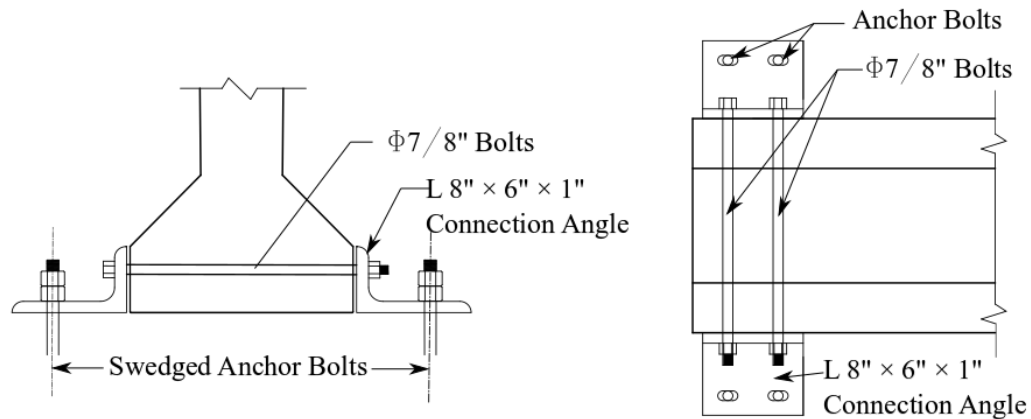


Figure 5. Post Katrina connection design

In 2011, Jora B. Lehrman et al. [15] did a study on the performance of highway bridge girder anchorages under an actuator-simulated hurricane wave induce load, where three typical anchorages (See Figure 6) for AASHTO Type III girders were investigated, and the ultimate capacity of these three types of anchorages with vertical loading were: 102.1 kN for Clip Bolt (Figure 6a), 417.4 kN for Headed Stud (Figure 6b), and 151.1kN for Through Bolt, all of which were far less than 566.2 kN induced by Hurricane Katrina, Mock C. The results show that the post-Katrina connection only increases the capacity of the pre-Katrina connection by about 50 percent, which is insufficient to provide the resistance required to survive a 100-year hurricane similar Katrina.

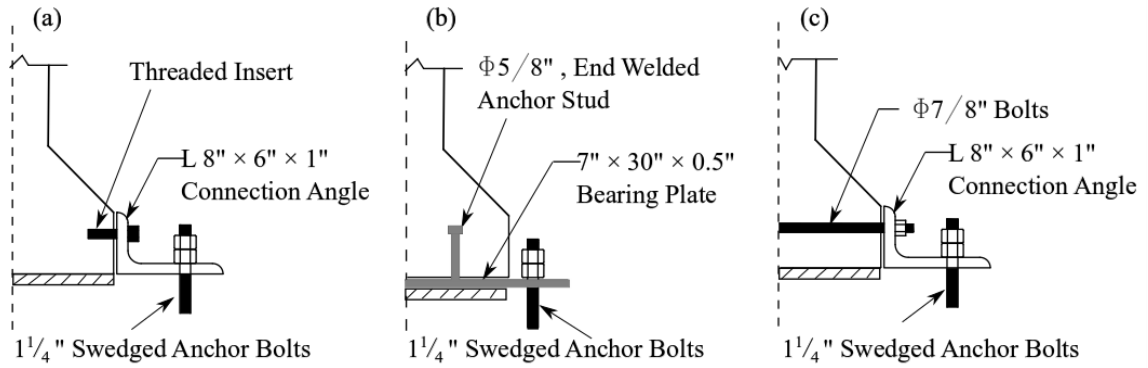


Figure 6. AASHTO Type III girder connections

There were also some other proposed strengthening methods to increase the hurricane resistance of coastal bridges presented by US Federal Highway Administration in 2016. [16] Figure 7 also shows potential retrofit methods to the existing I-10 Bridge, which would increase continuity. The first option is to increase the connections' capacity, where Figure 7a depicts the connection that makes a "Z" shape clip angle that can cover the girder bulb and uses two steel braces to increase the clip angle's stiffness. The second option is adding shear bocks on the cap to prevent the girder from moving laterally. The third option is drilling holes in the end diaphragm of bridges and using stiff rods to increase the connectivity of each bridge deck, which may increase the effective weight of a single span and allow adjacent spans to resist the impact load together.

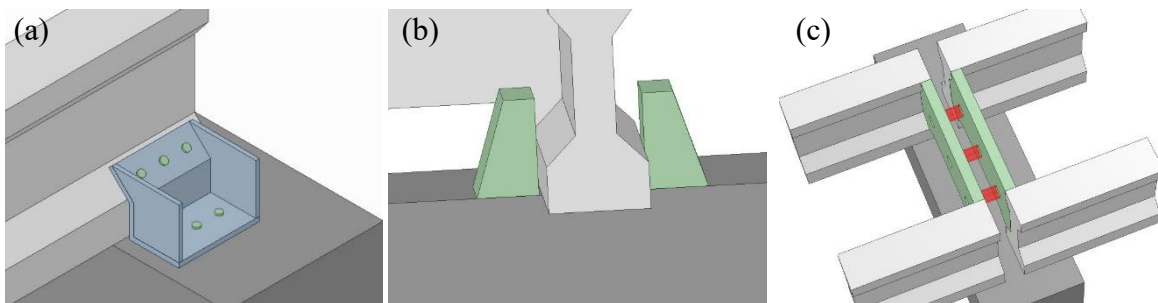


Figure 7. (a) Connection that increases the lateral and uplift capacity; (b) shear block type connection; (c) connection to increase span continuity

These are possible options to improve the capacity of the bridges' hurricane resistance. However, an ideally rigid anchor connection, like Figure 7a, is not a viable solution, providing minimal energy dissipation to attenuate potentially large accelerations and resulting in sudden concrete fracture and superstructure uplift or lateral dislocation. Also, the negative moment may cause some problems to the connection such as cracking at the girder ends. The shear blocks in Figure 7b only increase the lateral capacity, but not do provide any vertical resistance. The third option in Figure 7c needs more research validation as the diaphragm is very thin.

Other concepts considered for increasing the capacity of the cap-to-girder connection include using FRP to wrap the end of the girder end and the bent cap, drilling holes in the deck to allow air to pass through the deck to reduce the buoyancy of the entrapped air, and providing external connections to the superstructure and substructures.

Carbon fiber reinforce Interfacial Epoxy / Polyurea Matrix (C-IEPM)

In this presented the research, Carbon-fiber reinforced Interfacial Epoxy-Polyurea Matrix (C-IEPM) is used for external connections for the bridge in the coastal area. C-IEPM is an innovative composite developed to dissipate more energy when it was used for structural retrofitting. The C-IEPM is manufactured using a dual-hybrid matrix system involving amino-based polymeric compounds to provide necessary viscous-type damping and high strength sustainability. Tekalur [18] et al. conducted a blast experiment to test a polyurea coated composite's blast resistance and found that the additional layer of polyurea on the impact face considerably increases the blast resistance. Zhou[19], et al. indicated that energy absorption tends to increase with more exceptional polyurea thickness and

lower elapsed curing time(t_c) of the epoxy in both quasi-static and impact crash tests.

The objective of the research

The goal of the proposed research is to optimally mitigate highly probable catastrophic surge and wave force damage to coastal bridges at an affordable cost.

The objectives of the proposed study are:

Provide a cost-effective connection detail that will reduce damage by hydrodynamic forces from wave and surge loading using C-IEPM

Enhance ductility and damping, fracture toughness, and impact-resistance properties through the use of C-IEPM

Increase the vertical force and lateral force capacities of the bridge cap-to-girder connection

Ensure adequate joint expansion via elastomeric C-IEPM

Develop a ‘processing window,’ i.e., a timeframe to manufacture C-IEPM on-site to achieve desirable properties of C-IEPM.

In the proposed study, the analysis that stems from the 930-687 Auburn Report [10] for Category 3 - 5 hurricanes will be used to develop a cost-effective C-IEPM connection detail to accommodate hydrostatic and hydrodynamic forces to protect against surges over 17ft and large wave forces, i.e., Mock C hurricanes. The C-IEPM will be specifically designed for critical connections in order to maximize energy dissipation in each bridge, i.e., the ‘total-bridge.’ The analysis, treated as a significant optimization problem, will yield the best combination of C-IEPM connections (i.e., comprised of the same system of polymers but processed differently) at various locations in the bridge.

While enhancing ductility is a critical facet of this research, the dissipation of kinetic energy maximizes damage mitigation upon surge and wave impact, where damage to the connection detail is ‘localized’ via ‘damage barriers’ built within the C-IEPM. This provides tremendous resiliency to the connection and also helps sustain the strength of the C-IEPM. To accomplish this, C-IEPM dissipates energy through an internal damping phenomenon that is located at the interface of its unique epoxy - polymer (which is a pre-stabilized polymer) reaction, thus allowing substantial energy to be dissipated via molecular interfacial redundancy. The dissipation of energy through the C-IEPM joints also reduces the amount of force that is ultimately transmitted to the piers.

Organization of Content

This research aims to develop an effective connection method for coastal bridge against hurricane-induced surge and wave using an innovative fiber-reinforced composite. This research compares different connections that may be used on existing coastal bridges, which proves that the proposed material (C-IEPM) has an excellent potential to be the candidate for application on coastal bridges. Moreover, this research encompasses a more in-depth investigation of the proposed C-IEPM so that the properties of this strengthening material (C-IEPM) can be improved.

Paper 1 presents the experimental results of the six scaled concrete girders tested using a modified, simulated storm surge and slamming wave force function, derived using regional maps for a 100-year return-period Hurricane Katrina type storm. Responses of the different connection details include pre-Katrina, post-Katrina and strengthened connections using CF/E (Carbon Fiber reinforced Epoxy) and C-IEPM are compared,

showing that the C-IEPM strengthened connections are the best performing, dissipating more energy and offering better resistance to hurricane induced forces than CF/E.

Paper 2 focuses on the effect of the bonding property that affects the damping of the proposed material C-IEPM (called C-DCI in Paper 2). Different pre-cured times, t_c , are investigated using Dynamic Mechanical Analysis (DMA), and a viscoelastic model is developed using the General Maxwell Model, whose parameters are used in an Abaqus finite element model. Finally, the FE analysis proves that a better adhesive between epoxy and polyurea results in a higher $\tan\delta$ or damping.

Paper 3 discusses in more detail the investigation of the interfacial area of C-IEPM, using Nano-IR and SEM, investigating the chemical reactions of the interfacial areas so a new polyurea can be produced. The results show that the lower t_c leads to a wider interfacial area, allowing a better transition from epoxy to polyurea. This new polyurea toughens the epoxy surface, giving the CF/E better fracture toughness and energy dissipation. This accounts for why the C-IEPM has a much better performance than CF/E and why the control of curing time (t_c) is important for the application of this new material.

INTEGRATING ENERGY TRANSFERABILITY INTO THE CONNECTION-DETAIL
OF COASTAL BRIDGES USING REINFORCED INTERFACIAL EPOXY-
POLYUREA REACTION MATRIX COMPOSITE

By

LI HE, THOMAS L. ATTARD, HONGYU ZHOU, AND ADAM BROOKS

Composite Structures, Volume 216, 15 May 2019, Pages 89-103

Copyright
2019
by
ELSEVIER

Used by permission
Format adapted and errata corrected for dissertation

Abstract

A new Carbon-fiber Interfacial Epoxy-Polyurea Matrix (C-IEPM) composite is investigated as a potential retrofit option for vulnerable girder-to-cap connection-details in coastal highway bridges. IEPM is a reaction of crosslinking epoxy with functional groups of pre-polymerized polyurea, producing an energy-transfer mechanism inherently absent in conventional carbon-fiber reinforced epoxy (CF/E) that drastically reduces the serviceability limit state during extreme hurricane events. IEPM is a covalently bonded interface, produced as a reaction of migrating epoxy species (epoxide and amine-based hardener), controlled as a function of their curing time (t_c), with highly reactive isocyanate and amine polyurea moieties. To demonstrate IEPM effectiveness, six scaled concrete girders were tested using a modified simulated storm surge and slamming wave force function, derived using regional maps for a 100-year return-period Hurricane Katrina. Two girders, designed using current AASHTO field connection-details, failed catastrophically (concrete shear failure) in less than one-half load cycle. The CF/E-strengthened girder, failing in less than one load cycle, experienced severe damage to its girder-to-cap connection, including fiber and epoxy matrix breakage, delamination, unsustainable girder-end rotations, and transient force-displacement hystereses loops. However, after 12 load cycles, the C-IEPM-strengthened girder, providing substantial energy transferability (material damping) through its connection-details, experienced only local cracking.

Keywords: AASHTO connection-details; FRP; Energy transferability; Polyurea; IEPM

Introduction

In 2017, Hurricanes Maria, Irma, and Harvey comprised three of the top five costliest hurricanes in U.S. history, resulting in \$265 billion in total economic losses and culminating in the costliest year (\$306.2 billion) on record [1]. However, Hurricane Katrina in 2005 remains as the single costliest hurricane in U.S. history - \$161 billion, including over \$1 billion in repair or replacement cost of damaged bridges [2]. Hurricane Katrina also revealed a direct relationship between elevated storm surge and structural damage (although debris impact was also a prominent factor), highlighting deficiencies in girder-to-cap connections (“connection-details”) in highway bridges along the U.S. Gulf Coast. Currently, there are over 70,000 bridges crossing coastal tidally-influenced waters in the U.S. Many of these bridges were designed similar to the I-10 bay-way twin bridges in Mobile, Alabama [3], which experienced unseating and significant drifting of bridge decks, namely six on-ramp spans, from storm-induced wave forces during Hurricane Katrina, exemplifying the potential devastation that large storm disasters can levy on coastal bridge infrastructure.

Current strength design and retrofit solutions for coastal bridges may not sufficiently mitigate substantial damage, let alone minimize limit states [4], during large hurricane events. Post-disaster surveys reveal that elevated storm surge and waves are directly responsible for bridge structural damage, mainly due to weak girder-to-cap connections. Douglass (2006) [5] and Chen (2009) [6] determined that culpable storm surges conduce strong lateral strikes (slamming wave forces) on the superstructure, exceeding the design capacity of cap-beam anchors. Ramey et al. (2008) [7] found that superstructures are pushed-off of their cap-beams decks, as decks become dislocated,

because of insufficient connection-details. In this light, remediation of the connection-detail has been examined using various laboratory experimental and computational simulation tests to analyze the effects of wave forces. Douglass [5] developed a method to calculate the horizontal and vertical wave loads on bridge decks. Using the I-10 bay-way bridges in Mobile, Ramey et al. [7] compared AASHTO design specifications to Douglass and modified Douglass methods, finding that the latter more consistently modeled field data because it accounted for the trapped air under the bridge deck cell, perpetrated by the rising surge and leading to hydrostatic forces. Schumacher et al. [8] and Bradner et al. [9,10] simulated dynamic deck responses of the I-10 bridge across Escambia Bay using a 1:5 scale model and over 400 wave conditions to capture actual wave effects. Xiao and Huang et al. [11] used the Biloxi Bay Bridge in Mississippi to develop a volume of fluid (VOF) model to investigate the effects of submersion depth of the bridge deck on wave uplift force during Hurricane Katrina. Bozorgnia et al. [12] and Seiffert et al. [13] examined the influence of trapped air on bridge decks. In 2017 and 2018, Tang et al. [14, 15] used a numerical model to confirm that the response of bridge-decks to wave forces is mostly influenced by the behavior of the connection-details.

Lehrman et al. [16] tested threaded insert/clip bolt anchorage (CB) of Pre-Katrina (as-is) and through-bolt anchorage (TB) Post-Katrina (retrofit) connection-details in coastal highway bridges subjected to simulated Katrina wave forces, revealing the connection region's vulnerability to sudden catastrophic failure. While various retrofit and strengthening techniques have been explored to enhance the capacity of the connection-details and remediate their failure mechanisms [17], many of these methods ostensibly lack sufficient material damping to transfer the high dynamic energy from imposing hurricanes.

For example, the “post-Katrina” retrofit, implemented in the I-10 bay-way across Mobile Bay, increased embedment length of the anchors (into the cap-beam) and extended threaded inserts through-the-width of the flange. Other alternative retrofit measures included: (1) steel strips to strengthen connection-details; (2) shear blocks to alleviate lateral dislocation of girders; and (3) Fiber-Reinforced Polymer (FRP) to increase shear strength of the concrete (see Ramey et al. [7]), albeit FRP has a propensity to experience brittle and sudden shear failure [18]. Because these solutions underperformed [7], another suggestion centered on increasing the superstructure elevation to reduce uplift and lateral forces at the girder-to-cap region [17]. However, demolition and reconstruction of coastal bridges, including many older low-lying bridges, can be cost-prohibitive [19], consuming more material and time while disrupting a municipality’s functionality, and may ultimately induce larger stresses.

In the absence of significant material damping at the connection-details in current strengthening and retrofit schemes, a new materials-interface solution is proposed for coastal bridges under extreme wave forces. C-IEPM utilizes the time of epoxy curing, t_c , to dial-in chemistries that, at the macro-scale, are shown to enhance safer energy transferability through the connection-details. Six, 25% scaled spans, including 4.57 m long reinforced concrete girders supported on rigid end-cap-beams, were dynamically tested by applying a scaled function that mimicked simultaneous surge and slamming wave forces (Hurricane Katrina). Connection-details of the test girders included: (1) mechanical threaded inserts and bolts plus cap-beam anchors, (2) CF/E, and (3) C-IEPM. Analysis of the failure modes in the six spans revealed that insufficient material damping in the connection-details would render current field-designed girders as susceptible to rapid

destruction due to potential shear failure of the concrete that surrounds the ‘threaded inserts and bolts’ connection. Test results of a “Post-Katrina” retrofit, which uses threaded inserts with through-bolts (through the width of the flange) and an increase in anchor development length into the cap-beam, reveal only a marginal reduction to the serviceability limit state in coastal bridges. The results highlight that an increase in ductility without bona fide means to enhance material damping leaves coastal bridges vulnerable and likely to experience quick catastrophically failure during large hurricane events. To address this issue, a C-IEPM-retrofit of the connection-details, relative to a conventional CF/E retrofit, shows that C-IEPM substantially increases material damping, thus relegating girder damage locally and drastically enhancing bridge serviceability.

Description of Interfacial Epoxy-Polyurea Matrix (IEPM)

Conventional Carbon Fiber Reinforced Epoxy (CF/E), or generally referred to as CFRP (P = polymer), is a high-strength brittle material commonly used to strengthen or retrofit various civil/ structures [20-22]. Inception of an Interfacial Epoxy-Polyurea Matrix (IEPM) and its integration to CF/E – by annexing IEPM to CF/E to produce a new Carbon-fiber Interfacial Epoxy-Polyurea Matrix (C-IEPM) – is conceptualized on the notion of a highly damped transitional material, specifically a chemically bonded interface characterized by designable molecular vibrational properties, that lies between brittle epoxy matrix and (elastomeric) polyurea matrix. The purpose of IEPM is to enhance energy transferability (e.g., dissipation) of imparted wave-induced energy, diverting crack formations away from stiff and brittle fiber and epoxy networks, thus allowing the high-strength of carbon-fiber to be sustainable while incorporating greater structural resiliency

[23]. Aliphatic polyurea is a two-part elastomer consisting of Part A, i.e., an (-NCO)-based quasi-prepolymer comprised of isophorone diisocyanate (IPDI) and polyoxypropylene diamine (in lieu of the polyol used in aromatic polyurea), and Part B. Part B is a resin-blend composed of a high-molecular weight resin, e.g., polyoxypropylene amines, that develop polyurea flexibility, and a chain extender. The chain extender is a low-molecular weight cycloaliphatic diamine, that helps to complete the polymer chain and controls overall polyurea dry-time, moisture diffusivity and moisture absorption. The lack of moisture-inducing polyol and addition of a co-chain extender (or a hindered amine) further helps promote chemical reactivity between (-NCO) moieties and curing epoxy (and small t_c), resulting in high-quality IEPM that drastically enhances material damping in conventional CF/E.

Paucity of essential material damping in CF/E structures is often over-compensated by aggrandizing carbon fiber quantity, thus amplifying cost and pre-disposing the structure to unexpected failure. Similarly, while a polyurea top-coat applied to cured CF/E can provide additional elasticity, polyurea cannot sufficiently supplement fracture energy absorption in CF/E to stabilize crack growth and crazing [24]. However, a well-designed IEPM, located between epoxy and polyurea components and comprised of aliphatic “pre-polymerized” polyurea moieties and curing epoxy (at small t_c and low epoxy-resin viscosity), is a viable candidate for injecting critical material damping and fracture toughness in CF/E-designed composite structures.

IEPM is a chemical mixture of topically mixed curing epoxy and reactive polyurea, whose moieties (functional groups) chemically react to produce a covalently bonded structure. Zhou and Attard [25 - 27] previously examined CF/E - IEPM (C-IEPM) as a

retrofit option in severely damaged reinforced concrete walls and beams, in new steel beams, and in the design of tornado storm rooms, demonstrating the ability of C-IEPM to sustain high-fiber-strength by enhancing material damping, and thus reducing the risk of catastrophic structural failure. **Fig. 1** illustrates the multi-layer composition of C-IEPM: Fiber, Epoxy, IEPM, Polyurea.

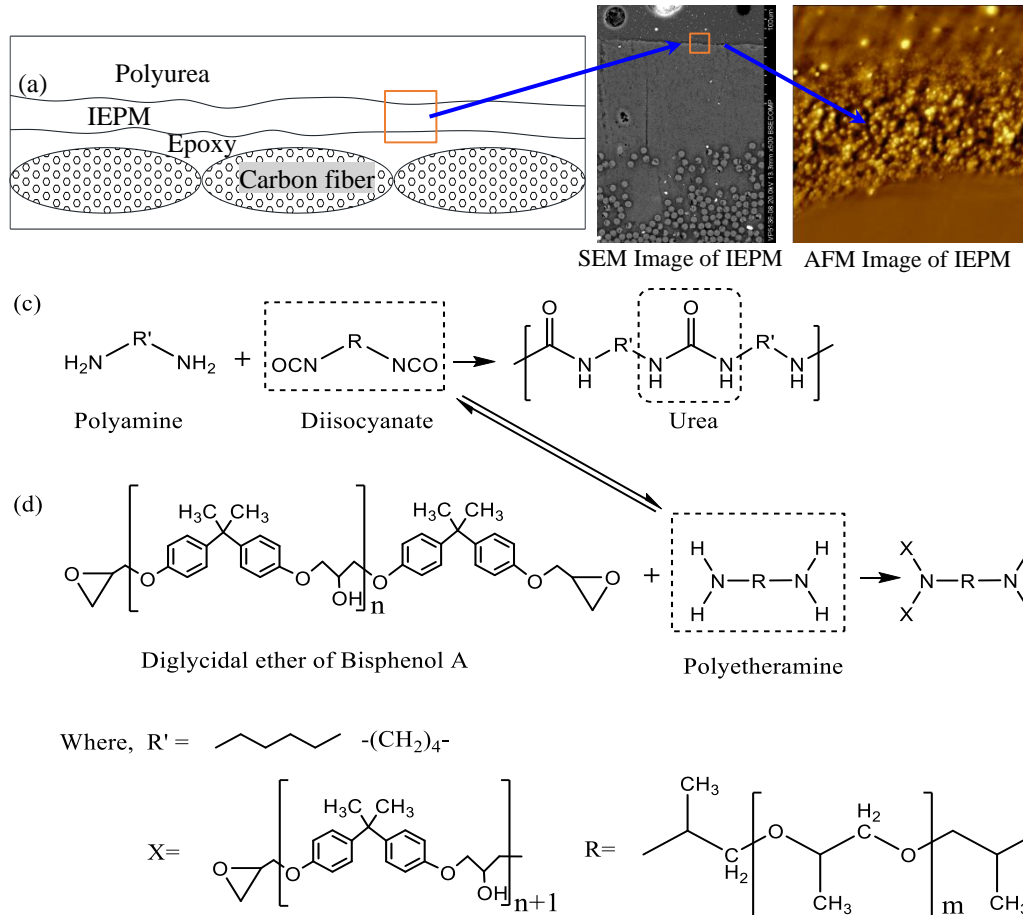


Fig. 1. (a) IEPM polymerization comprised of covalent bonds between polar $-(\text{NCO})$ and $-(\text{NH}_2)$ -epoxy moieties, and epoxide functional groups; and (b) curing reaction of epoxy

The reaction of ongoing cross-linking between $-(\text{NH}_2\text{-epoxy})$ and epoxide (as a function of t_c) leads to a likely reaction between epoxide, $-(\text{NH}_2\text{-epoxy})$, and $-(\text{NCO})$,

which comprises a covalently bonded IEPM structure, see **Fig. 1**. Depending on the curing time, t_c , of $-(\text{NH}_2\text{-epoxy})$ and epoxide before applying the “pre-polymerized” polyurea, designable material damping and fracture toughness may be incorporated into C-IEPM-retrofitted structures, verifying a link between IEPM (t_c) chemical bonding and bulk material properties.

Parts A and B of aliphatic polyurea are mixed in the impingement chamber of a spray gun (Fusion Air Purge[®] by Grayco[®]) at 73.9°C and pressure at 14.5 MPa. In “pre-polymerized” form, i.e., in its dynamic or still-curing form, the polyurea mix is sprayed to the desired epoxy surface. In accordance with fiber-epoxy manufacturer specifications (BASF[®]) [28], the epoxy-resin (DGEBA) and amine-based hardener were mixed at a ratio of 3 : 1.

IEPM provides supplementary material damping to CF/E depending on its “chemical bond richness,” i.e., distribution and density of the chemical bonds. IEPM, characterized by designable enthalpy and molecular vibrational properties, evinces energy transferability [29] via loss modulus and fracture toughness, providing added resistance to the girder/ cap-beam connection against large wave and surge impact forces. In the formulation of C-IEPM, t_c is a critical processing parameter, linking optimal moiety reactivity between $-(\text{NCO})$, $-(\text{NH}_2\text{-polyurea})$, $-(\text{NH}_2\text{-epoxy})$, and epoxide that maximizes energy transferability of surge and impact forces. He and Attard [30] showed that $t_c = 0$ (applying polyurea immediately after mixing epoxy-resin and amine-based hardener) maximizes loss modulus (\propto which is proportional to material damping) in C-IEPM, thus minimizing connection-detail damage. In the construction of CF/E and two out of the three C-IEPM test girders, the carbon fiber sheets (FIB 600/50 CFS, uni-directional

architecture, 600 g/m², 3800 MPa tensile strength, 0.33 mm/ply fiber thickness) were produced by BASF[®], USA. Although the strength of CF/E and C-IEPM is approximately the same (2,800 MPa) - i.e., the tensile strength of polyurea (100% solids pure aliphatic polyurea produced by VersaFlex[®], USA) is negligible (between 5 and 17 MPa), the IEPM chemistry in C-IEPM contributes critical molecular vibrational / damping properties [30] that conventional CF/E lacks.

Experimental Program

Preparation of scaled girders specimens and connection details

The AASHTO Type III girder used in the I-10 bay-way bridge across Mobile Bay is depicted in **Fig. 2a**. Lehrman et al. [16] used a modified AASHTO Type III prestressed girder in an anchorage study of highway bridges subjected to simulated wave-induced loads. In the current study, six AASHTO Type III test girders were designed according to plans provided by the Alabama Department of Transportation (ALDOT) using similar cross-sectional geometries, see **Fig 2**. The lab-designed (test) girders were constructed at ¼-scale of a typical field-designed girder in terms of span-length (4.57 m versus 18.29 m) and at approximately ⅓-scale in terms of cross-sectional area (0.123 m² versus 0.361 m²). Similarity principles were maintained between the lab and field designs, where corresponding stresses at the connection-details and near the concrete girder-ends remained consistent. **Fig. 2b** illustrates the cross-section of a typical lab-scale test girder, and **Table 1** compares design details of the prototype AASHTO III type girder and the test girder. As-is connection-details of the prototype field-girders are in accordance with existing “Pre-Katrina,” see **Fig. 3a**, and “Post-Katrina,” see **Fig. 3b**, designs [7,31]. Carbon- fiber (CF/E

and C-IEPM) was used to strengthen the connection-details, see **Fig. 3c**, by wrapping it around portions of girder cross-section and cap-beam; the strategy is akin to conventional CF/E-strengthening of marine-pile connection-details [32].

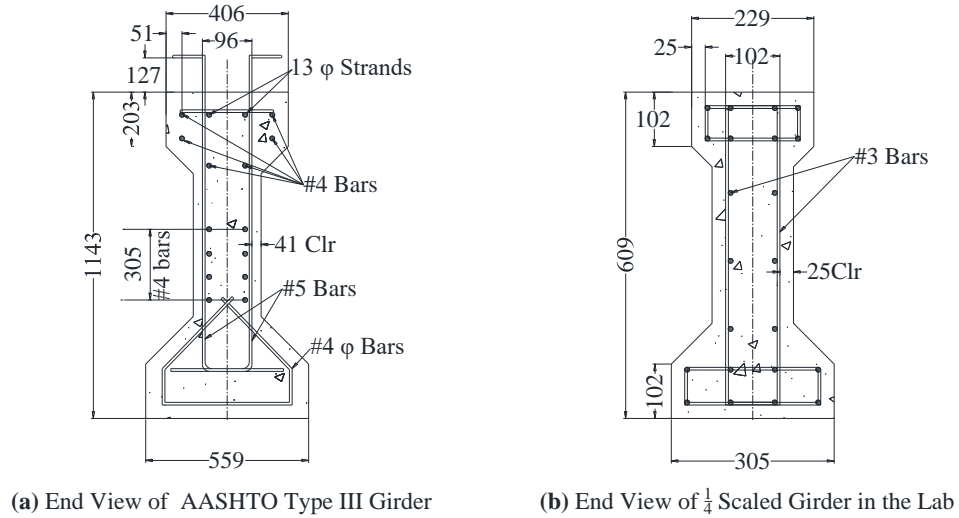


Fig. 2. End view of AASHTO girders: (a) in the field; and (b) in the lab (dimension in mm)

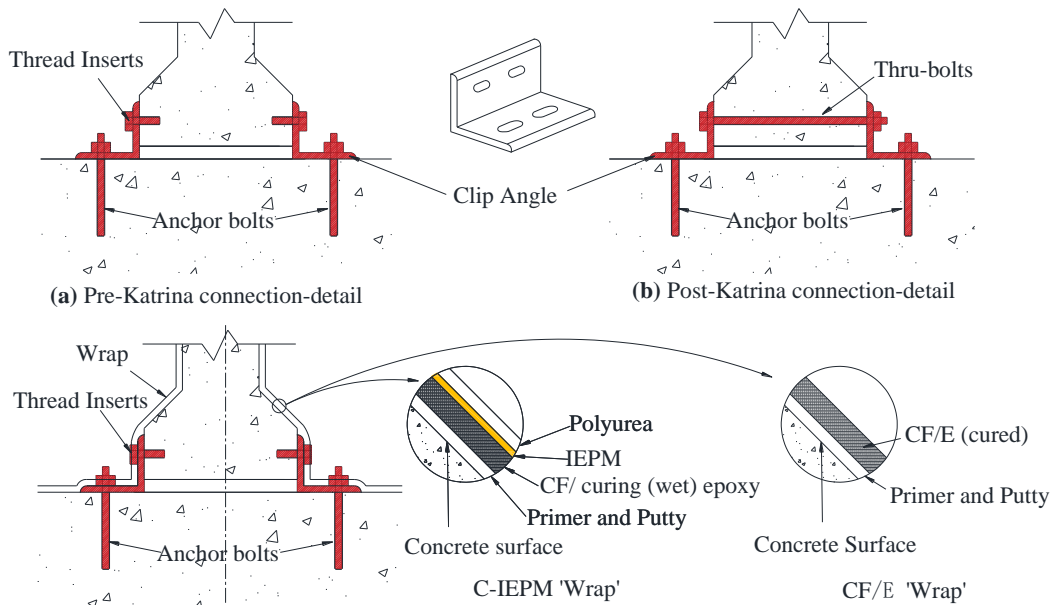


Fig. 3. (a) Pre-Katrina connection-details; (b) Post-Katrina connection-details; and (c) options for strengthening existing mechanical connection-details using C-IEPM and CF/E

In order to enhance ductility, stiffness, and strength in the substructure of the I-10 bridge (below the girder), one retrofit option [33, 34] involved wrapping CF/E around portions of the pier, connection-details, and girder. However, delamination and significant fiber damage made this option ineffective against large hurricane wave forces due to a lack of substantial damping which delimits structural resiliency and strength sustainability. Conversely, in order to ascertain a remedy to CF/E shortcomings, C-IEPM was used to reduce girder responses and alleviate failure of the connection-details through the IEPM interface via supplemental material damping.

Table 1

Comparison of AASHTO type III girder used in the field and $1/4$ - scale test-girder

Component	As-Is	Lab-Scale
Girder Type	Pre-stressed	Reinforced
Concrete Grade (U.S.)	4,000 psi	4000 psi
Span Length	18.28m	4.57m
Section Depth	1.14m	0.61m
Flange Width	0.559m	0.305m
Anchors bolts	$\phi = 31.75$ mm; L= 381 mm; 279.4 mm embedment	$\phi = 15.88$ mm; L=203 mm; 1524 mm embedment
Thread inserts (Pre-Katrina)	$\phi = 19.8$ mm; L=76.2 mm; 63.5 mm embedment	$\phi=12.7$ mm; L=50.8mm; 38.1 mm embedment
Thru-bolts (Post-Katrina)	$\phi = 22.2$ mm;	$\phi =12.7$ mm;
Length (L); Diameter (ϕ)	L = 508 mm	L = 330mm

The fiber lay-up design for CF/E and two of the three C-IEPM test girders are identical, see **Fig. 4a** inset. **Fig. 4a** illustrates the sequential (step-by-step) application of fiber to the connection-detail, providing a nominal strength of about 2.503 kN / mm (of

fiber width along the weak girder / cap-beam edge). **Fig. 4b** shows the application of anchor strips, and **Fig. 4c** shows the final fiber-epoxy lay-up at the girder cross-section. **Fig. 4d** shows a close-up view of the retrofitted mechanical connection-details. In **Figs. 4b - d**, CF/E is generated when the epoxy has fully cured while C-IEPM (total thickness of ~ 7 mm) is produced after spraying a thin layer (~ 3 mm) of polyurea to curing epoxy. The loss modulus (\propto material damping) provided by IEPM (physical width: $10\text{ }\mu\text{m}$ to $50\text{ }\mu\text{m}$), which is layered beneath the overlying polyurea, provides tremendous resilience to the girder and increases the likelihood of hurricane survival.

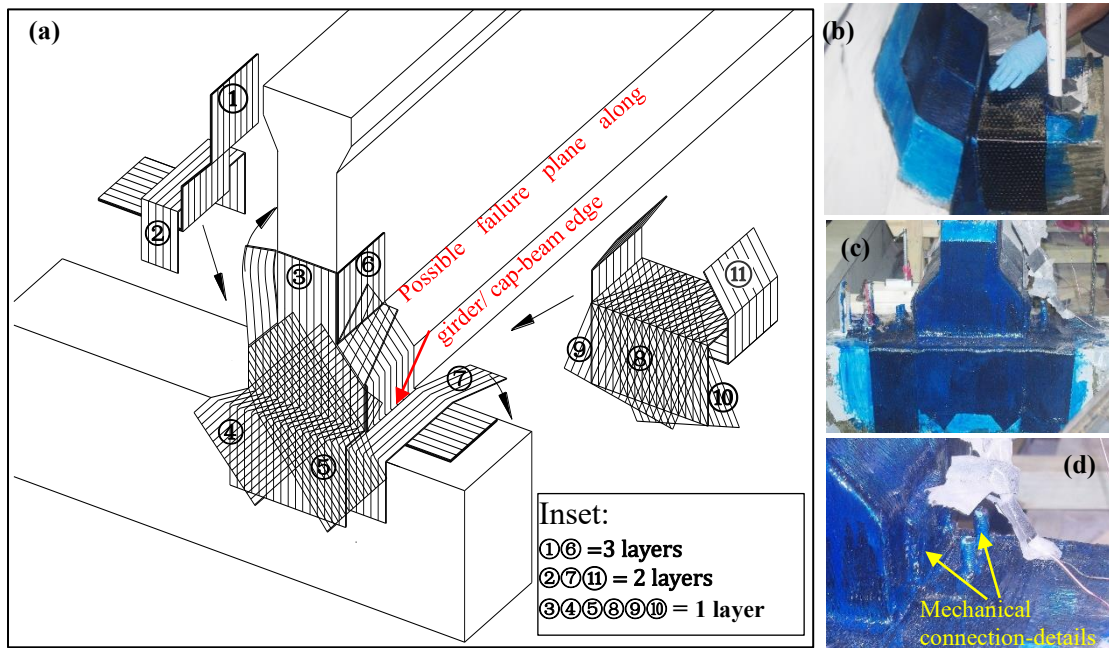


Fig. 4. CF/E procedure for retrofitting the mechanical connection-detail in concrete girders, showing (a) sequential fiber lay-up; (b) carbon-fiber applied to a girder-end that has no existing mechanical connections; (c) final CF/E lay-up; and (d) CF/E applied around mechanical connections (note: following CF/E lay-up, C-IEPM may be manufactured by spraying polyurea to the wet (curing) epoxy surfaces in (c) and (d))

Experimental Test Setup and Instrumentation

Wave height and period are two critical parameters used to calculate wave and surge forces [7, 35, 36]. The maximum wave elevation during Hurricane Katrina in Mobile Bay was recorded as 7 m [37]. A wave load cycle of eight to ten seconds (duration) may be interpolated using the relationship between maximum wave height and simulated wave periods, designed using probability density functions of 100-year return-period occurrences in the Gulf of Mexico [38]. Assuming a 9-sec period and using a 250 kN capacity dynamic hydraulic actuator with a rotating / swivel head, a combined hurricane-induced load function for wave and surge forces was determined in accordance with the superimposed profile in **Fig. 5d** [39].

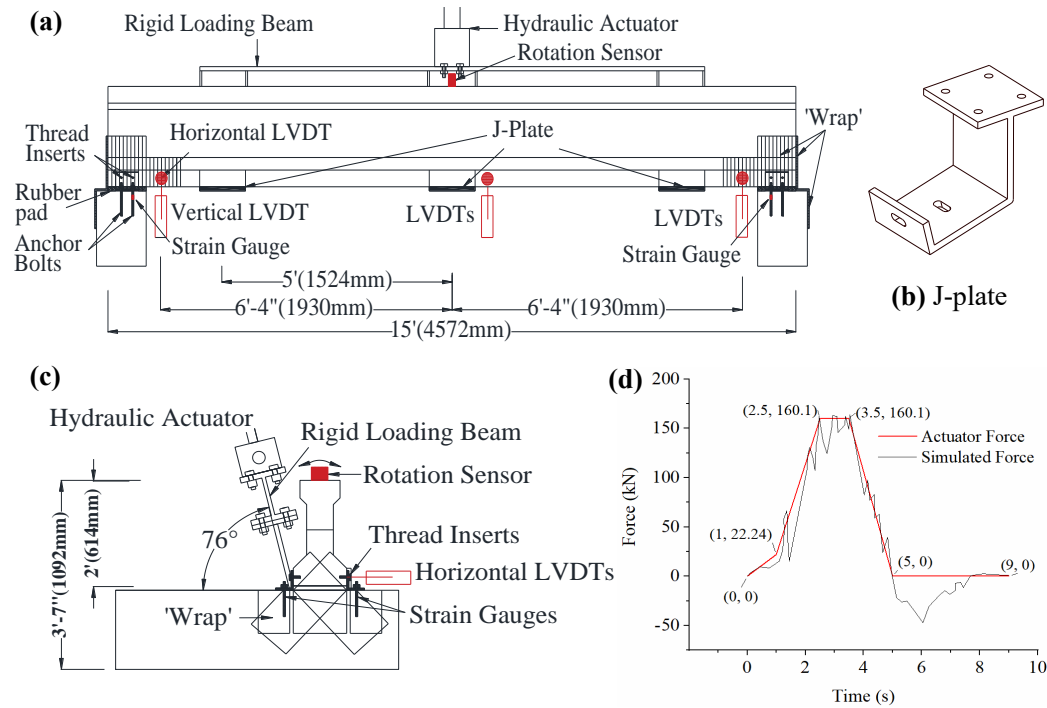


Fig. 5. Laboratory test set-up, showing **(a)** actuator force applied to the test girder via rigid steel beam connected to the girder at three points; **(b)** profile view of the actuator loading angle; **(c)** J-plate; and **(d)** Modified (lab-scale) Hurricane Katrina wave forcing function produced by the actuator (red) that models the desired theoretical wave load according to the modified Douglass function [5,31]

The peak actuator force was calculated as 160.1 kN, or $\frac{1}{4}$ -scale of the actual (non-scaled) peak force for Hurricane Katrina. The force-controlled load function was comprised of a 5-second loading cycle (where wave load rises for 2.5 sec, remains constant for 1 sec, then retracts for 1.5 sec) and 4 seconds of load acquiescence. The “red” load function in **Fig. 5d** was applied to each Test Girder (TG) using a ‘rigid steel loading beam’ that was anchored at three positions, see **Fig. 5a**, using three “J-plate” connectors, see **Fig. 5b**. The connection-details in **Table 1** and shear stresses near the girder-ends were designed in accordance with a stress similarity analysis of the field-designed girders using forces of 566.3 kN (vertical) and 150.3 kN (horizontal) that were calculated using the modified Douglass equation [5,31] and that also accounted for girder and tributary-deck weight [7]. Simulations were used to confirm that five-point loading, facilitated through the rigid steel beam, may be used to model a uniform wave-and-surge combined loading accurately. In this case, the actuator was positioned at $\theta = 76^\circ$ relative to a horizontal plane, see **Fig. 5c**, resolving components into simultaneous surge (vertical) and slamming wave (vertical and lateral) loads through the rotational actuator head. These loads were transferred primarily to the connection-details of each test girder [14, 15, 17].

This study focuses on enhancing the connection-details in coastal bridges. Six lab-scale test girders, without deck-bracing, were conservatively designed using reinforced concrete (instead of prestressed concrete) and tested in the structural high-bay laboratory. The test girders (TG) and their retrofit schemes are summarized in **Table 2**.

Pre-Katrina and Post-Katrina TG were designed in accordance with ALDOT design specifications [31] and using in-field measurements of the I-10 bridge. For interior-span girders freely resting on their cap-beams, where neither girder-end is mechanically

attached, connection-details of a C-IEPM_0 TG ($t_c = 2.5$ hr) were strengthened at both ends with C-IEPM using a plain weave (PW) bi-directional fiber (ACP Composites®, 127 g/ m², 3,654 MPa tensile strength, 0.23 mm/ ply fiber thickness) with a nominal strength of 2.503 kN / mm, see **Table 2**. The connection-details of C-IEPM_1 TG ($t_c = 2.5$ hr) include mechanical connections at one end to allow for expansion and to provide a positive moment for exterior-span girders that are subject to large surge and wave-impact forces; in this design, both girder-ends are strengthened using C-IEPM. **Fig. 4a** illustrates the fiber lay-up for C-IEPM_1 TG, which uses a uni-directional fiber (BASF, The Chemical Company®, 600 g / m², 3.79 GPa tensile strength, 0.33 mm/ply fiber thickness) with nominal fiber-strength of 2.17 kN / mm along the girder/ cap-beam edge, see **Table 2**.

Table 2

Design details and cyclic load-response features of the tested specimens

Specimen Name	Connection-Detail	Fiber (Thickness), Load Strength / Fiber-Width	Type	Maximum Load (kN)	Cycle No. at Failure
Pre-Katrina TG	Inserts both ends	—		60.0	1
Post-Katrina TG	Thru-bolts both ends	—		88.2	1
C-IEPM_0 TG	C-IEPM both ends	ACP PW (0.57 mm), 2.17 kN/mm (along girder/cap edge)	Periodic dynamic, Fig 5(d)	54.9	1
C-IEPM_1 TG	Left: C-IEPM and mech. connections Right: C-IEPM	FIB 600/50 CFS (0.66 mm), 2.503 kN/mm (along girder/cap edge)		142.4	1
CF/ E TG	CF/E Wrap and mech. connections both ends	FIB 600/50 CFS (0.66 mm), 2.503 kN/mm (along girder/cap edge)		160	10
C-IEPM_2 TG	C-IEPM and mech. connections both ends	FIB 600/50 CFS (0.66 mm), 2.503 kN/mm (along girder/cap edge)		160	12

Experimental Results and Discussion

Dynamic response of the test girders (TG)

Using the target load function in **Fig. 5d**, the force-displacement curves of six 4.57 m long lab-scale test girders, see the lab setup in **Figs. 5a** and **5c**, were recorded using the load cell attached to the actuator and six LVDTs. Load-displacement relationships at mid-span of Pre-Katrina TG, Post-Katrina TG, and C-IEPM_0 TG ($t_c = 2.5$ hr) indicate that the connection-details experienced significant failure in less than 1.5 sec of the first loading cycle, or about one-fourth of the 5-second loading cycle, see **Fig. 5d**.

After experiencing some plateauing for slightly longer than 0.5 seconds, see **Fig. 6**, the three systems failed after about 2 seconds of loading, or less than one-half of a loading cycle, sustaining a failure load of about 28.6 kN. The failure mechanism in each case was the shear failure of the concrete. However, connection-details of C-IEPM_1 TG ($t_c = 2.5$ hr) performed better. Failure of the girder-end sans mechanical connections occurred at significantly larger force (119.4 kN) at 2.02 sec and was followed by the initial failure of the mechanically connected girder-end between 2.33 sec and 2.37 sec. The onset of plateauing then occurred at 2.50 sec, according to **Fig. 5d**. A sustained force of 142.4 kN was supported for approximately 0.67 seconds until the mechanically connected girder-end completed its failure in shear after about one-half loading cycle. After the sudden decrease in force, the sustained force of 33.3 kN was found to be slightly larger than that of Pre-Katrina TG, Post-Katrina TG, and C-IEPM_0 TG (28.6 kN) and also included slightly larger ductility. Interestingly, the increase in maximum force in C-IEPM_1 TG (142.4 kN), ranging from 68% to 146% larger than the maximum force in Pre-Katrina TG, Post-Katrina TG, and C-IEPM_0 TG, emphasizes an important point: Although the strengths of the carbon-fiber in C-IEPM_0 TG and C-IEPM_1 TG are similarly weak in shear [16], if the

connection-details of girders can include, as a minimum, weak-in-shear mechanical connections, e.g., Pre-Katrina TG and C-IEPM_1 TG, then supplementing the connection-details with IEPM can (1) engage the underlying concrete to the fiber, and (2) sufficiently distribute the wave load to the fiber and also transfer load energy via its material damping mechanism (thus reducing stress concentrations to the fiber). This effectually enhances shear resistance of C-IEPM and reduces the propensity of fiber delamination, thus markedly improving structural performance (compare C-IEPM_1 TG to C-IEPM_0 TG in **Fig. 6**). This is evidenced in C-IEPM_1 whose initial failure force in the non-mechanically anchored girder-end is 119.4 kN, or 97% to 115% larger than the maximum force in Pre-Katrina TG, Post-Katrina TG, and C-IEPM_0 TG, see **Table 2**. This leads to an important finding, that in a dynamic and high-shear demand environment, C-IEPM is most effective when an additional system – even weak mechanical connections – helps to facilitate rapid engagement between C-IEPM and the underlying substrate (in this case, concrete).

A comparison between C-IEPM_2 TG ($t_c=1.5$ hr) and CF/E TG in **Fig. 6** revealed that although CF/E-strengthened connection-details (and mechanical connections at both girder-ends) help the girder to achieve a target load of 160.1 kN, the girder is unable to survive one loading cycle without experiencing substantial damage. The initial failure of CF/E TG occurred after the load had plateaued for about the same amount of time (0.65 sec) as C-IEPM_1 TG did, once the mechanically connected-end of the former girder failed (after 0.67 sec elapsed time). After approximately 3 sec of plateauing, the strength of CF/E TG sharply decreased, unable to recover its target load of 160.1 kN before the wave load retracted. Although damage to CF/E TG was less than in C-IEPM_1 TG, both systems slightly did recover after their sudden decrease in strength. In subsequent loading cycles,

the aggrandized amount of carbon-fiber used to design CF/E TG provided “reserve” strength. Along with new principal materials axes, the girder was able to “recover” a portion of the inelastic deflection incurred after each cycle.

C-IEPM-2 TG ($t_c = 1.5$ hr) clearly survived load cycle 1, quickly surpassing the performance of CF/E TG. Because of the shorter curing time that was used ($t_c = 1.5$ hr), IEPM was able to transfer sufficient energy via requisite material damping that helped the C-IEPM-strengthened connection-detail to engage with the concrete substrate, thus highlighting the importance of t_c (in C-IEPM_2 TG versus C-IEPM_1 TG). As a result, C-IEPM_2 TG survived a total of 12 loading cycles, and its hysteresees stabilized after three loading cycles. However, the hysteresees curves (and structural damage) of CF/E TG failed to stabilize due to the brittle nature of CF/E after the girder had efficaciously failed during cycle No. 1, see **Fig. 6**.

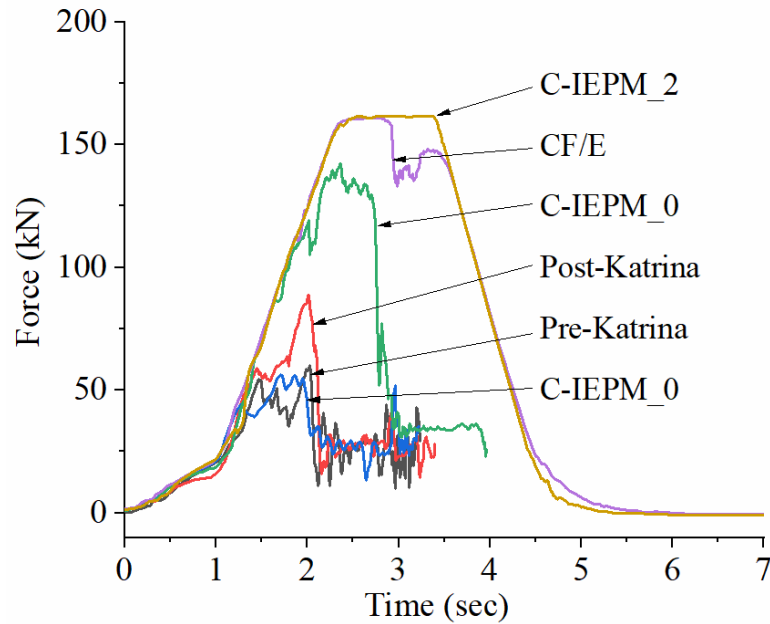


Fig. 6. Force (mid-span) time-history of cycle 1 for the six test girders (TG)
Comparison between Pre-Katrina TG and Post-Katrina TG

Force time-history. **Fig. 7** depicts a rapid failure for Pre-Katrina TG, with one connection-

detail failing after 1.47 sec (54.4 kN), then with some “plateauing” marked by a decrease in force to 33.6 kN. This was followed by system hardening, or load increase after damage (recovery), as the threaded inserts remained partially embedded in the concrete. The right girder-end completely disengaged from its cap-beam when the second connection-detail failed 56 seconds later at 2.03 sec and 60.0 kN. The failure mode for each connection was a sudden shear failure of the concrete surrounding the threaded inserts / screwed bolts, see **Figs. 8a** and **8b**. The findings are consistent with damage modes observed in-the-field following Hurricane Katrina [10]. The Post-Katrina TG, designed following the connection-details in **Fig. 3b**, also experienced sudden shear failure of concrete surrounding the anchor bolts as a primary mode of failure, where one girder-end failed at a slightly larger initial force (59.0 kN versus 54.4 kN) at 1.45 sec, leading to only a slight decrease in force (53.82 kN), likely due to the ductility of the embedded threaded through-bolts, see **Fig. 8c**. The use of through-bolts engaged a larger concrete region, generating a 52% increase in maximum force in Post-Katrina TG (88.2 kN) relative to Pre-Katrina TG (60.0 kips), see **Table 2**, but at a similar time of loading (2.01 sec versus 2.03 sec).

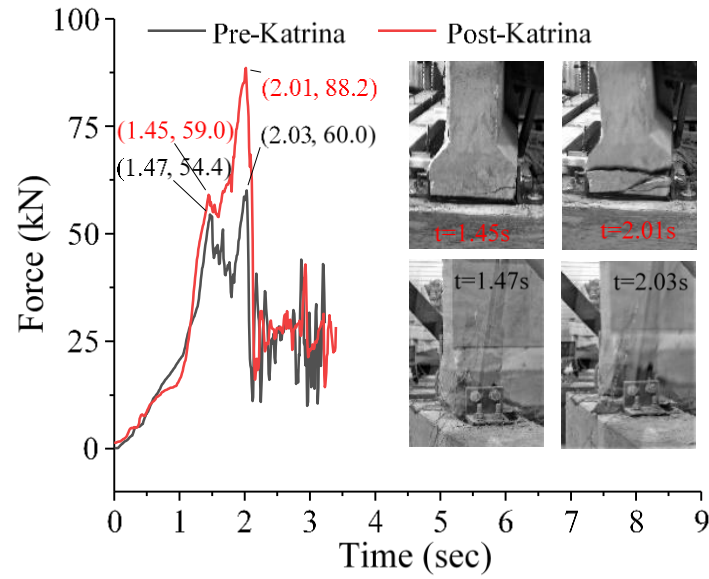


Fig. 7. Dynamic response of Pre-Katrina and Post-Katrina connection



Fig. 8. Shear failure modes of (a) and (b) Pre-Katrina TG; and (c) and (d) Post Katrina TG where ductile behavior of through-bolts allow maximum force of 88.2 kN to be recovered until concrete fails in shear

Force-deflection and energy dissipation. Post-Katrina TG and Pre-Katrina TG failed within the first half-cycle of loading, well below the maximum target force of 160.1 kN, and at similar ultimate mid-span deflection (59 mm and 62 mm, respectively). Additionally, the force-deflection relationship for Post-Katrina TG reveals a substantial difference in energy dissipation (area under the curve), and although yield strength had marginally increased (59.0 kN versus 54.4 kN), yield deflection increased from 12.8 mm to 20.1 mm, see **Figs. 7 and 9**, likely because of the extra slip perpetrated via the through-bolts. However, the maximum (peak) force of 88.2 kN is 45% less than the target peak strength (160.1 kN). However, with similar ultimate deflections, displacement ductility (μ_d) for Post-Katrina TG, which is the ratio of ultimate deflection to yield deflection in **Figs. 7 and 9**, is 33% lower ($\mu_{d,Post} = 3.08$ versus $\mu_{d,Pre} = 4.61$). However, system strain hardening provided by the through-bolts increased energy dissipation by over 70% in Post-Katrina TG, substantially improving damage tolerance. Therefore, while the Post-Katrina TG connection-detail is an improvement over the conventional Pre-Katrina TG detail, it does not improve the existing limit state (catastrophic failure) of typical bridge spans in harsh storm environments.

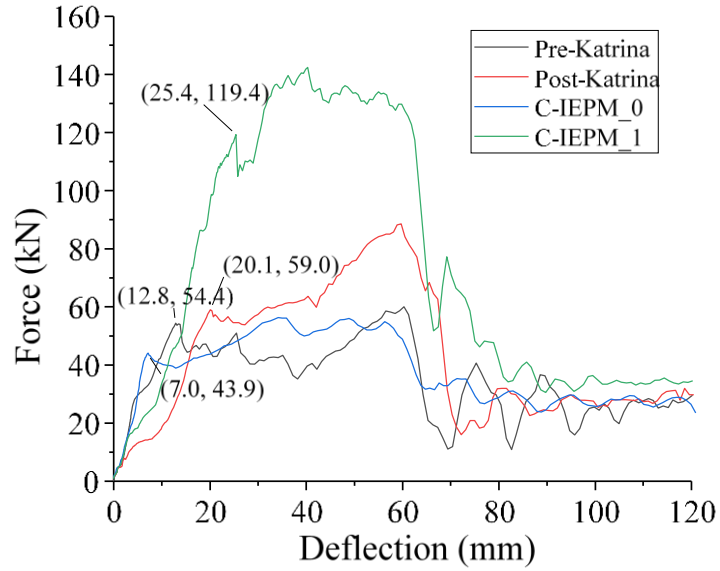


Fig. 9. Comparison of force-displacement behavior of Pre-Katrina TG, as-is) and test girder 2 (post-Katrina)

C-IEPM-strengthened connection-details with and without mechanical anchors

C-IEPM- or CF/E- strengthened connection-details are comprised of mechanical connectors, concrete, and either C-IEPM or CF/E, see **Fig. 11a**, leading to a combined stress mode that ultimately leads to a shear failure mode. Failure of C-IEPM_1 TG begins at 2.02 sec at 119.4 kN (non-mechanically-connected girder-end), and failure of C-IEPM_0 begins at 1.29 sec at 44.4 kN. After incurring initial failure, the resistant force in each girder was able to increase due to system hardening, see **Fig. 10**, which was also evinced in Post-Katrina TG and Pre-Katrina TG, see **Fig. 7** (although the substantial strength-decrease in Pre-Katrina TG delimited the subsequent increase in load). The load-increase helped C-IEPM_1 TG to nearly reach the targeted peak plateau load (160.1 kN, **Fig. 10**) at 2.50 sec (**Fig. 5d**), whereas C-IEPM_0 TG could not. This is significant because without the presence of even a weak Pre-Katrina-designed mechanical anchor, C-IEPM_0 TG behaved comparably to Pre-Katrina TG or Post-Katrina TG, where the concrete substrate could only

minimally engage with the strengthening mechanism, where, in the case of C-IEPM_0 TG, transfer of load energy (via IEPM material damping) and load distribution to the fiber were limited. At 1.61 sec, failure in C-IEPM_0 TG also initiated in the second girder-end, and a load of 54.9 kN was sustained until complete shear failure occurred at 1.95 sec, see **Figs. 11a** and **11b**. Conversely, C-IEPM_1 TG resisted a significantly larger initial connection failure force (119.4 kN versus 44.4 kN) relative to C-IEPM_0 TG, despite having one non-mechanically connected girder-end and one Pre-Katrina mechanically connected end (initial failure at 54.4 kN), where even a weak anchorage-system bided time for the underlying concrete to engage with C-IEPM. As a result, material damping in IEPM helps to transfer enough of the load-energy at both girder-ends, resulting in a significantly larger initial failure force (119.4 kN). When the non-mechanically connected girder-end finally failed at 2.02 sec, the wave load was immediately and solely resisted by the mechanically connected girder-end (see the vertical relationship in **Fig. 10**), which subsequently failed (initially) between 2.33 sec and 2.37 sec. A maximum force of 142.4 kN was then sustained until final failure occurred at 2.68 sec (compared to 54.9 kN in C-IEPM_0 TG). The C-IEPM_1 TG experiment was stopped prematurely due to excessive physical rotation about the mechanically connected girder-end, see **Figs. 10** and **11d**. Except for some concrete cracking that was observed around the thread bolts, no surface damage was observed around the mechanically connected end, see **Fig. 11c**. CF/E-strengthened connection-details are comprised of mechanical connectors, concrete, and C-IEPM, see **Fig. 11e**, leading to a combined stress mode. The maximum force in C-IEPM_1 TG was conservatively calculated as 268.9% larger (at the non-mechanical girder-end) and 259.4% larger than the maximum resistance in C-IEPM_0 TG, clearly highlighting the ability of

C-IEPM to transfer energy after engaging with the underlying concrete. As a measure of greater perspective, initial and final connection failure forces in C-IEPM_1 TG (119.4 kN and 142.4 kN) are over 120% greater than forces in a ‘hypothetically combined’ Pre-Katrina TG (54.4 kN and 60.0 kN) and C-IEPM-0_TG (44.4 kN and 54.9 kN) system. Additionally, the experimental test for C-IEPM_1 TG was stopped at a force (142.4 kN) that was still 54.2 kN larger than the maximum force in Post-Katrina TG (88.2 kN), signifying that although C-IEPM can overcome shear strength limitations of conventional CF/ E [40], it appears that large shear forces induced by hurricane wave loads require a combination of C-IEPM and a common mechanical connection, e.g., steel anchors and clip angle.

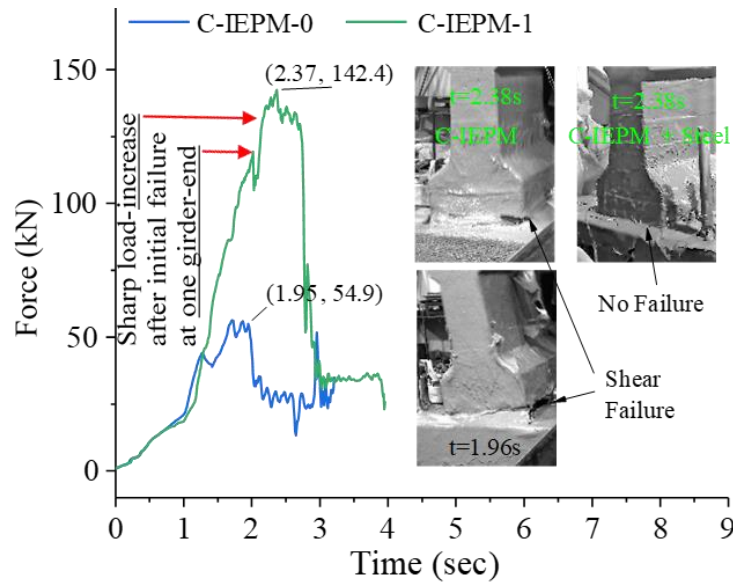


Fig. 10. Actuator force-time history of C-IEPM_0 and C-IEPM_1. C-IEPM_1 TG experienced minimal damage to the connected-end when the wave-load experiment was stopped at 2.38 sec due to shear damage and girder rotation at the non-mechanically connected-end. In C-IEPM_0, the girder failed initially at 1.29 sec; the second non-mechanically girder-end experienced initial failure at 1.61 sec, with a sustained load of about 54.9 kN for 34 seconds until complete disengagement of the girder from its cap-beam

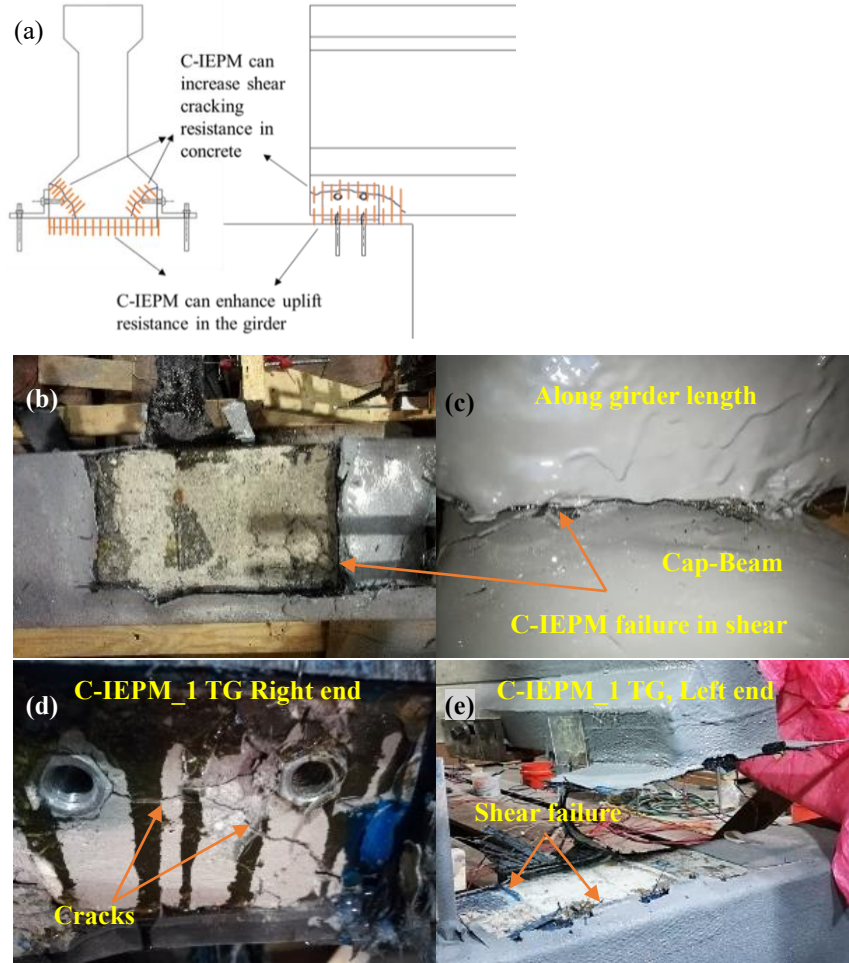


Fig. 11. (a) Depiction of connection-detail strengthening system, comprised of either C-IEPM or CF/E composite and mechanical connectors joining the concrete girder and cap-beam; (b and c) Shear failure observed in C-IEPM (C-IEPM_0 TG); (d) concrete shear failure at non-mechanically connected left girder-end (cap-beam) of C-IEPM_1 TG; (e) C-IEPM shear failure at non-mechanically connected girder-end in C-IEPM_1 TG

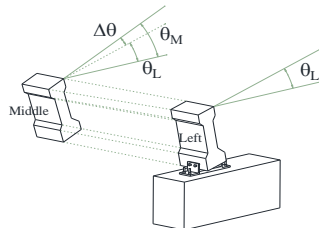
Comparison of C-IEPM_2 and CF/E as retrofitting or strengthening materials

The girder designs for CF/E TG and C-IEPM_2 TG include “pre-Katrina” type mechanical connections at both girder-ends. A high-speed camera is used to capture progressive damage states of the left-end connection-detail of each test girder, see **Fig. 12**, depicting force-time test results after the 1st, 2nd, 3rd, and 10th cycles. Rotations (θ°) of girder cross-sections were calculated at the left girder-end, middle of the girder, and right girder-end; the results are summarized in **Table 3**. During cycle No. 1, after reaching its peak force (160.1 kN), excessive damage to CF/E TG precluded recovery of the peak force, which is indicated by the “flat” force-time plot just prior to unloading, **Fig. 12a**.

Table 3

Rotation angle of CF/ E and C-IEPM at the peak of each cycle

Cycle No.	Rotation Angle (θ°), CF/ E TG			Rotation Angle (θ°), C-IEPM_2 TG		
	Left end (θ_L)	Middle (θ_M)	$\Delta\theta$	Left end (θ_L)	Middle (θ_M)	$\Delta\theta$
1	5.26	5.34	0.08	1.06	1.26	0.20
2	7.35	7.40	0.05	9.07	9.57	0.51
3	10.07	9.98	-0.09	11.74	12.28	0.54
4	11.06	11.19	0.13	13.13	12.62	0.52
5	12.22	12.25	0.03	12.89	12.89	0.51
6	13.37	13.39	0.02	13.09	13.63	0.54
7	13.99	14.01	0.03	13.30	13.86	0.57
8	15.87	15.87	0.00	13.48	14.08	0.59
9	17.72	17.72	0.00	13.67	14.29	0.62
10				13.85	14.50	0.65
11				14.08	14.76	0.68
12				14.56	15.27	0.71



This conclusion is supported by the large rotation experienced by the left girder-

end ($\theta_L = 5.26^\circ$) and middle girder cross-section ($\theta_M = 5.34^\circ$) of CF/E TG, which lacked a cogent mechanism for transferring the input energy (dissipating it away). In contrast, rotations experienced by C-IEPM_2 TG were only $\theta_L = 1.06^\circ$ and $\theta_M = 1.26^\circ$ during cycle No. 1, and although cross-section rotations in cycle No. 2 were substantially larger, exceeding 9° see **Table 3**, input wave energy was absorbed through the bending modes of the IEPM chemical bonds. This efficaciously minimized girder damage, thus stabilizing it and relegating it locally; consequently, C-IEPM_2 TG was able to recover and harden (see the load increase following damage, i.e., “positive” tending force-time plot in **Fig. 12b**).

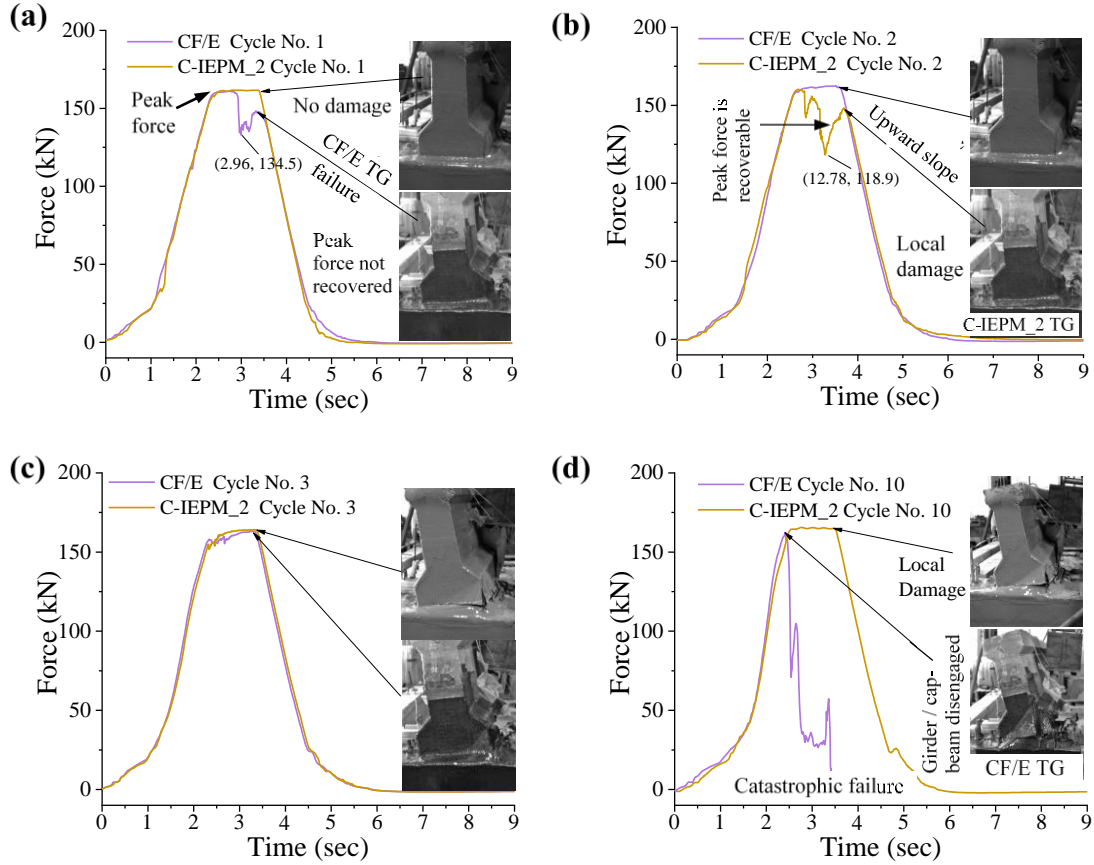


Fig. 12. Force time-histories of C-IEPM_2 TG at four loading cycle
In cycle No. 3, θ_L and θ_M for CF/E TG and C-IEPM_2 TG increased by over 35%

and 30%, respectively, relative to cycle No. 2. Due to the material damping in C-IEPM_2

TG, the transient component of the response hysteresees started to stabilize as the response approached steady-state form. As a result, the per-cycle increase in θ diminished substantially ($\sim 1\%$). This was not evident in the CF/E TG response as θ continued to increase between 5% and 15% in subsequent load cycles until the girder finally disengaged from its cap-beam in cycle No. 10, resulting in catastrophic failure.

Table 3 also shows that the angle of twist, $\Delta\theta$ ($\Delta\theta$ = rotation of middle cross-section relative to girder-end rotation, see the inset in **Table 3**), per cycle is fairly constant for C-IEPM_2 TG and CF/E TG. Two observations are made: (1) $\Delta\theta$ is very small ($\Delta\theta \approx 0$) for CF/E TG, indicating shear failure of the connection-details during cycle No.1 and near-zero rotational, or torque ($\propto \Delta\theta$), resistance during the 10 cycles (the girder essentially rotates as a rigid body); (2) $\Delta\theta$ for C-IEPM_2 TG is significant, indicating (i) rotational resistance; (ii) local damage, e.g., cracking of the connection-details, see **Figs. 13c** and **13d**; and (iii) minimal service limit state; (3) θ_L in CF/E TG consistently increases, indicating that damage to the connection-details steadily accumulates until the girder disengages from its cap-beams during cycle No. 10, see **Figs. 12d, 13a, and 13b**; and (4) θ_L in C-IEPM_2 TG stabilizes, thus minimally changing from cycle-to-cycle.

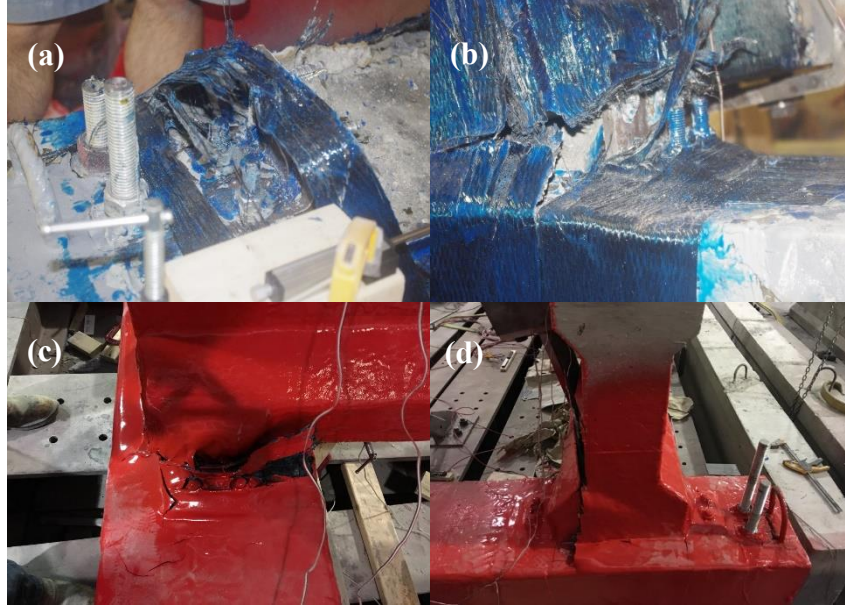


Fig. 13. (a) and (b) Damage observed in CF/E TG, showing that the connection-details fail at multiple locations, exhibiting fiber breakage, CF/ E delamination, concrete shear failure (at the locations of threaded inserts in the girder), and yielding of threaded anchor bolts (in the inserts); and (c) and (d): Local damage in C-IEPM_2 TG after 12 load cycles, seen only on one girder-end

Nature of the energy dissipation through C-IEPM and CF/E. When the second load cycle unloads after ~12 sec, the mid-span deflection of C-IEPM_2 TG is 10.2 mm greater than the deflection of CF/E TG (53.3 mm), see **Figs. 14a - c**. The upward trending hysteresees of C-IEPM_2 TG is visible during cycle No. 2, with a relative deflection of ~ 45 mm (unload point to unload point between load cycle No. 1 and load cycle No. 2); the upward trend continues in cycle No. 3. In contrast, the hysteresees curve for CF/E TG in cycle No. 1 does not recover its peak force, indicating excessive damage to the girder which is consistent with the results in **Table 3**. However, the large amount of fiber and reserve material strength in CF/E TG facilitates the redistribution of load that takes place after cycle No. 1 and a change in principal materials axes, effectually helping the peak hysteresis force to achieve the peak force of 160.1 kN during load cycle No. 2.

Fig. 14c compares maximum mid-span deflections per cycle for CF/E TG and C-IEPM_2 TG. Although the connection-details of Pre-Katrina TG and Post-Katrina TG had failed catastrophically at mid-span deflections of 62 mm and 59 mm, the ultimate mid-span deflections in CF/E TG and C-IEPM_2 TG (which did not fail) were 102 mm and 88 mm. C-IEPM advents ductility and energy transferability (energy absorption/dissipation) in C-IEPM_2 TG, stymying the bridging of local damage and thus facilitating deflection recovery and hysteresees stabilization so that peak-to-peak deflections only minimally changed, thus averting major global damage. However, while C-IEPM appears to be a viable retrofit or strengthening option, the presence of simple mechanical connections and use of smaller t_c can enhance the ability of C-IEPM to engage with the underlying concrete substrate: compare C-IEPM_2 TG ($t_c = 1.5$ hr) in **Fig. 13a** to C-IEPM_1 ($t_c = 2.5$ hr) and C-IEPM_0 ($t_c = 2.5$ hr) in **Fig. 10**. **Fig. 14c** also shows that the change in mid-span deflection per cycle in C-IEPM_2 TG quickly approaches zero, approaching a cumulative maximum after cycle No. 3; mid-span velocity also diminishes quickly after cycle No. 3 because of the material damping infused via C-IEPM. Without substantial material damping, the mid-span deflection per cycle in CF/E TG consistently increases, surpassing C-IEPM_2 TG after the first two cycles. As a result, the velocity in CF/E TG remains nearly constant at 1.25 mm/ sec, until the girder completely disengages from its cap-beams after three load cycles, the accumulated hysteresis energy (areas under the hysteresis curves) of C-IEPM_2 TG and CF/E TG are similar, 8,176 joules (J) and 8,248 J, respectively.

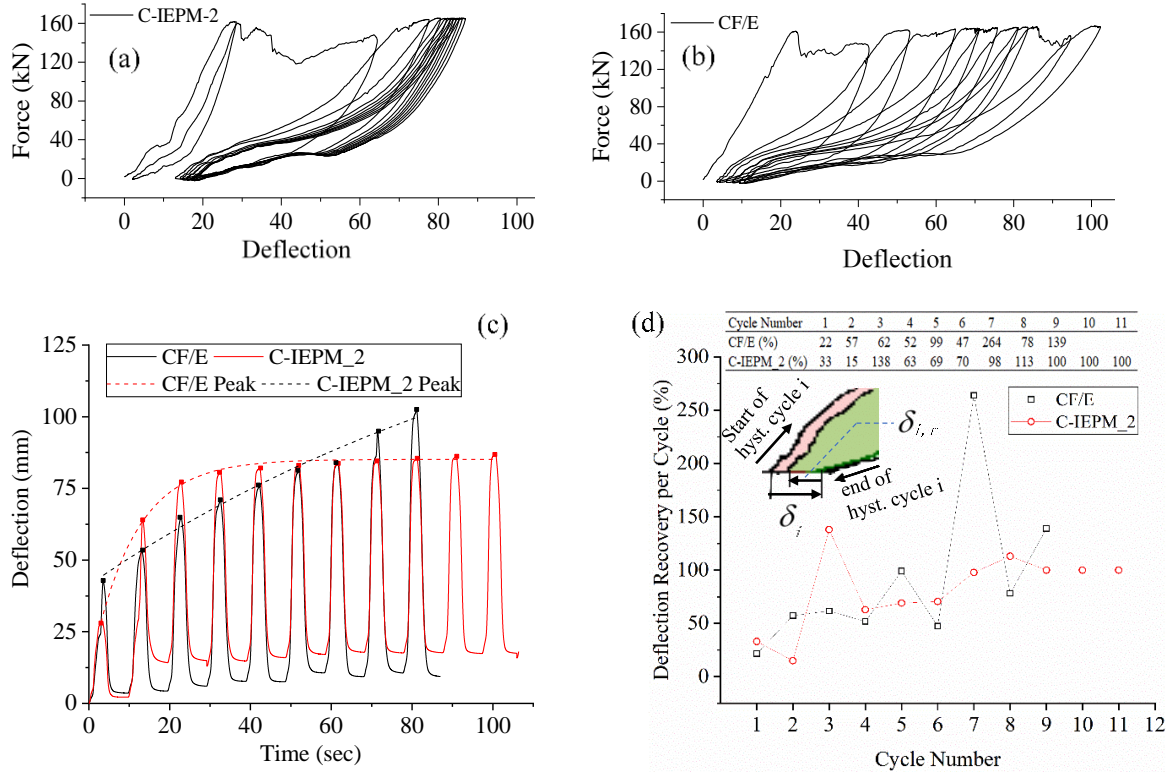


Fig. 14. (a, b) Hystereses of C-IEPM_2 TG and CF/E TG, where material damping in IEPM helps to stabilize the response in C-IEPM_2 TG after 3 or 4 cycles, thus preserving girder integrity and minimizing the service limit state (to local damage / cracking); (c) a comparison of peak mid-span girder deflections, per cycle, showing that C-IEPM_2 TG quickly stabilizes (constant) while CF/E TG deflections, without a substantial damping mechanism, consistently increase until sudden disengagement; and (d) Displacement recovered per cycle (%), calculated at end of cycle relative to gross cycle displacement

Table 4 summarizes the accumulated energy (J) after each cycle. In C-IEPM_2 TG, the transfer (“dissipation”) of incoming wave energy occurs through bond-motion modes, such as bending, twisting, or stretching modes [41,42], eliciting molecular vibrational properties that attribute to bulk properties, such as material damping and fracture toughness, that help to stabilize damage (including the large amount of energy after cycle No. 2) and control the calculated area (dissipated energy) under the hystereses of C-IEPM_2 TG, thus resulting only in local cracking of the concrete and C-IEPM at the

connection-detail. By enhancing damage tolerance in C-IEPM_2 TG via IEPM, microscopically weak individual structures (individual cracks) can be integrated into a macroscopically strong solid, thus minimizing harm to the overall girder. In other words, the chaining of damage events that could lead to failure of the composite system is inhibited. Instead, global failure of the connection-detail (and girder) may finally occur after a significant number of individual “stabilized damage events” eventually inter-connect, thus utilizing the full structural redundancy (force resistance) of the system until, for example, concrete shear failure, pull-out failure, or steel (anchor) tensile failure occurs [27].

Table 4

Accumulated energy after the i th cycle (summed area under each hysteresis curve) for CF/E TG and C-IEPM_2 TG

Cycle No. i	1	2	3	4	5	6	7	8	9	10
TG										
CF/E (J)	3296	5521	8248	10629	12691	14810	16652	19370	21562	31266
C-IEPM_2 (J)	1036	5757	8176	10173	11800	13361	14860	16270	17705	19135

Physically, C-IEPM_2 TG inherits strength sustainability and resiliency, where its response (displacement and rotation) quickly stabilizes. Conversely, due to a lack of inherent material damping and fracture toughness in CF/E TG, its hystereses curves remain transient (i.e., failing to reach a steady-state), thus hindering stability of the girder response. As a result, damage accumulates until the girder eventually fails catastrophically. By introducing a substantial amount of material damping via IEPM into the girder, the

transient component of the dynamic response is quickly eliminated, i.e., incoming wave energy per cycle is transferred (“dissipated”), and the steady-state component that remains confirms that damage propagation is blunted and remains local.

The steady-state nature of the hystereses of C-IEPM_2 TG indicates that C-IEPM remains engaged with the concrete during loading, helping to transfer wave energy away from the weak mechanical connections, thus localizing damage. Although after three cycles the accumulated energies in C-IEPM_2 TG and CF/E TG are similar, after 10 cycles, the total energy in C-IEPM_2 TG tallies 40% less (19,135 J versus 31,266 J). This emphasizes a critical point, that although comparative areas under the hystereses curves are initially similar, the energy transfer mechanisms – bond-motion modes (IEPM) compared to brittle epoxy matrix cracking or fiber-breakage – are different. Therefore, physically, girder damage is manifested differently through failure modes according to each system’s properties. In the case of C-IEPM, a log-decrement analysis determined a damping ratio (ξ) of 4.87%, whereas $\xi = 1.18\%$ for CF/E [40], which greatly influences each girder’s serviceable limit state and overall health.

Fig. 14d shows the recoverable percent deflection per cycle, defined in Equation (1) as

$$\Delta_R = \frac{\delta_{i,r}}{\delta_i} \times 100 \quad (1)$$

where Δ_R (as a per-cent) is the ratio of $\delta_{i,r}$ (amount of recovered deflection at the end of hysteresis cycle No. i (signified by zero force) just prior to loading of cycle No. $i+1$) to δ_i (total deflection during hysteresis cycle No. i , measured from initial loading of hysteresis cycle i at zero force until load completely unloads at zero force). The deflection recovery is proportional to the “backstress.” For C-IEPM_2 TG’s hysteresis cycle No. 1, 33% (Δ_R)

of the cycle's total deflection (δ_i) is recovered, at which point, hysteresis cycle No. 2 begins. Starting with cycle No. 3 or cycle No. 4, Δ_R increases considerably as the hystereses tend towards steady-state. Further, the accumulated energy that is dissipated per cycle is comparatively smaller than that in CF/E TG. The transient hystereses in CF/E TG in conjunction with the sporadic values of Δ_R (62, 52, 99, 47, 264, 78, 139) – albeit large values starting with cycle No. 5 – indicated that damage quickly accumulated, where the proximate start of each hysteresis curve, see **Fig. 14b**, reaches a comparatively larger (transient) peak-to-peak deflection. However, in C-IEPM_2 TG, damage was minimal, where start deflections are proximate (large Δ_R) after cycle No. 4 and also reach comparatively similar (steady-state) peak-to-peak deflections, see **Fig. 14a**.

Energy recovery via material strength reserve, material damping, and load distribution.

Fig. 15a uses the hystereses of consecutive cycles (after the girder-system yields), defined as cycle No. i and subsequent cycle (No. $i+1$), to illustrate how energy recovery can influence the behavior of each girder during hurricane wave loading. Due to the load distribution, material damping, and re-orientation of new principal materials axes that occurs after cycle No. i , a portion of the hysteresis energy may be recovered (see the 'dark green' region in **Fig. 15b**), netting an actual amount of "transferred," or dissipated, energy, manifested as girder damage during cycle No. i (see the 'pink' region in **Fig. 15b**). The recovered energy – and recovered displacement (**Fig. 14d**) – are essentially "put back into the structure" as it begins cycle (No. $i+1$), thus helping the girder response to stabilize. Examination of **Fig. 12a** and a comparison of **Figs. 14a** and **14b** reveal that material damping, through a well-designed IEPM, can differentiate between girder failure (CF/E

TG) and minimal damage / girder cracking (C-IEPM_2 TG) using equal quantities of fiber and for the same fiber orientation.

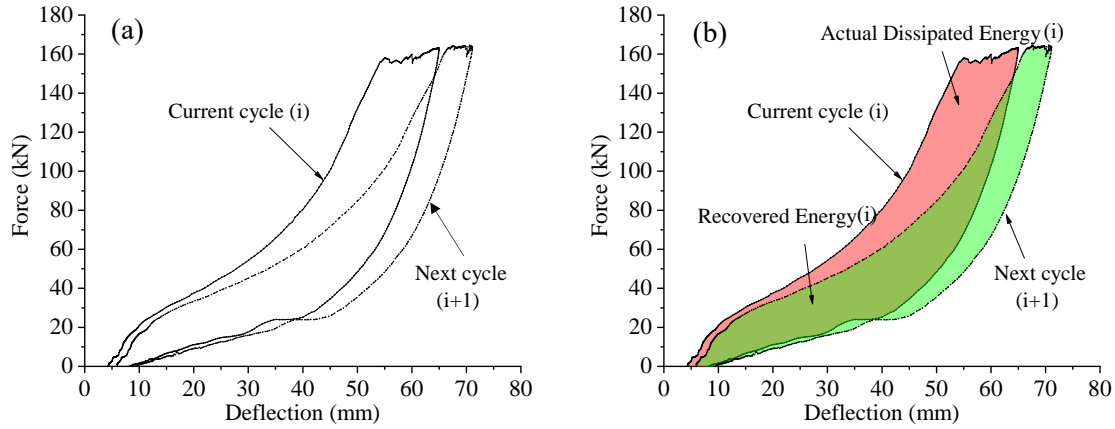


Fig. 15. (a) Illustration of energy dissipated per cycle, i and $i+1$; and **(b)** Distinction of actual and recovered energy

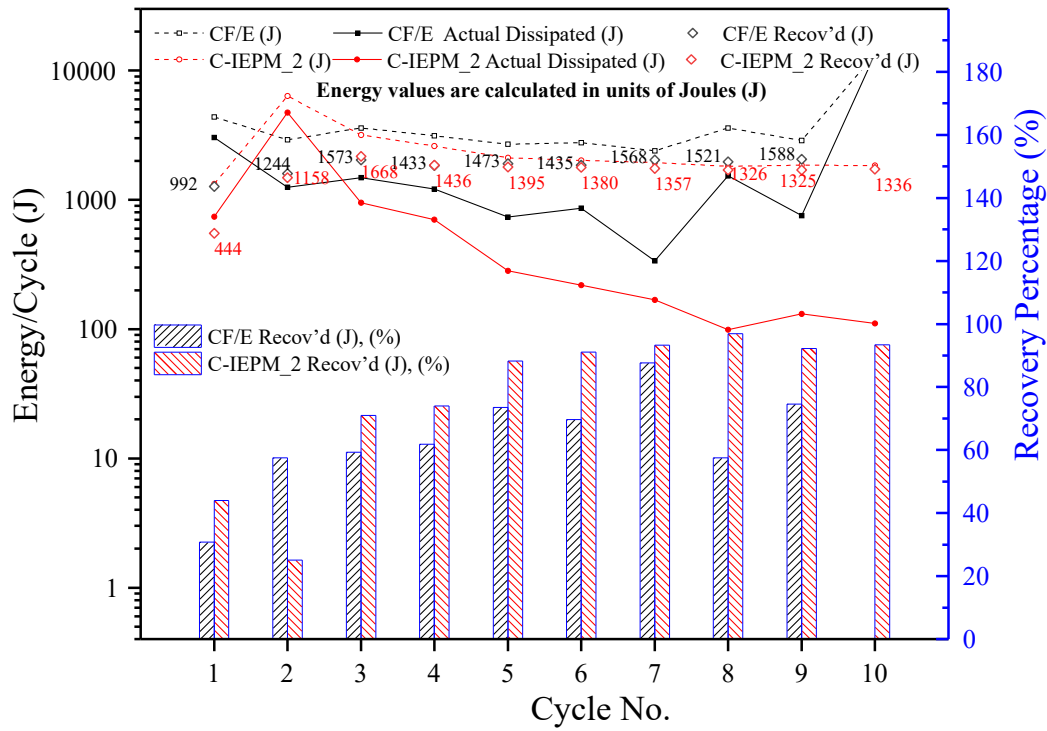


Fig. 16. Energy dissipation (J) and recovery per cycle of CF/E TG and C-IEPM_2 TG

The elastic stiffness of C-IEPM_2 TG was calculated as 6.17 MN/m (which is similar to 6.27 MN/m for C-IEPM_0 TG and C-IEPM_1 TG); for CF/E TG, it was 7.13 MN/m. However, the difference in performance for the test girders is attributed to the material damping provided by C-IEPM_2 ($t_c = 1.5$ hr), which is greater than the damping contribution by C-IEPM ($t_c = 2.5$ hr) [25], resulting in a more rapid reduction of peak-to-peak displacement (per cycle). Furthermore, the average increase in deflection per cycle for CF/E TG was calculated as 7.493 mm, whereas C-IEPM_2 TG, it was 0.914 mm per cycle, or 87.8% smaller. **Fig. 16** examines the energy dissipation (J) per hysteresis cycle. This area, illustrated in **Fig. 15a**, is consistently larger for CF/E TG, see the red and black dotted lines. Due to insufficient material damping, CF/E TG experienced excessive damage during cycle No. 1 and failed, where the peak load could not be re-achieved and therefore receding catastrophic girder failure. A comparison of red and black solid lines in **Fig. 16** gives a richer perspective of the accumulating girder damage, where actual damage per cycle (in accordance with the energy recovered) was significantly less in C-IEPM_2 TG. Furthermore, **Fig. 16** indicates that in C-IEPM_2 TG, the amount of recovered energy per cycle tends towards 100%, whereas a lack of essential material damping in CF/E TG delimited the amount of recovered energy. This is manifested by the transient nature of the hystereses, which, by failing to stabilize (**Fig. 14b**), adumbrates complete detachment of the girder from its cap-beam supports.

Discussion of Fracture Energy in C-IEPM and CF/E

Pre-Katrina and Post-Katrina connection-details were insufficient against estimated maximum Hurricane Katrina wave-induced forces (scaled), **Fig. 5**. The dominant failure

mode of each test girder was shear failure of the brittle concrete surrounding the yielded short bolts / threaded inserts (Pre-Katrina) and horizontal through-bolts (Post-Katrina). As a remedy, high-strength carbon-fiber in CF/E or C-IEPM was used to enhance each girder's shear resistance (see **Fig. 11a**) through its connection-details, starting with an arrangement of aligned fibers (see **Fig. 4**). Although carbon-fiber is weak in shear, an aggrandized amount of fiber through various orientations and in conjunction with “as-is” Pre-Katrina-designed mechanical anchors can help resist large shear forces. El Maaddawy and Sherif [43] used multiple orientations of carbon-fiber to wrap the connection-details of notched deep concrete beams (at girder-ends) under four-point bending, increasing shear strength by 72%. However, in the current hurricane study, dynamic multi-axial loading necessitated a substantial amount of fiber to design the connection-details of CF/E TG, yet nonetheless resulting in substantial fiber fracture and overall girder damage and failure after one loading cycle.

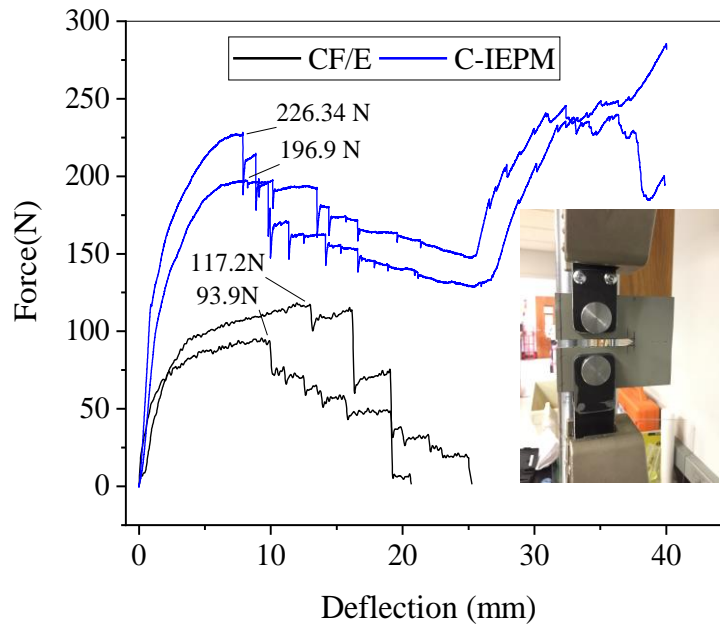


Fig. 17. Compact Tensile (CT) test load-displacement curves of coupon-scaled structures (a) CF/ E and (b) C-IEPM

A series of Compact Tension (CT) tests were performed in order to analyze the

fracture toughness provided by C-IEPM and CF/E. Two CF/E and two C-IEPM coupon-scale specimens (25 cm × 2.5 cm) were tested according to ASTM E1820 standards [44]. Each specimen was manufactured using 2 layers of thin (0.15 mm) plain-weave (bi-directional) carbon fiber. Load-deflection relationships are shown in **Fig. 17**. The results of the linear elastic fracture mechanics analysis are consistent with the test girder results presented earlier, which validate that C-IEPM ($t_c = 1.5$ hr) provides resilience and energy dissipation that CF/E alone cannot. By alleviating fiber delamination, thus sustaining high-fiber strength at large ductility via material damping, the amount of necessary carbon fiber may be reduced. Test results of CF/E coupons show rapid decrease in strength after yielding.

Table 5

Fracture energy calculated from coupon-scale fracture tests

Material Specimen No.	CF/ E		C-IEPM	
	1	2	1	2
Maximum load (P_{max} , N)	93.9	117.2	226.34	196.9
Fracture energy (G_f , J)	783.94	1,209.21	1,386.059	1,623.40
Average (P_{max}/G_f)	107.63 N / 1,020.77 J		218.49 N / 1,562.096 J	

In **Fig. 17**, P_{max} in C-IEPM coupons is 250% greater than in CF/E coupons. **Table 5** shows the calculated fracture energies for the four coupons, revealing that at the cusp of crack growth, C-IEPM significantly enhanced resistance to crack propagation by eliciting significantly more fracture energy than CF/ E, where the average fracture energy in C-IEPM was 50% greater than that in CF/E.

Similarity principles, the linear nature of CF/E, and the shear failure modes that

were observed experimentally, in-the-field, and that are consistent with the American Concrete Institute (ACI) 318-08 Standard [45] in both “Pre-Katrina” and “Post-Katrina” test girders indicate that conclusions from this study are applicable (“scalable”) at the field-scale. Although the non-linear nature of energy transferability (energy absorption / dissipation and fracture energy) that is driven by the design of IEPM may at first ostensibly preclude scalability of C-IEPM when limiting the damage state in coastal bridges, e.g., to cracking, the chemical reactivity between (-NCO) moieties and curing epoxy at small t_c , which engender a quality IEPM to enhance material damping in conventional CF/E, is not scale-dependent. Therefore, the findings from this study are applicable to the field-scale.

Conclusions

An experimental testing program was developed to analyze six connection-detail design schemes in coastal bridges, ascertaining their structural integrity and plausibility to reduce each girder’s serviceability limit state to local cracking during major hurricane events. The test-bed for each test girder included a periodic wave-force function, consisting of simultaneous surge (vertical / hydrostatic) and wave (lateral and vertical / hydrodynamic) forces in accordance with the existing I-10 bay-way AASHTO bridges in Mobile, Alabama. The six single-span Test Girders (TG, $1/4$ scale) were designed using the following connection-details: (1) ‘Pre-Katrina,’ or ‘as-is’ mechanical connections prior to the 2005 Hurricane Katrina event; (2) ‘Post-Katrina,’ which utilized through-bolt threaded anchors for the concrete girders; (3) conventional carbon-fiber reinforced epoxy (CF/E)-wrapped connection-details that included pre-Katrina-designed mechanical connections; and (4) – (6) Carbon-fiber Interfacial Epoxy-Polyurea Matrix (C-IEPM) at different t_c (2.5

hr and 1.5 hr) was applied to zero, one, or two girder-ends eliciting different essential boundary conditions, with or without existing pre-Katrina-designed mechanical connections.

IEPM was annexed to curing CF/E via chemical bonding between curing epoxy and polyurea moieties, producing a new interfacial C-IEPM composite (between the epoxy and polyurea components). A calculated Hurricane Katrina wave function was dynamically applied to the six test girders. Pre-Katrina TG, Post-Katrina TG, and C-IEPM_0 TG connection-details failed after approximately one-half of the load cycle duration; within 0.5 sec after the initial shear failure of the connection-details, the girders severed from their respective cap-beams. Although C-IEPM_1 TG exhibited about 2.5 to 3 times greater strength than Pre-Katrina TG, Post-Katrina TG, and C-IEPM_0 TG, C-IEPM_1 TG also failed in less than one full load cycle.

Although the connection-details in C-IEPM_2 TG and CF/E TG were able to achieve the maximum wave load (160.1 kN), CF/E TG was deemed to have effectively failed during cycle No. 1 as it was unable to recover, or re-achieve, the maximum force during the load plateauing stage and after experiencing excessive damage to its connection-details, including fiber breakage. However, because of an aggrandized quantity of fiber and re-orientation of materials axes, the reserve strength and deflection recovery helped the girder to recover a portion of the energy during subsequent loading cycles until catastrophically detaching from its cap-beam supports. Conversely, C-IEPM, formulated on a reaction between epoxy and polyurea moieties to engender a high-quality IEPM, infused significant material damping via damping ratio of 4.87% (versus 1.18% for CF/E) to the connection-details, therefore limiting the damage state of the girder to local cracking

after 12 wave-load cycles. The final conclusions of the study are summarized as follows:

- CF/E TG was unable to dissipate sufficient energy per loading cycle, experiencing significant girder rotation and fiber delamination. As the damage accumulated, the force-deflection hystereses remained transient until the girder catastrophically failed
- C-IEPM_2 TG provided sufficient energy dissipation and fracture toughness (fracture energy), thus localizing damage to the fiber, matrix, and concrete in the connection-details. The anelastic behavior and hyperelastic response of the girder help to stabilize its hystereses after load cycle No. 3 or load cycle No. 4, characterizing its survival. After 12 load cycles, C-IEPM_2 TG experienced only localized damage.

C-IEPM appears to be a viable option for minimizing bridge-damage under extreme coastal hurricane forces. Requiring a minimal quantity of carbon-fiber, C-IEPM minimizes the serviceability limit state of bridge girders to local cracking, thereby drastically extending the life-span of vulnerable coastal bridges.

Acknowledgments

This work was supported by the Alabama Department of Transportation [Grant No. 930-935S]. The research was also partially supported by the Center for Nanophase Materials Sciences (CNMS) at the U.S. Department of Energy's Oak Ridge National Laboratory (ORNL) [Grant Nos. CNMS2018-086, CNMS2017-R80 and CNMS2017-R59].

References

- [1] Office of Coastal Management, National Oceanic and Atmospheric Administration (NOAA); 2018. <https://coast.noaa.gov/states/fast-facts/hurricane-costs.html>
- [2] Padgett J, DesRoches R, Nielson B, Yashinsky M, Kwon OS, Burdette N, Tavera E. Bridge damage and repair costs from Hurricane Katrina. *Journal of Bridge Engineering*. 2008 Jan;13(1):6-14.
- [3] U.S. Department of Transportation, Federal Highway Administration, 2016. <https://trid.trb.org/view/1501848>
- [4] Nowak AS, Grouni HN. Serviceability considerations for guideways and bridges. *Canadian Journal of Civil Engineering*. 1988 Aug 1;15(4):534-8.
- [5] Douglass SL, Chen Q, Olsen JM, Edge BL, Brown D. Wave forces on bridge decks. Coastal Transportation Engineering Research and Education Center Final Report. Univ. of South Alabama, Mobile, Ala. 2006 Apr.
- [6] Chen Q, Wang L, Zhao H. Hydrodynamic investigation of coastal bridge collapse during Hurricane Katrina. *Journal of Hydraulic Engineering*. 2009 Mar;135(3):175-86.
- [7] Ramey, G., Alvin Sawyer III, and Joel G. Melville. Hurricane Surge/Surface Wave Forces on Deck-Girder Bridges and Design/Retrofit Options for These Bridges. 2008.
- [8] Schumacher T, Higgins C, Bradner C, Cox D, Yim SC. Large-scale wave flume experiments on highway bridge superstructures exposed to hurricane wave forces. *Sixth National Seismic Conference on Bridges and Highways*. Multidisciplinary Center for Earthquake Engineering Research South Carolina. Department of Transportation Federal Highway Administration Transportation Research Board (TRB) 2008.
- [9] Bradner C, Schumacher T, Cox D, Higgins C. Experimental setup for a large-scale bridge superstructure model subjected to waves. *Journal of Waterway, Port, Coastal, and Ocean Engineering*. 2010 May 13;137(1):3-11.
- [10] Bradner C, Schumacher T, Cox D, and Higgins C. Large-Scale Laboratory Observations of Wave Forces on a Highway Bridge Superstructure. TREC Final Report. 2011.
- [11] Xiao H, Huang W, Chen Q. Effects of submersion depth on wave uplift force acting on Biloxi Bay Bridge decks during Hurricane Katrina. *Computers & Fluids*. 2010 Sep 1;39(8):1390-400.
- [12] Bozorgnia M, Lee JJ, Raichlen F. Wave structure interaction: Role of entrapped air on wave impact and uplift forces. *Coastal Engineering Proceedings*. 2011 Jan 26;1(32):57.
- [13] Seiffert BR, Ertekin RC, Robertson IN. Wave loads on a coastal bridge deck and the role of entrapped air. *Applied Ocean Research*. 2015 Oct 1;53:91-106.

- [14] Cai Y, Agrawal A, Qu K, Tang HS. Numerical Investigation of Connection Forces of a Coastal Bridge Deck Impacted by Solitary Waves. *Journal of Bridge Engineering*. 2017 Oct 18;23(1):04017108.
- [15] Qu K, Tang HS, Agrawal A, Cai Y, Jiang CB. Numerical investigation of hydrodynamic load on bridge deck under joint action of solitary wave and current. *Applied Ocean Research*. 2018 Jun 30; 75:100-16.
- [16] Lehrman JB, Higgins C, Cox D. Performance of highway bridge girder anchorages under simulated hurricane wave induced loads. *Journal of Bridge Engineering*. 2011 Apr 25;17(2):259-71.
- [17] Robertson, I.N., Yim, S. and Tran, T., 2011. Case study of concrete bridge subjected to hurricane storm surge and wave action. In *Solutions to Coastal Disasters 2011* (pp. 728-739).
- [18] Silberschmidt, V.V. ed., 2016. Dynamic deformation, damage and fracture in composite materials and structures. Woodhead Publishing.
- [19] Anarde KA, Kameshwar S, Irza JN, Nittrouer JA, Lorenzo-Trueba J, Padgett JE, Sebastian A, Bedient PB. Impacts of Hurricane Storm Surge on Infrastructure Vulnerability for an Evolving Coastal Landscape. *Natural Hazards Review*. 2017 Oct 26;19(1):04017020.
- [20] Sen, R., Liby, L. and Mullins, G., 2001. Strengthening steel bridge sections using CFRP laminates. *Composites Part B: Engineering*, 32(4), pp.309-322.
- [21] Garden, H.N. and Hollaway, L.C., 1998. An experimental study of the influence of plate end anchorage of carbon fibre composite plates used to strengthen reinforced concrete beams. *Composite Structures*, 42(2), pp.175-188.
- [22] Siwowski, T., Kulpa, M., Rajchel, M. and Poneta, P., 2018. Design, manufacturing and structural testing of all-composite FRP bridge girder. *Composite Structures*, 206, pp.814-827.
- [23] Hu H, Yu S, Wang M, Ma J, Liu K. Tribological properties of epoxy/polyurea composite. *Polymers for Advanced Technologies*. 2009 Sep;20(9):748-52.
- [24] Zhou, H.; Attard, T. L.; Dhiradhamvit, K.; Wang, Y.; ErDMAn, D. Crashworthiness Characteristics of a Carbon Fiber Reinforced Dual-Phase Epoxy–polyurea Hybrid Matrix Composite. *Composites Part B: Engineering* 2015, 71, 17–27.
- [25] Zhou, H.; Dhiradhamvit, K.; Attard, T. L. Tornado-Borne Debris Impact Performance of an Innovative Storm Safe Room System Protected by a Carbon Fiber Reinforced Hybrid Polymeric-Matrix Composite. *Engineering Structures* 2014, 59, 308–319.
- [26] Zhou H, Attard TL. Rehabilitation and strength sustainability of fatigue damaged concrete–encased steel flexural members using a newly developed polymeric carbon–fiber

composite. *Composites Part B: Engineering*. 2013 Feb 1;45(1):1091-103.

[27] Zhou H, Attard TL, Wang Y, Wang JA, Ren F. Rehabilitation of notch damaged steel beams using a carbon fiber reinforced hybrid polymeric-matrix composite. *Composite Structures*. 2013 Dec 1;106:690-702.

[28] <https://www.master-builders-solutions.basf.us/en-us/products/concrete-repair-and-structural-reinforcement/carbon-fiber-wraps/masterbrace-sat-4500>

[29] Ramin MA, Le Bourdon G, Heuzé K, Degueil M, Buffeteau T, Bennetau B, Vellutini L. Epoxy-terminated self-assembled monolayers containing internal urea or amide groups. *Langmuir*. 2015 Feb 24;31(9):2783-9.

[30] L. He and T. L. Attard, Viscoelasticity of Chemically Bonded Interfacial Epoxy-Polyurea Matrix per Migration of Epoxy Species via Curing Time Parameter, *Key Engineering Materials*, Vol. 779, pp. 71-79, 2018

[31] ALDOT report 930-687, 2008. <http://www.eng.auburn.edu/files/centers/hrc/930-687.pdf>

[32] Chaallal O, Shahawy M, Hassan M. CFRP repair and strengthening of structurally deficient piles: Design issues and field application. *Journal of Composites for Construction*. 2006 Feb;10(1):26-34.

[33] Dai JB, Kuan HC, Du XS, Dai SC, Ma J. Development of a novel toughener for epoxy resins. *Polymer International*. 2009 Jul;58(7):838-45.

[34] Kuan HC, Dai JB, Ma J. A reactive polymer for toughening epoxy resin. *Journal of applied polymer science*. 2010 Mar 15;115(6):3265-72.

[35] Stearns M, Padgett JE. Impact of 2008 Hurricane Ike on bridge infrastructure in the Houston/Galveston region. *Journal of Performance of Constructed Facilities*. 2011 Feb 11;26(4):441-52.

[36] Guo A, Fang Q, Li H. Analytical solution of hurricane wave forces acting on submerged bridge decks. *Ocean Engineering*. 2015 Nov 1;108:519-28.

[37] Fritz HM, Blount C, Sokoloski R, Singleton J, Fuggle A, McAdoo BG, Moore A, Grass C, Tate B. Hurricane Katrina storm surge reconnaissance. *Journal of Geotechnical and Geoenvironmental Engineering*. 2008 May;134(5):644-56.

[38] Do TQ. Fragility approach for performance-based design in fluid-structure interaction problems, Part I: Wind and wind turbines, Part II: Waves and elevated coastal structures (Doctoral dissertation, Colorado State University. Libraries).

[39] Do TQ, van de Lindt JW, Cox DT. Performance-based design methodology for inundated elevated coastal structures subjected to wave load. *Engineering Structures*. 2016 Jun 15;117:250-62.

- [40] Attard TL, He L, Zhou H. Improving damping property of carbon-fiber reinforced epoxy composite through novel hybrid epoxy-polyurea interfacial reaction. *Composites Part B: Engineering*. 2019 Jan 23.
- [41] González MG, Cabanelas JC, Baselga J. Applications of FTIR on epoxy resins-identification, monitoring the curing process, phase separation and water uptake. *Infrared Spectroscopy-Materials Science, Engineering and Technology*, IntechOpen. 2012.
- [42] Chowdhury RA, Hosur MV, Nuruddin M, Tcherbi-Narteh A, Kumar A, Boddu V, Jeelani S. Self-healing epoxy composites: preparation, characterization and healing performance. *Journal of Materials Research and Technology*. 2015 Jan 1;4(1):33-43.
- [43] El Maaddawy T, Sherif S. FRP composites for shear strengthening of reinforced concrete deep beams with openings. *Composite Structures*. 2009 Jun 1;89(1):60-9..
- [44] ASTM Committee E08 on Fatigue and Fracture. Standard test method for measurement of fracture toughness. ASTM International; 2011.
- [45] ACI Committee, and International Organization for Standardization. Building code requirements for structural concrete (ACI 318-08) and commentary. *American Concrete Institute*, 2008.

VISCOELASTICITY OF CHEMICALLY BONDED INTERFACIAL EPOXY-
POLYUREA MATRIX PER MIGRATION OF EPOXY SPECIES VIA CURING TIME
PARAMETER

By

LI HE, THOMAS L. ATTARD

Key Engineering Materials, Volume 779, September 2018, Pages 71-79

Copyright
2018
by
Trans Tech Publications

Used by permission

Format adapted and errata corrected for dissertation

Abstract

A new fiber (x) reinforced Dynamic Covalent epoxy-polyurea Interface (x-DC_{EP}I) shows good mechanical energy transferability of impact and vibration forces. The bonding property of x-DC_{EP}I interface, engendered between curing, or reactive, epoxy and dynamic polyurea, is controlled by epoxy curing time (t_c). The reaction of curing epoxy, where t_c is a thermodynamic processing parameter, and fast-curing/ dynamic aliphatic polyurea, which lacks polyol in its resin chain extender, is linked to bulk mechanical energy transfer, quantified specifically via the loss modulus of x-DC_{EP}I. The parameter t_c effectuates designable chemical bond properties within x-DC_{EP}I. Using Generalized Maxwell models, viscoelastic properties of epoxy, polyurea, and x-DC_{EP}I are predicted, and results are verified using Dynamic Mechanical Analysis (DMA). The Maxwell models for x-DC_{EP}I, as a function of t_c , are used in a finite element analysis (ABAQUS) to control performance of dynamically loaded structures.

Keywords: Polyurea, Epoxy, Viscoelasticity, DMA, Complex Moduli, Loss Modulus, Generalized Maxwell Model

Introduction

Mechanical energy transferability in composite structural dynamics is a well-accepted design parameter that has been richly investigated [1, 2]; yet, the topic, which affects a multitude of applications, deserves far greater attention [3-5], inasmuch as the formulation of composite energy transfer via interfacial constituent manipulation of chemically covalent bonds had remained unexplored [6].

Polyurea is an elastomeric, cost-effective, easy-to-apply spray-coating technology that is an attractive damage mitigation option for many civilian and military infrastructures, improving structural survivability in certain low-energy ballistics and blast environments [7]. Tekalur, et al. [8] performed experiments to test blast-resistance of polyurea-coated composite panels, showing that sufficient polyurea layering on the impact side can considerably increase blast resistance and also low-energy ballistics-resistance when combined with other damage-mitigation systems.

Polyurea-focused mitigation traditionally utilizes steel and composite substrates, eliciting an increase in energy transferability as a function of polyurea thickness. Studies [7-9] on blast-mitigation have also found that polyurea-coated composites enhance energy transfer as a function of polyurea thickness. However, because polyurea is only an elastomer, coated panels are unable to sufficiently localize energy from large-charge energy releases, thus detrimentally transferring energy to panel supports.

Energy transferability in conventional fiber-reinforced polymers (FRP) is usually controlled by fiber orientation, matrix hysteresis, and fiber-matrix interface hysteresis. Most thermosetting polymers, such as epoxies, fracture at relatively low strains. Damage in the epoxy or fiber-matrix interface quickly bridges to induce macroscopic material

failure. To enhance damage tolerance, *damage barriers* are effectuated in a new fiber (x) reinforced Dynamic Covalent epoxy-polyurea Interface (x-DC_{EP}I) in order to isolate micro-scale damage events and render individual cracks harmless [3,4].

To localize damage in x-DC_{EP}I (FRP), such as fiber-matrix debonding and fiber-breakage, a newly uncovered Dynamic Covalent epoxy/polyurea Interface (DCI) intermittently adjoins FRP and polyurea to stabilize crack growth by transferring imparted energy via educed molecular vibrations, resulting in local energy management and thus ingenerating substantial resiliency and composite strength sustainability.

Microstructurally, Attard, et al. [3] found that tunable and sustainable (via large cohesion strength) viscoelastic properties can be instituted in FRP by topically applying a lightly crosslinked elastomer (polyurea) to a three-dimensional highly cross-linked epoxy (thermoset) morphology during the latter's intermediate curing cycle.

x-DC_{EP}I Composite

x-DC_{EP}I is a new mechanical transfer-energy system designed and manufactured using a dual-hybridized dynamic covalent interface (DCI), which contains amino-based polymeric compounds that bridge elastomeric polyurea properties to stiff epoxy properties and also institute significant viscous damping. Zhou et al. [10] used C-DC_{EP}I (x = Carbon-fibrous composite) to retrofit fatigue-damaged concrete-encased steel flexural members, revealing significantly more energy transferability than conventional C-FRP. Attard et al. [11] and Zhou et al. [3] the latter in low/ medium-velocity crush-testing, showed that mechanical energy transfer in C-DC_{EP}I improves dramatically when DCI is manufactured at lower t_c and thicker polyurea (h_p). However, t_c and polyurea reactivity/ dynamicity

dominate energy transferability in high-strain-rate-inducing load environments, evoking controllable viscoelastic properties and damage localization¹². In this study, viscoelastic properties of x-DC_{EPI}, predicated on DCI, are modeled using a Generalized Maxwell model and verified using DMA.

DMA Configuration

Spraying polyurea (in its dynamic reactive form) to the surface of curing epoxy (t_c) engenders a covalently bonded DCI that controls cohesion strength and induces unique molecular vibration properties that can link to macro-properties in C-DC_{EPI} [6] In this study, C-DC_{EPI} specimens were designed for six DCI, $t_c = \langle 0, 0.5, 1.0, 2.0, 3.5 \rangle$, and for $t_c = 24$ (polyurea is sprayed to fully cured epoxy surface, engendering no DCI), see **Table 1**. Chemical analysis via atomic force microscopy (AFM) educes DCI thickness about 2 μm (at higher t_c) and 50 μm ($t_c=0$).

Table 1

DMA Test Specimen Details

Curing time (t_c , hr)	Total Specimen Thickness (h_t , mm)	Polyurea Thickness, mm	Epoxy Thickness, mm	Width (mm)
0	1.55	1.31	0.24	7.27
0.5	2.38	1.58	0.80	6.87
1.0	2.64	1.64	1.00	7.97
2.0	2.93	2.12	0.81	6.28
3.5	4.41	3.12	1.29	9.05
24	4.48	1.30	3.18	7.93

TA Instruments Q800 Dynamic Mechanical Analyzer (DMA) was used to collect and analyze data in single-mode cantilever bending. Complex dynamic Young's modulus is defined as $E^* = E' + iE''$, where E' is storage modulus (time-dependent linear elastic

component), and E'' is loss modulus (material damping). The ratio of loss/ storage moduli in the form $\tan \delta = E''/E'$ represents total energy transfer, i.e., the capability to absorb and transfer mechanical energy per loading cycle as a function of elasticity, load-rate, and material damping.

Generalized Maxwell Models and its Parameters

Generalized Maxwell Model

The Generalized Maxwell model, **Fig. 1**, is phenomenologically comprised of a linear spring (E_e) and several parallel models [$M = M(E_i, \eta_i)$] that describe complex material relaxation [6, 12].

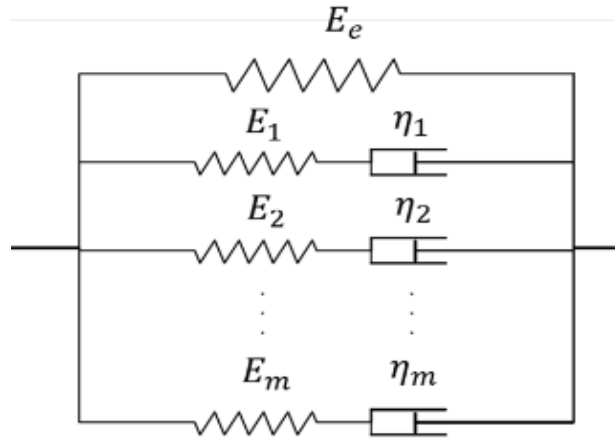


Fig. 1. Generalized Maxwell Model

Constitutive equations of spring and multi-models [M] are

$$\sigma_e = E_e \varepsilon \quad (1)$$

$$\frac{d\varepsilon}{dt} = \frac{d\sigma_i}{dt} \frac{1}{E_i} + \frac{\sigma_i}{\eta_i} \quad (2)$$

$$\sigma = \sigma_e + \sum_i^m \sigma_i \quad (3)$$

where $\sigma^*(\omega)$ is the complex stress function in the Generalized Maxwell Model that contains the elastic spring stress σ_e . The imaginary component, $\sigma_i(\omega)$, is derived via Fourier transform of Equation (2) to account for rate-dependent loading. The complex modulus $E^*(\omega)$ may then be derived as a Prony Series, Equation (4), which contains storage and loss moduli, where the former contains real and imaginary components.

$$E^*(\omega) = E_e + \sum_{i=1}^m E_i \frac{i\omega\rho_i}{1 + i\omega\rho_i} \quad (4)$$

The elastic modulus, E_e , is one component of the storage modulus $E'(\omega)$, Equation (5) [13], which also contains a real component in the frequency domain. The imaginary component of Equation (4), or $E''(\omega)$ in Equation (6), is the loss modulus. Equations (5) and (6) are derived for the Generalized Maxwell Model, which is later applied to Equation (9) to quantify DCI in terms of loss modulus and t_c .

$$E'(\omega) = E_e + \sum_{i=1}^m E_i \frac{\omega^2\rho_i^2}{1 + \omega^2\rho_i^2} \quad (5)$$

$$E''(\omega) = \sum_{i=1}^m E_i \frac{i\omega\rho_i}{1 + \omega^2\rho_i^2} \quad (6)$$

In Equations (5) and (6), ω is angular frequency, and ρ_i is relaxation time. The Generalized Maxwell Model may be expressed by a relaxation modulus equation to ascertain relaxation behavior in viscoelastic materials. The relaxation modulus may be derived in the time domain via Equations (1) – (3), and the storage modulus may be expressed as Prony Series, Equation (7)

$$E'(t) = E_e + \sum_{i=1}^m E_i e^{-\left(\frac{t}{\rho_i}\right)} \quad (7)$$

Material Model Parameters

For the Generalized Maxwell Model of Equation (4) – (7), E_e , E_i and ρ_i are Pony Series parameters, calibrated for Equation (4), to storage moduli data via DMA testing of pure epoxy and pure polyurea. By isolating the epoxy and polyurea components in C-DC_{EP}I specimens, the contribution of DCI in terms of moduli and damping may be calculated. The storage modulus $E'(\omega)$ for polyurea and epoxy was obtained via DMA for a series of frequencies $\omega = \langle 500, 50, 5, 0.5, 0.1 \rangle$; the results are shown in **Table 2**.

Table 2

Prony Series Fitting Target (DMA Measured Data)

ω (rad/s)	500	50	5	0.5	0.1
f (Hz)	79.577	7.9578	0.79577	0.079577	0.015915
Polyurea E' (MPa)	308.723	299.432	272.23	242.319	222.382
Epoxy E' (MPa)	2273.54	1778.55	1751.22	1731.03	1694.43

The five DMA characteristic data points appear sufficient for fitting the storage modulus relationship to 99% ($R^2=0.99$) correlation. Parameters E_i and ρ_i are obtained by fitting the Prony Series model to DMA test data for pure material. The results of the calibration are shown in **Fig. 2**, where **Table 3** summarizes the parameter results. At ambient temperature (20°C), polyurea viscoelastic behavior may be modeled using Generalized Maxwell function in Equation (7) in accordance with the Prony Series parameters in **Table 3**.

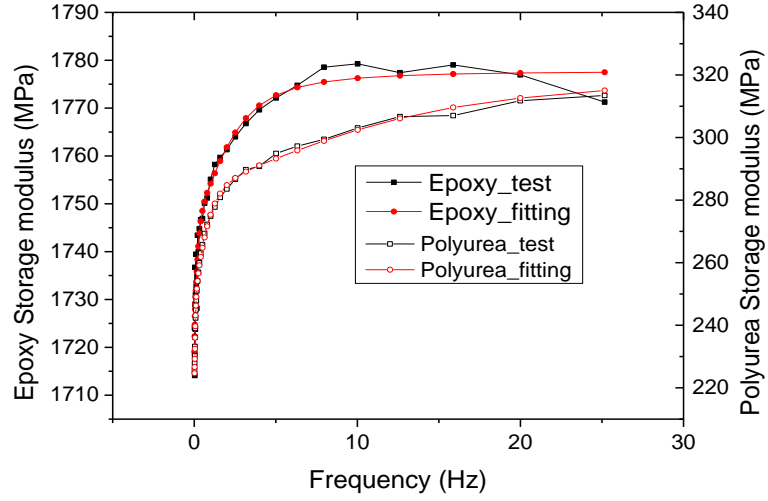


Fig.2. The calibration of the fitting results

Table 3

Prony Series Parameters

	e	1	2	3	4
$E_i(\text{MPa})$	220.392	13.65	6.940	29.13	39.94
$\rho_i(\text{s})$		0.1682	1.311	1.358	20.94
$E_i(\text{MPa})$	1685.54	68.42	379.96	256.42	179.30
$\rho_i(\text{s})$		30.79	0.0454	0.02161	0.01767

Knowing epoxy Poisson's ratio (ν) of 0.4 and polyurea 0.45, the viscoelastic property may then be expressed as the shear relaxation [14] modulus $G(t)$ and bulk relaxation modulus, $K(t)$, which are obtained using Equations (8a) and (8b).

$$G(t) = \frac{E(t)}{2(1 + \mu)} \quad (8a)$$

$$K(t) = \frac{E(t)}{3(1 - \mu)} \quad (8b)$$

Results and Discussion

DMA Results and Discussion

Because of the uncertainty in DCI thickness and distribution of *type* of covalent bonds within DCI (where different bonds will transfer energy via unique vibration properties), a conservative approach was used to calculate the general contribution of DCI to loss modulus, which describes energy transfer capacity (material damping) via materials deformation and heat to attenuate structural response[15]. Polyurea along with a combination of DCI and epoxy produces a dual-parallel Generalized Maxwell Model [16], **Fig. 3**, for viscoelastic x-DC_{EP}I. Equation (9) models x-DC_{EP}I as polyurea (p), epoxy (e), and DCI (D) using Equation (4).

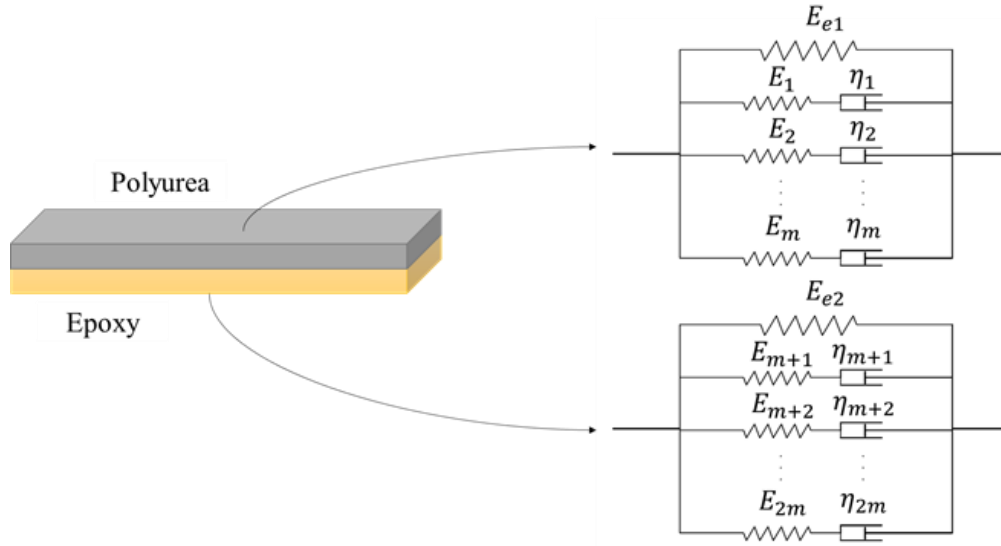


Fig. 3. Epoxy/polyurea Generalized Maxwell Model Components

$$\begin{aligned}
 E^*(\omega) = & \alpha_p E_{e1} + \alpha_e E_{e2} + \alpha_D E_{e3} + \alpha_p \sum_{i=1}^m E_i \frac{i\omega\rho_i}{1 + i\omega\rho_i} + \alpha_e \sum_{i=m+1}^{2m} E_i \frac{i\omega\rho_i}{1 + i\omega\rho_i} \\
 & + \alpha_D \sum_{i=2m+1}^{3m} E_i \frac{i\omega\rho_i}{1 + i\omega\rho_i}
 \end{aligned} \tag{9}$$

where volume-fraction coefficients are $\alpha_p = h_p/h_T$, $\alpha_e = h_e/h_T$, $\alpha_D = h_D/h_T$, and the total specimen thickness is $h_T = (h_e + h_p + h_D)$, see **Table 1**. Using Equation (9) and DMA test results, including storage and loss moduli and $\tan(\delta)$ of pure polyurea and epoxy, see **Fig. 4**, the contribution of DCI = DCI (t_c) to the complex modulus may be calculated. To validate the DMA data, polyurea, which is an elastomer, has an expectedly similar loss modulus (17 ~ 20 MPa) as pure epoxy, see **Fig. 4(a)** and **(b)**; storage moduli are expectedly different (one order of magnitude

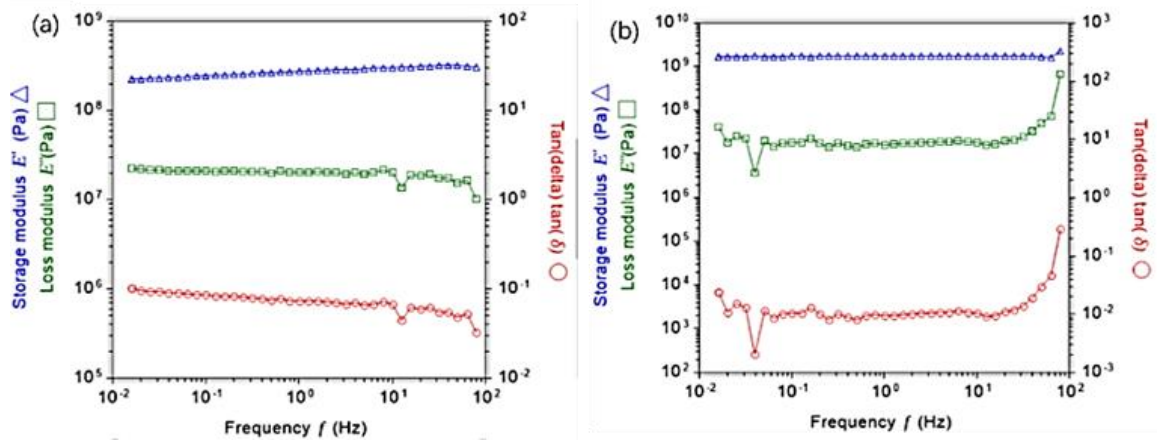


Fig. 4. DMA results of (a) polyurea and (b) epoxy at 20°C

In this study, DMA data was normalized relative to polyurea thickness (h_p) for x-DC_{EPI} (t_c). Assuming a two-layer system, see **Fig. 3**, the effectuated DCI loss modulus may be determined via the total DMA-measured loss modulus, $E''(\omega)$, for x-DC_{EPI}, see **Fig. 5(a)**.

$$\begin{aligned}
 \alpha_e \sum_{i=m+1}^{2m} E_i \frac{i\omega\rho_i}{1 + \omega^2\rho_i^2} + \alpha_D \sum_{i=2m+1}^{3m} E_i \frac{i\omega\rho_i}{1 + \omega^2\rho_i^2} \\
 = E''(\omega) - \left[\alpha_p \sum_{i=1}^m E_i \frac{i\omega\rho_i}{1 + \omega^2\rho_i^2} \right]
 \end{aligned} \tag{10}$$

The term in brackets on the right side represents loss modulus of pure polyurea (based on its volume fraction). Because $E''(\omega)_{x-DC_{EPI}} \gg E''(\omega)_e$ (comparison of **Fig. 5(a)** and **4(b)** and $h_e > h_D$, we conservatively assumed:

$$E''(\omega)_{DCI} = \sum_{i=2m+1}^{3m} E_i \frac{i\omega\rho_i}{1 + \omega^2\rho_i^2} \approx \frac{1}{\alpha_e} \left\{ E''(\omega) - \left[\alpha_p \sum_{i=1}^m E_i \frac{i\omega\rho_i}{1 + \omega^2\rho_i^2} \right] \right\} \quad (11)$$

The results are depicted in **Fig. 5(b)**, which shows about 100% increase in loss modulus contribution by DCI ($t_c = 0$) in comparison to DCI ($0.5 < t_c < 2$), with a marked drop-off for DCI ($t_c > 2$). The sudden drop-off at about 10Hz was due to a slip-condition at the boundary support of the cantilevered specimen. The results validate the tremendous influence enacted by epoxy curing time on DCI loss modulus.

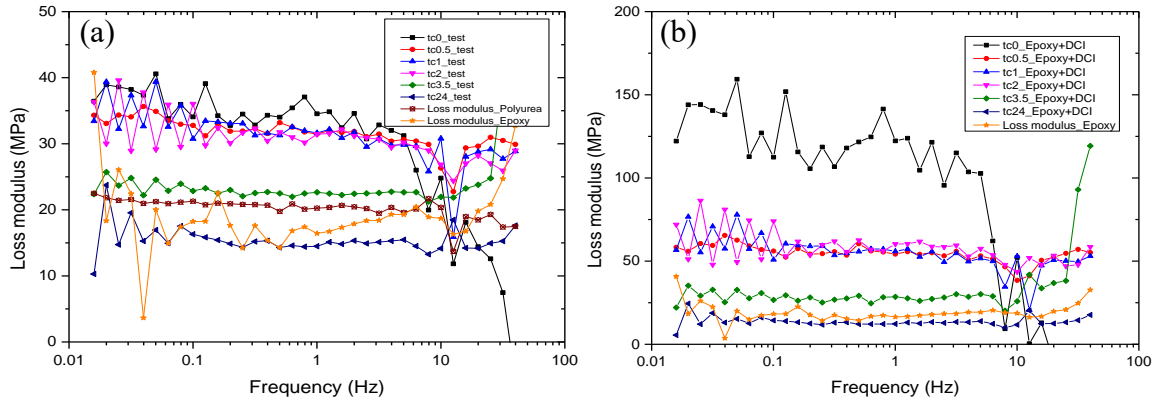


Fig. 5. Loss modulus $E''(\omega)$: (a) $E''(\omega)_{x-DC_{EPI}}$ via DMA tests; and (b) $E''(\omega)_{DCI}$ via DMA tests and assuming **Fig. 3** model

The ratio of loss modulus to storage moduli, i.e., $\tan(\delta)$, intimates energy transferability in materials [15] as a function of material damping (\propto loss modulus), inelastic material behavior (post-yield stiffness degradation), load-rate (w), and elastic stiffness (E_e). An observation of $\tan(\delta)$ in **Fig. 6(a)** and **6(b)** reveals that while $\tan(\delta)$ is

again greatest for DCI ($t_c = 0$), the disparity to other values of t_c is smaller than loss modulus in **Fig. 5(b)**. However, structure loading did not induce material damage, and therefore, there exists a similarity between x-DC_{EP}I and DCI+epoxy in **Fig. 6(a)** and **6(b)** due to the large storage modulus found in pure epoxy which provides the necessary stress transferring paths in x-FRP structures. However, the large loss modulus enacted by DCI helps to transfer energy via its covalent chemistry (bond strength/ enthalpy and molecular vibrations), thus preserving the x-FRP structure and minimizing/ localizing damage, ingenerating substantial resiliency, and composite strength sustainability. Studies by Attard et al. [7] and Zhou et al. [5] reveal on micro- and macro- levels are consistent with these findings, where DCI width (h_I) decreases as t_c increases; and in x-DC_{EP}I specimens with $t_c = 24$ hr (fully cured epoxy), there is no DCI (covalent bonding).

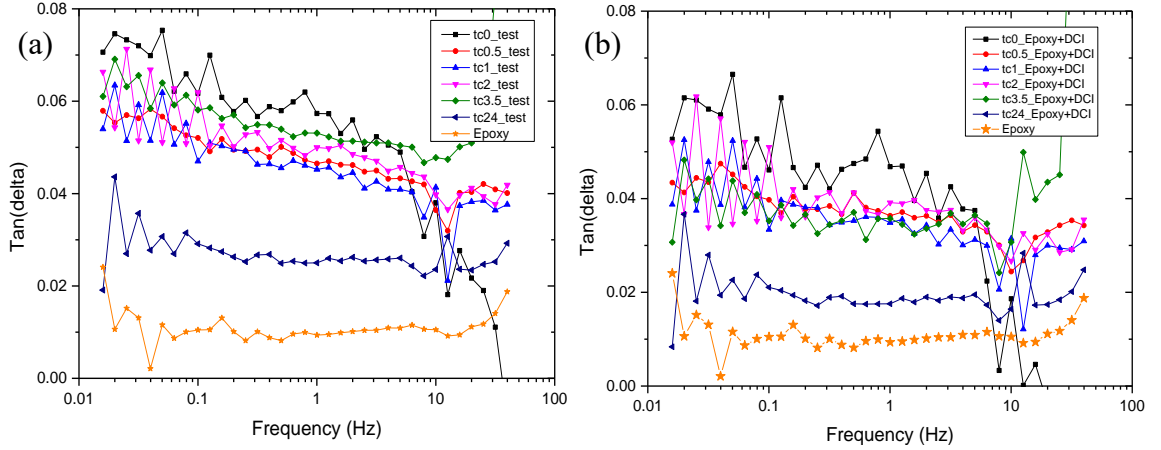


Fig. 6. Tan (δ) results for: (a) x-DC_{EP}I (via DMA); and (b) Epoxy + DCI system

FEA Results and Discussion.

To quantify DCI-induced material damping and bond strength in x-DC_{EP}I specimens, measured via DMA, we performed an independent analysis using the

Generalized Maxwell material model to validate the influence of t_c on viscoelastic behavior. The behavior of DCI at different curing times (t_c) is modeled using a cohesive contact property. We started with an assumption that DCI ($t_c = 0$) represents a fully bonded interface (bond strength). The bonding strengths of x-DC_{EP}I for various DCI ($t_c = 0$, $t_c = 1$, $t_c = 1.5$, $t_c = 3.5$ hours) were computed as 5 MPa, 3 MPa, 1 MPa, and 0.5 MPa, respectively using a Cohesive Element Model(CZM)[17], and the cohesive element modulus were 500 MPa, 400 MPa, 200MPa and 100 MPa.

The FE model and simulations assume polyurea thickness (h_p) of 24 mm and epoxy thickness (h_e) of 16 mm. The model is shown in **Fig. 7(a)**. A 0.1 N input force was applied at the specimen boundaries (fixed-fixed) at a frequency of 10 Hz. The time delay Δt of stress was used to determine the viscoelastic property of each specimen using Equation (12) [15, 18].

$$\tan(\delta) = \frac{\Delta t}{T} \quad (12)$$

where Δt is the delayed time and T_f is the period of the force in **Fig. 6 (b)**.

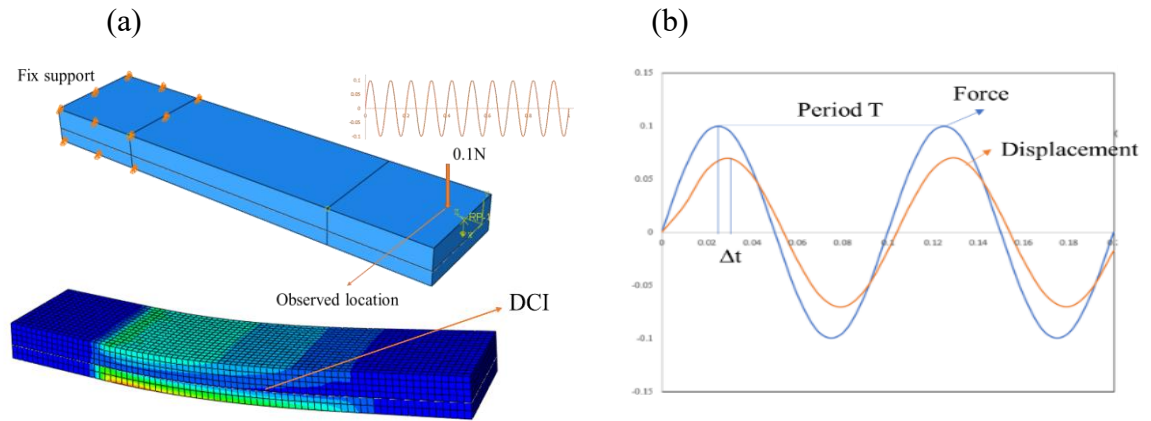


Fig. 7. (a) FE Model of a cantilever beam in single-mode bending, (b) Difference between the response of displacement and force

The force-displacement behavior at the loading point (**Fig. 7(a)**) is observed, and the four contact properties are simulated with respect to the four values of t_c . The response of each specimen is shown in **Fig. 8**. The elliptical hysteresis represents varying levels of damping [19]. In **Fig. 8**, elliptical area (\propto energy dissipation $\rightarrow \tan(\delta)$) increases and ellipse rotation decreases (towards 45°) as t_c decreases, which is consistent with DMA findings in support of DCI (t_c) influence.

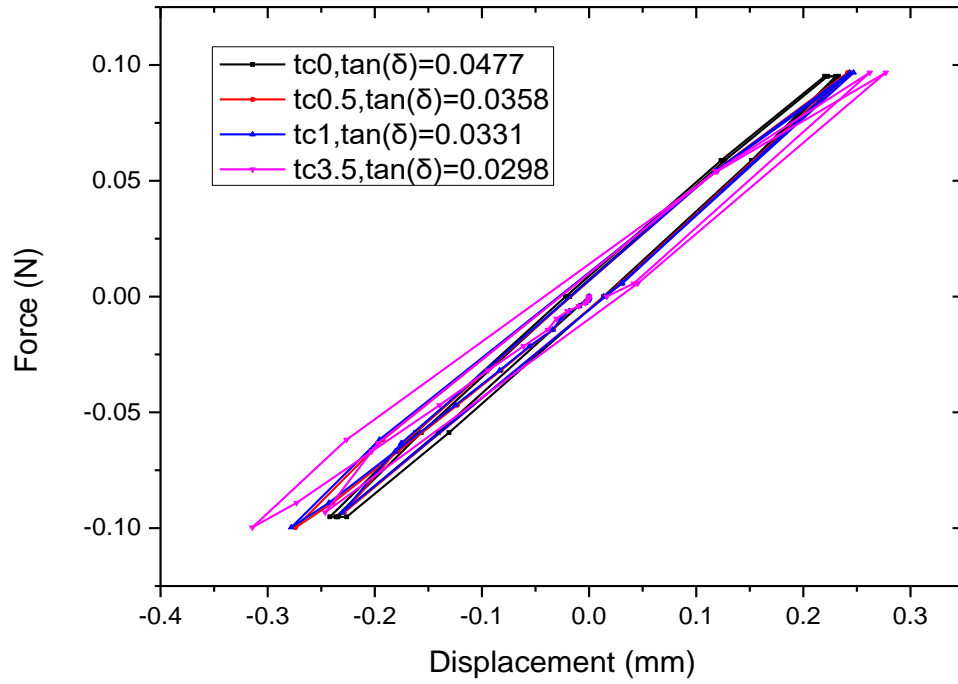


Fig. 8. Harmonic Response of the specimen

Conclusions

A new fiber (**x**) reinforced **D**ynamic **C**ovalent epoxy-polyurea **I**nterface (x-DC_{EPI}) shows good potential to greatly enhance mechanical energy transfer, including impact, fatigue, and vibration, in composite structures due to a viscoelastic property engendered via new intermittent **D**ynamic **C**ovalent epoxy-polyurea **I**nterface (DCI). The following four conclusions are relevant to DCI viscoelasticity.

A Generalized Maxwell Model is constructed using DMA experimental data, which accurately expresses the epoxy, polyurea and DCI properties.

A parallel epoxy/ DCI and polyurea system conservatively computes the DCI's progenerated viscoelasticity.

Epoxy curing time (t_c) has a large influence on the loss modulus contribution by DCI which enhances energy transferability in x-DC_{EPI} composite. Lower values of t_c institute enhanced material damping and bond strength between epoxy (which provides stress-transferring paths for FRP) and polyurea.

Finite element analysis, incorporating a Generalized Maxwell model, accurately simulates the polyurea, epoxy, and DCI properties, see Equation (11), that comprise x-DC_{EPI}. The results are confirmed via DMA testing, see **Figure 5**. The analysis, in accordance with DMA results, validates the influence of DCI on energy transferability and loss modulus (material damping).

References

- [1] Chen, C.C. and Linzell, D.G. (2014). "Numerical Simulations of Dynamic Behavior of Polyurea Toughened Steel Plates under Impact Loading," *Journal of Computational Engineering*
- [2] Huang, W., Yang, Y., Li, H., Lyu, P., & Zhang, R. (2017). Characterization and Damping Property of a Modified Polyurea Material. *DEStech Transactions on Materials Science and Engineering*, (ictim)
- [3] Zhou, H., Attard, T.L., Dhiradhamvit, K., Wang, Y., and Erdman, D. (2015). "Crashworthiness characteristics of a carbon fiber reinforced dual-phase epoxy-polyurea hybrid matrix composite," *Composites Part B: Engineering*, 2015. **71**: p. 17-27.
- [4] Zhou, H., Dhiradhamvit, K.. and Attard, T.L. (2014). "Tornado-borne debris impact performance of an innovative storm safe room system protected by a carbon fiber reinforced hybrid polymeric-matrix composite," *Engineering Structures*, **59**: p. 308-319.
- [5] Jia, Z., et al., (2016). "Experimentally-based relaxation modulus of polyurea and its composites," *Mechanics of Time-Dependent Materials*, **20**(2): p. 155-174.
- [6] Attard, T.L., Li He (2018). "Linking Nanoscale Changes in Polymer Composites to Bulk Material Properties for Ballistics-Resistant Panels, Accepted for Publication, *ACS Nano*, 2018.
- [7] Hui, T. and Oskay, C. (2012). Computational modeling of polyurea-coated composites subjected to blast loads, *Journal of Composite Materials*. **46**(18): p. 2167-2178.
- [8] Tekalur, S.A., A. Shukla, and K. Shivakumar, Blast resistance of polyurea based layered composite materials. *Composite Structures*, 2008. **84**(3): p. 271-281.
- [9] LeBlanc, J. and A. Shukla, The Effects of Polyurea Coatings on the Underwater Explosive Response of Composite Plates, in Blast Mitigation Strategies in Marine Composite and Sandwich Structures. 2018, *Springer*. p. 53-72.
- [10] Zhou, H., et al., Rehabilitation of notch damaged steel beams using a carbon fiber reinforced hybrid polymeric-matrix composite. *Composite Structures*, 2013. **106**: p. 690-702.
- [11] Attard, T.L. and Shi, Z. (2017). "Molecular Resiliency and Characterization of Designable Interfacial Polymerizations within a Carbon-Fiber Reinforced Polyurea-Epoxy Composite," Under Review, *Journal of Non-Crystalline Solids*, (2017)
- [12] Jia, Z., et al., Determining the shear relaxation modulus and constitutive models for polyurea and polyurea-based composite materials from dynamic mechanical testing

- data, *Mechanics of Composite and Multi-functional Materials, Volume 7*. 2016, Springer. p. 363-367.
- [13] Zienkiewicz, O., M. Watson, and I. King, A numerical method of visco-elastic stress analysis. *International Journal of Mechanical Sciences*, 1968. **10**(10): p. 807-827.
- [14] Ciambella, J., M. Destrade, and R.W. Ogden, On the ABAQUS FEA model of finite viscoelasticity. *Rubber Chemistry and Technology*, 2009. **82**(2): p. 184-193.
- [15] Chang, M., D. Thomas, and L. Sperling, Characterization of the area under loss modulus and $\tan \delta$ -temperature curves: acrylic polymers and their sequential interpenetrating polymer networks. *Journal of applied polymer science*, 1987. **34**(1): p. 409-422.
- [16] Al-Bender, F., V. Lampaert, and J. Swevers, The generalized Maxwell-slip model: a novel model for friction simulation and compensation. *IEEE Transactions on automatic control*, 2005. **50**(11): p. 1883-1887.
- [17] Li, S., et al., Use of a cohesive-zone model to analyze the fracture of a fiber-reinforced polymer-matrix composite. *Composites Science & Technology*, 2005. **65**(3-4): p. 537-549.
- [18] Odegard, G., T. Gates, and H. Herring, Characterization of viscoelastic properties of polymeric materials through nanoindentation. *Experimental Mechanics*, 2005. **45**(2): p. 130-136.
- [19] Graesser, E.J. and C.R. Wong, The relationship of traditional damping measures for materials with high damping capacity: a review, in *M 3 D: Mechanics and Mechanisms of Material Damping*. 1992, ASTM International.

LINKING NANOSCALE CHEMICAL CHANGES TO BULK MATERIAL
PROPERTIES IN IEPM POLYMER COMPOSITES SUBJECT TO IMPACT
DYNAMICS

By

THOMAS L. ATTARD, LI HE

ACS Appl. Mater. Interfaces, 2019 11 22 20404-20416

Copyright
2019
by
American Chemical Society

Used by permission

Format adapted and errata corrected for dissertation

Abstract

A synthesizable Interfacial Epoxy-Polyurea hybridized-Matrix (*IEPM*), comprised of chemical bonded nanostructures across an interface width ranging between 2 μm to 50 μm , is a candidate for dialing-in molecular vibrational properties and providing high-impact dynamics resistance to conventional Fiber(*x*)-Reinforced Epoxy (*F/E*), engendering an *x*-hybrid-polymeric matrix composite system (*x-IEPM-t_c*). Atomic Force Microscopy (AFM) and Scanning Electron Microscopy (SEM) elucidate interfacial nanoscale morphology and chemical structure via reaction kinetics of curing epoxy (as a function of time, *t_c*) and fast-reacting (pre-polymerized) polyurea. Nano-Infrared Spectroscopy (*nano-IR*) spectra, per non-negative matrix factorization (NMF) analysis, reveal that simultaneous presence of characteristic epoxy and polyurea vibrational modes, within a nanoscale region, along with unique *IEPM* characteristics and properties following thermomechanical analysis (TMA) and dynamic mechanical analysis (DMA), indicates chemical bonding, enabling *IEPM* reaction kinetics, as a function of *t_c*, to control natural bond vibrations and type / distribution of interfacial chemical bonds and physical mixtures, likely due to the bond mechanism between –NCO in polyurea, and epoxide and –NH₂ in epoxy hardener (corresponding to characteristic absorption peaks in *nano-IR* results), leading to enhanced *IEPM* quality (fewer defects/ voids). Test results of ballistics-resistant panels, integrated with thin intermediate layers of *x-IEPM-b-t_c*, confirm that lower *t_c* significantly enhances loss modulus (\propto material damping and per DMA) in impact dynamics environments.

Keywords: nanostructure, tunable interface, *nano-IR*, chemical bonding, epoxy, polyurea

INTRODUCTION

Design flexibility, including high-strength and stiffness, good chemical and heat resistance, and low-weight makes Fiber-Reinforced Epoxy (*F/E*) an attractive materials design-option¹ for a multitude of structural components. The U.S. Department of Energy projects the global market for Carbon-F/E (*CF/E*) to grow to \$25.2 billion by 2020 (15.3% growth rate) with a global-value demand of 210,000 metric tons.^{2,3} However, paucity of Mechanical Energy Transfer (*ME.T*) due to brittleness⁴ and to low fracture toughness and material damping, leading to sudden debonding,⁵⁻¹⁷ are often over-compensated by aggrandizing fiber quantity, thus amplifying cost and jeopardizing projected global and economic expectations.

By “enhance *ME.T*,” we refer to a material’s ability to reduce damage or elastic deformation due to physical force. Ballistics-resistance in conventional *CF/E* panels, subject to full projectile-perforation,¹⁸ is limited by low *ME.T*. Various remediation efforts, including supplementing panels with Kevlar-29 and reducing aerial density,^{18,19} provide limited and inconsistent results.²⁰ *ME.T* is a lofty design parameter²¹⁻³³ that has led to the development of various augmenting methods in polymers and *FRPs*, often resulting in adverse aftereffects,^{4-7,34-35} such as decreased mechanical strength, low chemical bond energy, and high production costs: [i] Although coupling agents can facilitate chemical bonding between reinforcing nanoparticle surfaces, dispersed homogenously, and the toughened polymer matrix,^{5-10, 36} where barriers “pin” cracks and impede crack propagation, process complexity and high cost limit the volume fraction of treated nanoparticles to 1% or 2%, thus minimizing benefit to bulk properties; [ii] Although nano-sized rubber particles with significantly higher surface-to-volume ratio (*SV*) than

microstructure or bulk materials create cavitation, crack tip blunting, and crack deflection at the interface to deter crack propagation in the matrix^{37,38} and contribute to better interface-related properties, high SV elicits multifold complications, such as nanoparticle agglomeration, that induce defects on the ‘polymer matrix-filler’ boundary; [iii] Although filling the polymer matrix with liquid rubber to create rubber-particle reinforcements³⁹ has been shown to improve fracture toughness from $0.5\text{MPa}\cdot\text{m}^{1/2}$ to $1.4\text{MPa}\cdot\text{m}^{1/2}$, the addition of rubber reduces the modulus and introduces defects at the “rigid-polymer-matrix/ rubber” boundary due to low bond enthalpy and surface energy in immiscible admixtures; [iv] Although tuning the composition of polymer matrix using a synthesis of block copolymer, e.g.,¹¹⁻¹⁵ PEO-based copolymers at low concentrations,¹³ has been shown to toughen the epoxy matrix, copolymer synthesis is complex and expensive, and experimental conditions are harsh, prohibiting efficaciousness to *FRP* application.

In addition to augmenting methods, several studies have focused on multi-scale material modeling and experimentation, linking nano/micro-scale and macro-scale properties. Jaffel et al.⁴⁰ developed a multi-scale experimental approach to continuously relate microstructure to macroscopic mechanical properties of plaster pastes during their setting, finding that an increase in Young’s modulus was a function of the degree of hydration. Boek et al.⁴¹ studied the colloidal Aggregate Interactions and flow parameters by simulating Asphaltene Interactions in molecular scale, finding that lubrication layers between the nanoaggregates led to the significant screening of direct asphaltene-asphaltene interactions. Also, a two-scale continuum sensitivity formulation was developed and used to ascertain sensitivity parameters of microstructure in the control of texture-dependent properties in deformation processing such as higher strength.⁴² The results indicate that

while multi-scale linkages have uncovered control of macro-scale mechanical properties via microstructure evolution,⁴⁰⁻⁴² no evidence of nanoscale changes appears to link new material properties to high-impact / shock dynamics. In this light, Leventis et al.⁴³⁻⁴⁵ improved mechanical strength of desirable aerogels by creating a cross-linked composite framework using covalent postgelation to anchor, or graft, polymer coatings on nanoscopic skeletal frameworks of silica. Polymer-cross-linking has also been extended to other applications involving aerogels to, e.g., provide stress-resistance against ambient pressure drying,⁴⁶ by grafting isocyanate-derived polyurea to pore surfaces of aerogels with backbone either innate hydroxyl surface functionality of silica⁴⁷ or amine-modified silica, where the latter has been used for cross-linking with polystyrene⁴⁸ and epoxide.⁴⁹ Although pore-surface-coating primary and secondary particles of silica aerogels, i.e., at building-block level, with norbornene functionality via ring-opening metathesis polymerization produced polymer supports⁵⁰ to improve strength fragility (mechanical strength) of aerogels, leading to enhanced macroscopic compression strength,⁵¹ extreme dynamics resistance (impact), for example, ballistics-resistance, remains a challenge.

Moreover, although polymer cross-linking non-related aerogel applications in this context⁴⁵ have been examined, macroscopic strength-enhancing may be limited and cost-ineffective. Instead, we have turned our attention to evincing loss modulus (material properties), in lieu of mechanical strength, by cross-linking isocyanate-derived polyurea without polyol (–OH) component (e.g., aliphatic-based polyurea) with evolving (ongoing) epoxide-amine cross-linking, where we used dynamic mechanical analysis (DMA) and thermomechanical analysis (TMA) to ‘bridge-a-gap’ between probing the cross-linked nanostructure at molecular (IR) and nanoscopic levels (AFM, chemical mapping) using

nano-IR techniques and analyzing impact-dynamics resistance at a macroscopic level (ballistics testing). By using the evolutionary cross-linking of epoxide and amine-based backbone, based on curing time, which is a backbone in itself, porosity (and non-porous) and physical surface mixtures may be minimized, instead of eliciting potentially rich chemical bonding along and through an evolving skeletal contour, evidenced by differing microstructures confirmed by SEM. Our findings, therefore, elucidate interfacial chemistry in apparently new polymer composites, linking nanoscale changes to bulk material properties in highly dynamic broad-scoped environments that may include enhancing ballistics-resistance, making this study a first of its kind.

Combined with high complexity, production limitations, and cost of nanoscale fillers, the design of high-impact absorbent structures is challenging. In our study, we examine nanostructure-based bulk-toughening via interface morphology (in lieu of conventional nanofillers), focusing on a continuous medium between isocyanate-derived polyurea with evolving (curing) cross-linking epoxide-amine functionality as the backbone. The Interfacial Epoxy-Polyurea hybridized-Matrix (*IEPM*), which may be tuned chemically, enhances loss modulus and toughness and minimizes composite brittleness, thus improving $ME.T$ via bonding, within the context of an x-Hybrid-polymeric Matrix Composite / $IEPM-t_c$ ($x-IEPM-t_c$) system,^{5-7,52,53} where “ x ” represents a load-bearing fiber, e.g., carbon ($x = C$), aramid ($x = A$), or glass ($x = G$); if no fiber ($x = \text{none}$) is used, $0-IEPM-t_c$ is designated. On the nanoscale, *IEPM* is a reaction of functional groups of pre-polymerized (aliphatic) polyurea (where the isocyanate monomer, isophorone diisocyanate (IPDI), reacts with polyoxypropylene diamine in lieu of polyol, commonly used in aromatic polyurea that was also investigated) and functional epoxy - in accordance with

the elapsed curing time (t_c) of epoxy – to link interfacial nanostructure and desirable bulk material properties for x - $IEPM$ - t_c , e.g., carbon-fiber-based composites, by eliciting strong chemical bonding across a high-quality interface (up to 50um wide), netting high SV of nanostructures. By tuning chemical reactions of $IEPM$ according to epoxy curing (t_c), where lower curing time elicits higher and more desirable epoxy backbone functionality, and fast-curing aliphatic-based polyurea, critical chemical bonding (density and distribution of chemical reactions) and molecular vibrational properties may be acquired. Previously, we found that $IEPM$ enhances bulk mechanical properties, such as material damping (\propto loss modulus), in x - $IEPM$ - t_c , leading to applications in tornado and hurricane resistance and crashworthiness.^{8-14,32,33} At lower t_c , greater loss modulus was introduced to x - $IEPM$ - t_c -designed structures⁹⁻¹⁰ while maintaining sufficient ambient stiffness. Application of polyurea to cured F/E ($t_c \geq 24$ h)⁵⁴ leads to an epoxy-polyurea physical mixture (without chemical bonding) that introduces only elastic (nonlinear) properties, where $ME.T$ is marginally enhanced.

In this study, we elucidate how lower t_c (and lower-viscosity epoxy-resin, ν) may stimulate different chemical reactions, specifically chemical bonds in lieu of less-desirable physical mixtures, across $IEPM$ that exist between known regions of pure epoxy and polyurea bounded by I_{EP} I_{PU} . By dialing-in t_c , the reaction kinetics of diffusing migrating species of curing epoxy with fast-curing pre-polymerized polyurea may be controlled to synthesize desirable x - $IEPM$ - t_c of high quality (whose $IEPM$ includes minimal defects/pores and densely distributed chemical bonds) to achieve desirable mechanical performance via loss modulus. To understand the ramification on property design ($ME.T$), i.e., the new nanostructures across the $IEPM$, AFM and *nano-IR* were conducted to map

IEPM nanoscale morphology and chemistry, respectively, and to characterize the effects of nanoscale domains and chemical bonding on material properties, such as loss modulus, in *x-IEPM-t_c* samples (using *DMA*). Design of ballistics-resistant panels, serving as a test-bed for impact (shock) dynamics, were controlled via *IEPM*; results confirmed securing of .44 magnum caliber bullets, fired at thin *C-IEPM-b-t_c* panels (where *b*=ballistics). Our discovery reveals that *IEPM* reaction kinetics, dialed-in using lower *t_c* and lower *ν*, may conduce certain nanoscale changes within the infrared (*IR*) frequency range that links *IEPM* quality (related to chemical bond density / distribution and defect / void reduction) and *IEPM* cohesion strength (in terms of bond enthalpy) to bulk *ME.T* properties.

Results and Discussion

Study of Chemical Reactions in the IEPM:

Epoxy (or poly-epoxide) denotes the epoxide functional group as well as cured products of epoxy resin. Epoxy attributes include good mechanical strength and chemical resistance. In this study, epoxy resin polymerizes with amine hardeners to form a cross-linked 3-D network. Its reactant counterpart, polyurea in pre-polymerized, or dynamic, form is an elastomer that is a reaction product of isocyanate (-NCO) based component and amine (-NH₂) based component forming urea linkages to cross-linked networks. In our study, we examined a rigorous number of chemical reactions at the interface by mixing different polyurea and epoxy components at room temperature to observe gelation. Complete results are included in Table S1. After examining various combinations, the reaction between isocyanate and amine epoxy-hardener is the one to most likely occur (Table S-1, Reaction 2) because of its high reaction rate (approximating the fast-reaction

rate of pure polyurea), resulting in a three-part reaction between (epoxide) + (amine epoxy hardener) + (isocyanate) and subsequent formation of a urea bond between epoxy and polyurea. Formation of chemical bonding is in accordance with: (1) *nano-IR* spectra of several *IEPM* consistently featuring both polyurea and epoxy peaks at single nanoscale locations (Figures 1 – 3); (2) consistency of non-negative matrix factorization (NMF) analysis for *IEPM* structures engendered using lower t_c ; (3) size of the laser tip (80 nm) is less than length of either epoxy or polyurea molecule^{55,56}; (4) DMA reveals that loss modulus for *IEPM*- $t_c=24$ h (physical mixture / juxtaposition of epoxy and polyurea) is less than loss modulus for *IEPM*- $t_c < 24$ h (which does not use fully cured epoxy); and (5) TMA reveals unique glass transition temperature (T_g) for *IEPM* structures for $t_c < 24$ h (but not for *IEPM*- $t_c = 24$ h). A suggested reaction is shown in Figure S1.

While polyurea provides limited *ME.T*, a properly designed *IEPM* (as a function of t_c) is characterized by large chemical bond enthalpy (ΔH), or strong bonding. In this light, distribution and density of covalent bonding (primary bonding) between functional groups of topically treated curing epoxy with pre-polymerized polyurea may be designed⁵⁷ to minimize weak secondary bonds / van der Waal forces,⁵⁸ which are associated with higher values of t_c ; DMA results also confirm that loss modulus varies significantly (inversely) with t_c in *x-IEPM*- t_c . In our study, samples were designated as *x-IEPM*- t_c which are listed in Table S2. For example, the C-N bond energy from the urea bond in *0-IEPM*-1.5 ($t_c = 1.5$) is 276 kJ/mol,⁵⁴ which is two orders of magnitude higher than van der Waals force bond energy, or 0.4 - 4.0 kJ/mol,⁵⁴ in *0-IEPM*-24 (where polyurea is sprayed on fully cured epoxy after 24 h). TMA further suggests nanoscale changes to *IEPM*, enacted via epoxy curing kinetics (t_c) and manifesting bonding and “*IEPM* richness,” i.e., density /

distribution of bond enthalpy, physical mixtures, and vibrational modes (molecular vibrational energy), are linked to bulk material property tunability.^{8-12,15,22-24,59}

IEPM Spectra

Figure 1 shows AFM and *nano-IR* results of the *IEPM*- $t_c=0$ reaction (comprising sample 0-*IEPM*-0), where aliphatic polyurea (curing) was applied to curing epoxy at $t_c=0$ h (with no fiber). An optical microscope image, Figure 1(a), indicates that epoxy and polyurea phases are separated by a distinct *IEPM* region of good quality, with minimized pores, gaps or cracks within the boundary. Two consecutive images of a region were scanned by AFM to capture the entire interface which is wider than the maximum AFM scanning range. Figures 1(b) and 1(c) show the changing topography, spanning pure epoxy (bounded by I_{EX}), interface (*IEPM*), and pure polyurea (bounded by I_{PU}). In order to study the chemical composition and bonding characteristics in *IEPM*, 100 *nano-IR* spectra were collected across the interface region. Twelve selected *nano-IR* spectra (marked by red dots) are depicted in Figures 1(b) and 1(c), indicating observable changes in morphology across the *IEPM*. The twelve *nano-IR* spectra at these locations are shown in Figures 1(d) and 1(e). Figure 1(b) displays pure epoxy and *IEPM* that contains both physical mixtures and chemical bonding. Figure 1(c) displays a smooth transition from *IEPM* to pure polyurea. “Wrinkle” patterns are attributed to microtome cutting of the soft polyurea. The bottom-to-top direction in Figure 1(d) corresponds to pure epoxy-to-polyurea in Figures 1(b) and 1(c). Table 1 summarizes our findings, revealing various enthalpies⁵⁴ and vibrational modes which are related to molecular vibrational / potential energy. The bottom spectrum of epoxy region (points 1-3, pastel green) reveals characteristic absorption peaks of pure epoxy

including C-O-C stretching of ethers^{60,61} (1036 cm⁻¹ and 1090 cm⁻¹ absorption peaks). Conversely, the top spectrum of polyurea region (points 9-12, pink) shows characteristic peaks of pure polyurea including the 1090 cm⁻¹ absorption peak (C-O-C) which is also common to *IEPM*. Although points 1-3 and 9-12 also contain higher frequencies (> 1300 cm⁻¹), points 4-8 (orange) are located within the *IEPM* and contain both polyurea and epoxy higher absorption peaks: 1510 cm⁻¹, 1606 cm⁻¹, 1550 cm⁻¹, and 1642 cm⁻¹ absorption peaks; lower frequency peaks (< 1300 cm⁻¹) are typically not strong indicators of specific polymers.

Table 1

Characteristic IR peaks of twelve points in 0-IEPM-0 in Figure 1

Location/ points	Characteristic Peaks in <i>x-IEPM-0</i> (nano-IR results)
1-3 (epoxy)	1036 cm ⁻¹ , 1090 cm ⁻¹ , 1510 cm ⁻¹ , 1606 cm ⁻¹
4-8 (interface)	1036 cm ⁻¹ , 1090 cm ⁻¹ , 1510 cm ⁻¹ , 1550 cm ⁻¹ , 1606 cm ⁻¹ , 1642 cm ⁻¹
9-12 (polyurea)	1090 cm ⁻¹ , 1550 cm ⁻¹ , 1642 cm ⁻¹
Chemical bonds identified according to their peaks	
1510 cm ⁻¹ & 1606 cm ⁻¹ : C-C stretching and C=C stretching of aromatic rings	
1550 cm ⁻¹ : secondary amine with N-H bending and C-N stretching modes	
1642 cm ⁻¹ : represents broad urea carbonyl stretching, covering 4 bands between 1675 cm ⁻¹ and 1590 cm ⁻¹ , ^{60,61}	
1090 cm ⁻¹ & 1036 cm ⁻¹ : C-O-C stretching of ethers; ^{58,59} also contained in polyurea	
Bond enthalpy (kJ/mol)	
C-C: 347; C=C: 620; N-H: 393; C-N: 276; C=O: 745; C-O: 351	

According to Table 1, the 1510 cm^{-1} and 1606 cm^{-1} absorption peaks (both epoxy) refer to C-C and C=C bonds (stretch modes). The absorption peak at 1550 cm^{-1} (polyurea) refers to secondary amine with N-H (bending mode) and C-N (stretching mode). The absorption peak at 1642 cm^{-1} (polyurea) represents a broad urea carbonyl absorption peak covering four bands between 1675 cm^{-1} and 1590 cm^{-1} .^{62,63} Depending on t_c , epoxy-polyurea reactions can ensue various type of *IEPM* quality (in terms of defects / voids), bond, or cohesion, strength (in terms of enthalpy), and *ME.T* (in terms of vibrational modes).

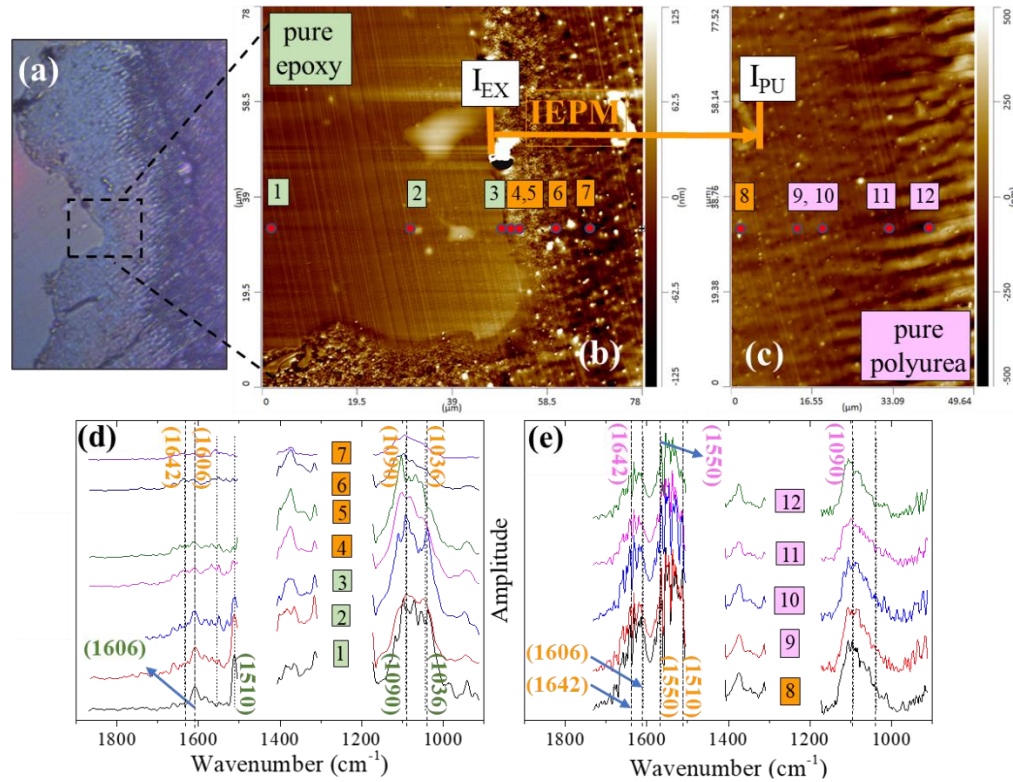


Figure 1. (a) Optical microscopy image of sample 0-*IEPM*-0; (b)-(c) AFM image of *IEPM*-0 topography, spanning a region from pure epoxy (I_{EX}) to pure polyurea (I_{PU}). (d)-(e): IR spectra of 100 points (12 are shown in red), revealing chemical bond characteristics as a function of t_c

Vibrational Modes

To identify a link between *IEPM* chemical bond richness and *nano-IR* spectral changes in Figure 1, t_c (and corresponding *IEPM*) are associated to specific molecular / vibrational modes (and potential energies). The atoms and bond structures comprising each *IEPM* illustrate relative motions of atomic planes as a function of wave behavior and distribution of electron energy (density) in atomic space. To enhance *ME.T* by facilitating [i] chemical bonding between polyurea and epoxy, [ii] better quality *IEPM* (fewer interfacial gaps / defects), and [iii] more *IEPM* layers within x -*IEPM*- t_c , we linked the diffusivity of migrating epoxy agents to vibrational modes (identified using *nano-IR* spectra) using the chemical bonds and physical mixtures identified in each *IEPM*- t_c (TOC). For example, the C=C molecule (1606 cm^{-1} , Table 1) in sample 0-*IEPM*-0 ($t_c=0$) includes a sigma bond ($\Delta H = 350\text{ kJ/mol}$)⁵⁴ and a pi bond ($\Delta H = 270\text{ kJ/mol}$)⁵⁴, and its vibrational modes are C-C stretching and C=C stretching of aromatic rings, N-H bending, C-N stretching, and carbonyl stretching. The strong bonds in aromatic rings, strong polar bonds, and vibrational modes (Table 1) contribute to fracture toughness and loss modulus. However, for x -*IEPM*- $t_c > 1$, the presence of combined 1510 cm^{-1} , 1606 cm^{-1} , 1550 cm^{-1} , and 1642 cm^{-1} absorption peaks is less evident, where impact resistance for larger t_c is less.

9-11

Interfacial Chemical Bonding and Physical Mixing

In order to understand how process tunability (t_c) may affect *IEPM* bond strength and quality, which affect bulk properties, we studied patterns of chemical bonding and physical mixing in 0-*IEPM*- t_c samples as listed in Table S2, sliced to a thickness less than

200 nm. Figures 2(a) - 2(m) show optical microscopy images, AFM topography images and *nano-IR* spectra. Similar to 0-*IEPM*-0 in Figures 1(d) and 1(e), 0-*IEPM*-0.5 and 0-*IEPM*-1.0 in Figures 2(c) and 2(f) reveal a cogent interface region and new features in the *nano-IR* spectra, including simultaneity of polyurea absorption peaks (1550 cm^{-1} , 1642 cm^{-1}) and epoxy absorption peaks (1510 cm^{-1} , 1606 cm^{-1}) on the spectra of points. The *nano-IR* point spectra collected across the *IEPM* (starting from the epoxy-*IEPM* (I_{EX}) boundary) evolve with the gradual decrease in amplitude of the epoxy characteristic absorption peaks (1036 cm^{-1} , 1510 cm^{-1} , 1606 cm^{-1}) and gradual increase in the amplitude of the polyurea characteristic absorption peaks (1550 cm^{-1} , 1642 cm^{-1}). This phenomenon suggests that both physical mixtures and chemical bonds are generated within *IEPM*-1.0 (width of $10\text{ }\mu\text{m}$) and *IEPM*-0 (width of $50\text{ }\mu\text{m}$) as a function of t_c , suggesting different richness in chemical structure produced from lower versus higher t_c . Sample 0-*IEPM*-2.5 displays the following features, see Figure 2(h): 1. Clear boundary between epoxy and polyurea; and 2. Significant gaps on the boundary. While these characteristics do not imply absence of chemical bonding / reactivity in *IEPM*-2.5, quality and width are ostensibly lower, resulting in decreased loss modulus, verified via DMA, and for larger t_c , reduction in interface chemical reactivity, verified via TMA. Finally, Figure 2(j) depicts an optical microscopy image of 0-*IEPM*-24 that completely separated during the microtome cutting process, a result of the weak interface at higher t_c .

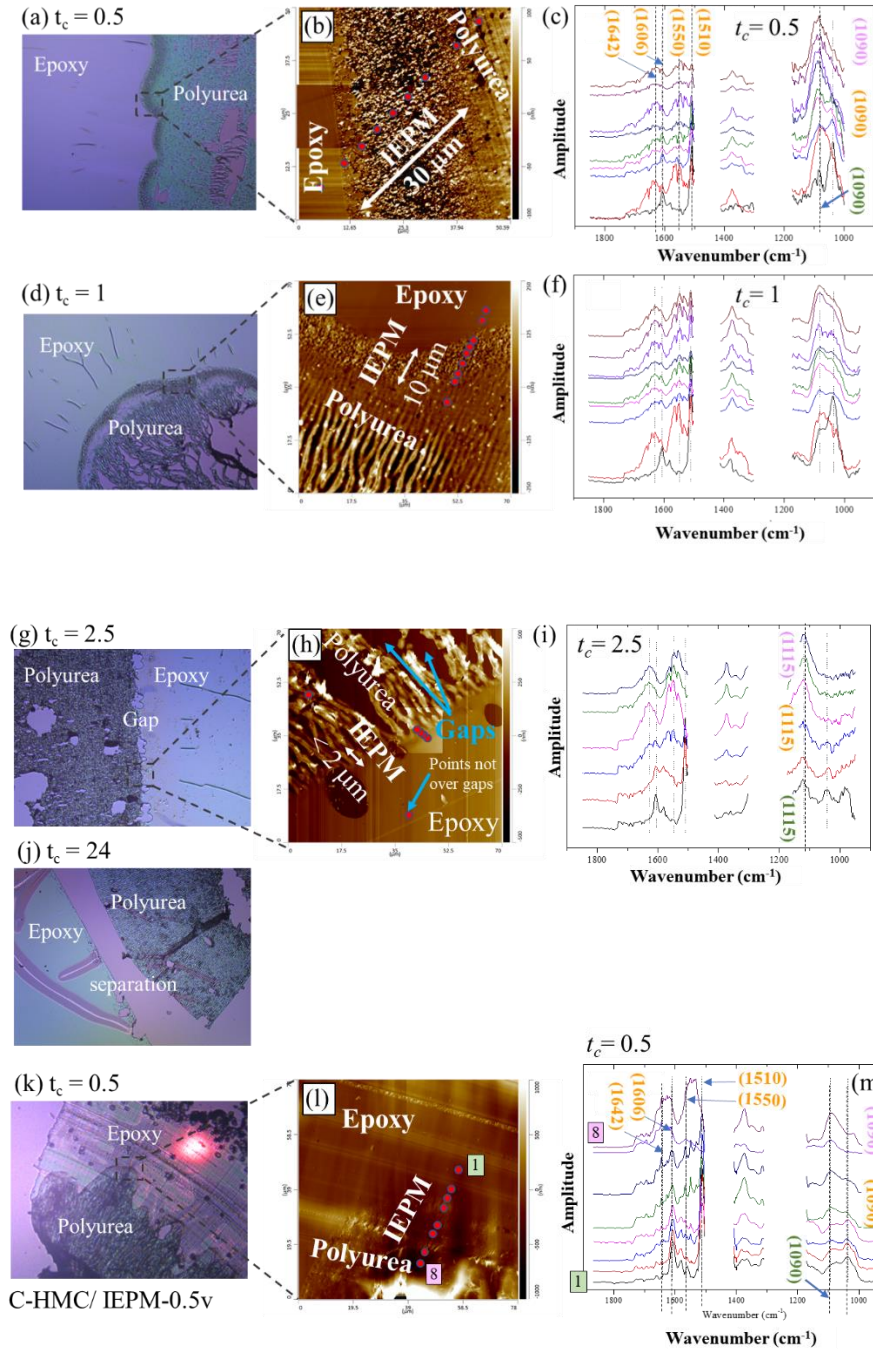


Figure 2. Optical images, AFM topography, and *nano-IR* spectra (corresponding to the red points shown in each interfacial region) of: (a) – (j) : 0-IEPM- t_c for $t_c = 0.5, 1, 2.5$, and 24; and (k) - (m): C-IEPM-0.5v

Interface morphology and chemical bonding were also examined according to epoxy viscosity using sample C-*IEPM*-0.5 ν , which is comprised of a higher-viscosity epoxy (1,367 cps). Although Figure 2(l) does not indicate a clear interface, Figure 2(m) reveals two spectra with all four major absorption peaks (1510 cm⁻¹, 1550 cm⁻¹, 1606 cm⁻¹, and 1642 cm⁻¹) of polyurea and epoxy, indicating the presence of chemical bonding. The decrease in interface clarity and width, in comparison to 0-*IEPM*-0.5, is attributed to slower diffusivity in higher-viscous epoxy relative to lower-viscous epoxy, with diffusivity that fosters a larger functional region for chemical bonding.

Topography Quality and IR Spectra reveal Simultaneity of Epoxy and Polyurea and t_c - driven Chemical Bonding

Table S1 lists possible interfacial chemical reactions. Among five experiments conducted between one epoxy component and one polyurea component, the reaction rate between isocyanate and amine epoxy hardener was remarkably high (comparatively), with the mixture reacting and gelling within 10 seconds at room temperature; the reaction rate is also similar to –NCO and –NH₂ (polyurea hardener). Although this alone only provides a possibility of chemical bond formation between epoxy and polyurea, we next consider that spatial resolution of *nano-IR* laser is approximately 80 nm (although this can vary depending on the material being measured). No new major absorption peaks are discovered on either pure epoxy or pure polyurea *nano-IR* point spectra. However, characteristic wavenumbers 1510 cm⁻¹, 1550 cm⁻¹, 1606 cm⁻¹, and 1642 cm⁻¹ of both epoxy and polyurea molecules (where each is ≥ 100 nm length-scale)⁶⁴ are consistently present in essentially each *nano-IR* point spectra in 0-*IEPM*-0 and 0-*IEPM*-0.5, where the urea carbonyl group

and aromatic ring in epoxy occur in the same chemical structure, inferring chemical bonding within those *IEPM* since we do not observe simultaneity of the four major absorption peaks in 0-*IEPM*- t_c with larger t_c . Chemical maps, obtained using the same *nano-IR*, further exemplify chemical bond richness, elucidating high improbability that a physical mixture (≤ 80 nm) could consistently contain both the urea carbonyl group and aromatic ring in epoxy. Conversely, the spectrum of 0-*IEPM*-3.5 appears to be weak in polyurea / epoxy simultaneity, which tends discernably to the inverse for lower t_c , and validates that reaction kinetics (t_c) are inversely related to chemical bond richness. Chemical bonding (and its richness) across *IEPM* may also be described using non-negative matrix factorization (NMF) analysis, revealing intensities of *nano-IR* peaks in decomposed vectors. Finally, DMA results distinguish between loss modulus at various t_c , and TMA distinguishes between C-*IEPM*- $t_c = 24$ (which we believe is, at best, comprised solely of physical mixture) and C-*IEPM*- $t_c < 24$, in addition to *IEPM* re-generativity characteristics.

Digging deeper, AFM and chemical images at smaller length scales, Figure 3, reveal discrepancies between samples 0-*IEPM*-0 and 0-*IEPM*-2.5. Sample 0-*IEPM*-0.5, Figure 3(a), depicts large epoxy grains (“pebbles”) adjacent to bulky epoxy and a gradual change of grain size along the direction from epoxy to *IEPM*. Chemical bonding is evidenced in Figures 3(b) and 3(c) where the chemical mapping of epoxy (1510 cm^{-1}) and polyurea (1550 cm^{-1}) wavenumbers reveals the presence of both epoxy and polyurea; “yellow” or “red” affirms presence of each substance. Since epoxy and polyurea are present at the same location, the presence of chemical bonding can be predicted. Furthermore, 0-*IEPM*-0.5 shows a polyurea-rich region at the boundary which is also an epoxy-rich region,

demonstrating the presence of strong chemical bonding in the mixed region, and penetration of polyurea beyond the surface of curing epoxy. However, the common-area blue regions in Figures 3(b) and 3(c) indicate no presence of epoxy or polyurea, likely due to “dips” in the surface of sample after the microtome procedure. In contrast, 0-*IEPM*-1.0 depicts a uniform size of smaller epoxy grains, attributed to decreased diffusivity of migrating epoxy species at $t_c = 1$ and a decrease in particle density. However, “red” or “yellow” regions in Figures 3(e) and 3(f), 0-*IEPM*-1, may be an indicator of richer chemical bonding and greater simultaneity of epoxy and polyurea. Furthermore, when a scanned region is devoid of a cogent *IEPM* layer, chemical mapping, i.e., wavenumber mapping across the chemical image, reveals discernible separation between epoxy and polyurea. For example, when mapping the wavenumber of polyurea-feature-peak across polyurea, a color change, indicating high laser-intensity, is observed (e.g., yellow or red). However, when mapping the wavenumber of epoxy-feature-peak across the same polyurea image, a significant contrast in color is observed, where the “flipped” color (to blue), albeit still at high laser-intensity, indicates absence of epoxy. This occurs in sample 0-*IEPM*-2.5, where the blue region in Figure 3(h) reveals no presence of epoxy on the polyurea side of the interface (using 1510 cm^{-1} epoxy wavenumber mapping) while Figure 3(i) reveals pure polyurea (1550 cm^{-1} polyurea wavenumber mapping); this signifies a distinct boundary and minimal presence of chemical bonding, likely signaling reduction in shear resistance (during the cutting process).

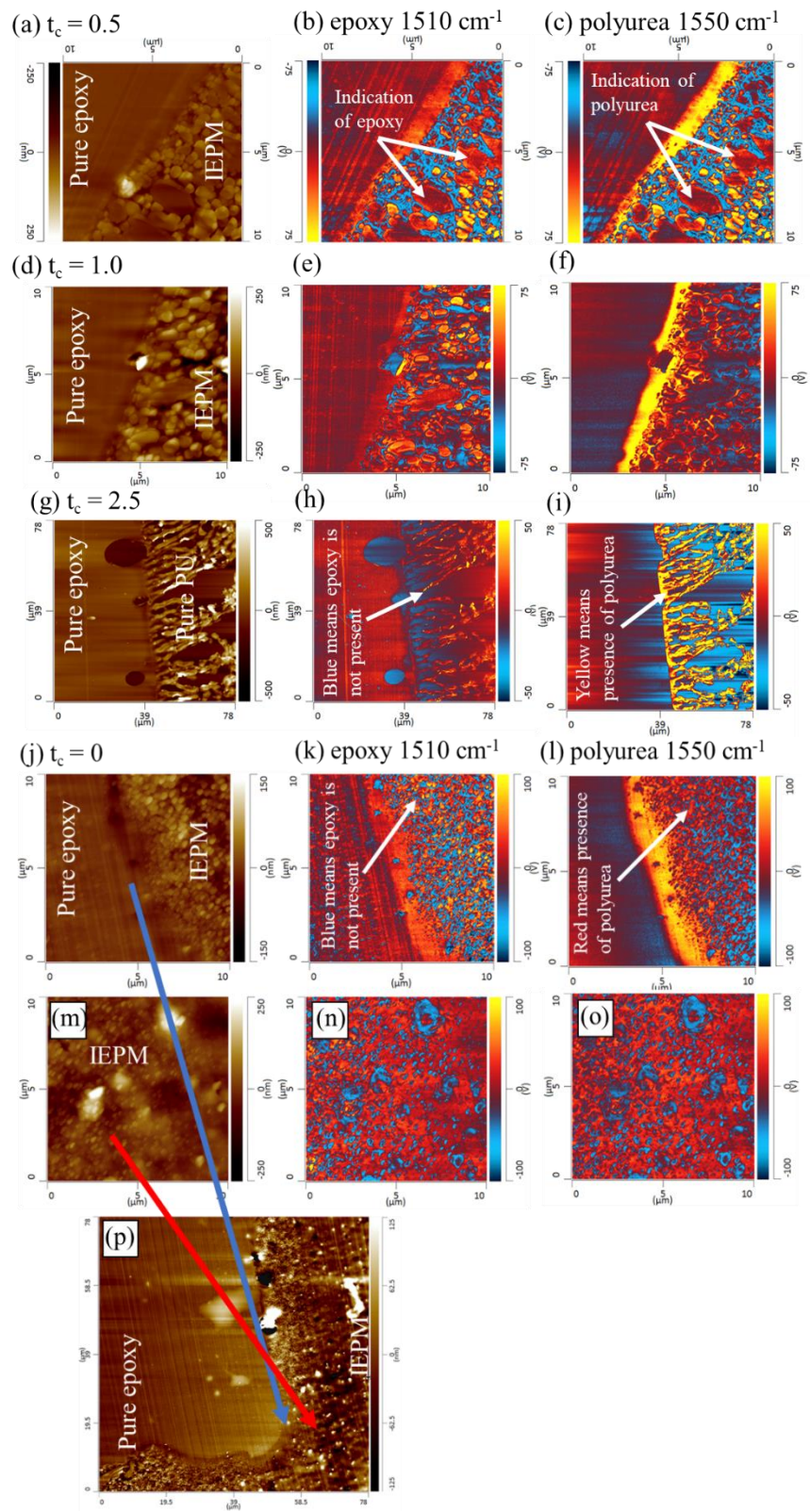


Figure 3. Magnified AFM images and chemical images of various types of *IEPM*: (a) – (i) : *IEPM*-0.5, 1.0, and 2.5; and (j) - (p): *IEPM*-0

Figures 3(j) through 3(p) show chemical images of 0-*IEPM*-0, introduced in Figure 1, at the epoxy-*IEPM* border (blue arrow) and into the *IEPM* (red arrow). A comparison of *IEPM* widths reveals that interface grain size of 0-*IEPM*-0 is smaller than that of 0-*IEPM*-0.5, but grain size decreases again when $t_c > 1$, e.g., 0-*IEPM*-2.5; however, the small grain size in 0-*IEPM*-0 indicates that reactivity of curing epoxy does not maximize upon initial mixing (although *IEPM* width does), where lower-viscosity epoxy ostensibly produces larger epoxy-polyurea grains. Chemical images, Figures 3(k) through 3(l), support the notion that epoxy diffusivity is less in 0-*IEPM*-0 since the wavenumber mapping of polyurea signals (1550 cm^{-1}), Figure 3(l), is slightly greater than mapping of epoxy signals (1510 cm^{-1}), Figure 3(k).

Non-negative matrix factorization (NMF)

NMF modeling was used to identify *IEPM* characteristics through statistics, verifying presence of chemical bonding. Figure 4 shows the three representative deconvoluted Vector spectra and corresponding Vector intensity loading maps, corresponding to 100 points across 0-*IEPM*-0.5, see Figure 2(b), and 0-*IEPM*-2.5, see Figure 2(h). A significant chemical bond feature is shown by the circled regions containing peaks 1510 cm^{-1} , 1550 cm^{-1} , 1606 cm^{-1} , and 1642 cm^{-1} , indicating presence of both polyurea and epoxy. In Figure 4(a), 0-*IEPM*-0.5 the corresponding loading indicator maps 1 and 3 indicate high intensity (yellow and turquoise, respectively) and widespread distribution of these four peaks across a significant portion of the interface, signifying a rich composition of chemical bonds. However, NMF of 0-*IEPM*-2.5 sample obtains only an epoxy Vector (Vector 3) and two polyurea Vectors (Vectors 1 and 2) as shown in Figure 4(b); there are

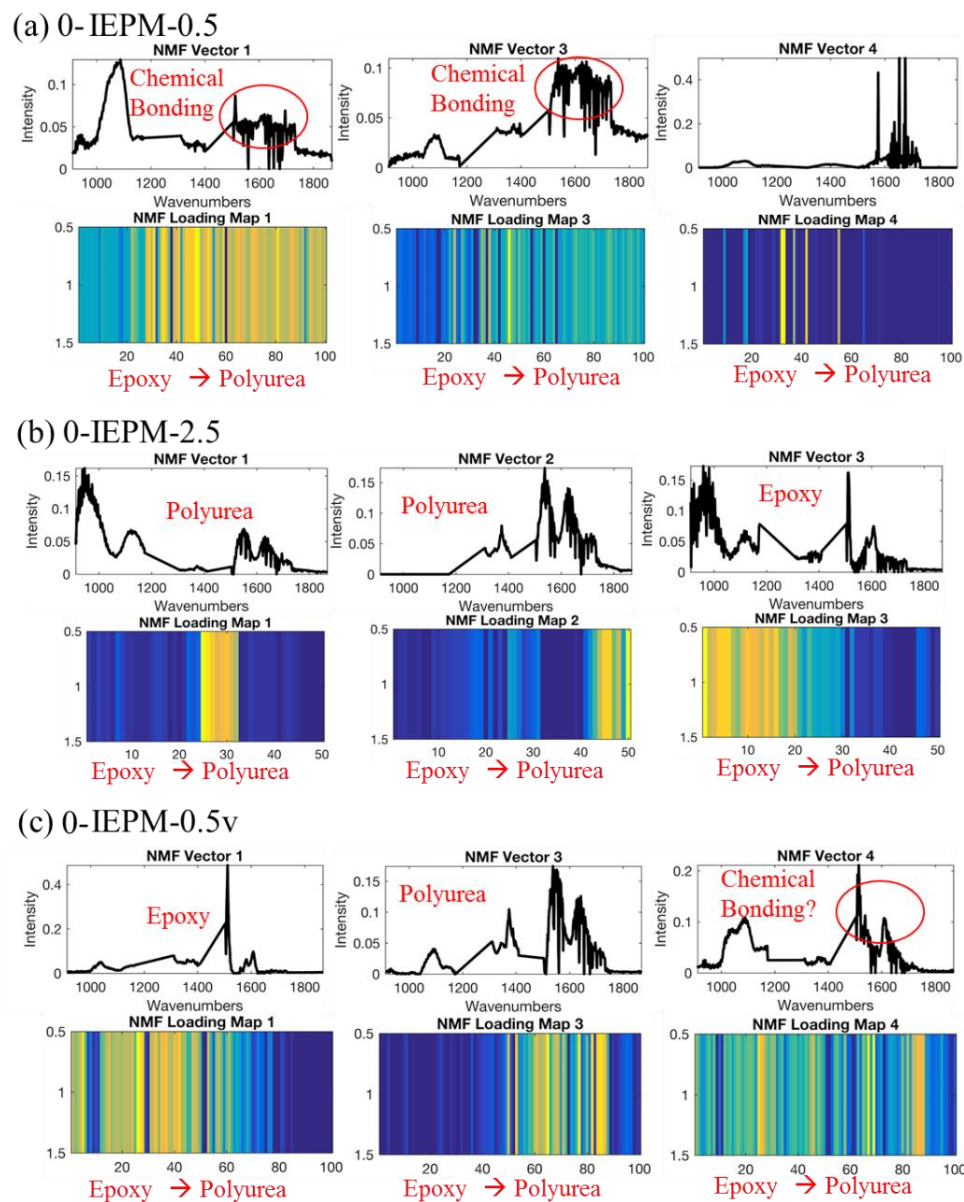


Figure 4. NMF vectors and corresponding intensity loading maps for: (a) 0-IEPM-0.5; (b) 0-IEPM-2.5; (c) 0-IEPM-0.5v

no de-convoluted Vectors that include both polyurea and epoxy peaks. Additionally, a clear boundary exists between epoxy and polyurea at points 20-25. Therefore, the reason NMF analysis does not obtain a chemical bond indicator for 0-*IEPM*-2.5 is that no significant interface characteristics exist in its *nano-IR* spectra.

Figure 4(c) shows NMF results of 0-*IEPM*-0.5v. Vectors 1 and 3 reveal clear patterns of epoxy and polyurea. Loading maps of Vectors 1 and 3 confirm locations of epoxy and polyurea via their intensity distribution, but they do not indicate pervasive (rich) chemical bonding akin to 0-*IEPM*-0.5 in Figure 4(a). Additionally, Vector 4 shows a combination of epoxy and polyurea peaks attributed to chemical bonding, but with a higher fraction of epoxy features than we observed in 0-*IEPM*-0.5, which attribute to slower diffusivity of migrating epoxy species associated to higher-viscosity epoxy, resulting in a narrower *IEPM* region, see Figure 2(l), and less reactivity between isocyanate and amine hardener in epoxy.

Linking Nanoscale Findings to Impulse (Shock) Dynamics (Ballistics Test Results)

We analyzed a series of *IEPM* chemical structures as a function of epoxy diffusivity (in terms of t_c), engendering significant chemical bond richness (simultaneity of high-frequency peaks ($> 1500\text{cm}^{-1}$), i.e., pervasive distribution of “red” / “yellow” intensities): (1) in wide *IEPM* region (e.g., width of *IEPM*-0 = 50 μm , see Table S2); (2) using fast epoxy diffusivity (resulting in large epoxy grain sizes, lower t_c) and lower-viscous epoxy; and (3) fabricating multiple *IEPM* layers within a multi- x -*IEPM*- b - t_c panel architecture. According to the results in Figure 3, samples 0-*IEPM*- $t_c \leq 1$ embody attributes (1) or (2). A large-scale experimental test regime was used to link nanoscale changes to *ME.T* (in

terms of loss modulus) in ballistics-resistant panels comprised of two or four layers of C - $IEPM$ - b - t_c , where C =carbon fiber.

DMA (loss modulus) and SEM (fractography) results (t_c).

DMA was used to link loss modulus and storage modulus material properties to molecular vibrational modes and bond enthalpy, see Table 1, as well as $IEPM$ chemical bonding, quality, and width as a function of t_c as observed in Figures 2 and 3. The six 0 - $IEPM$ - t_c bar samples (30 mm x 7 mm) in Table S2, held in single cantilever mode, were designed as a function of t_c and were excited over a frequency range 0.1 Hz and 10 Hz. Figure 5(a) compares loss modulus of several $IEPM$ - t_c , which is nearly zero for 0 - $IEPM$ -24, indicating some type of physical mixture and also revealing presence of gaps between regions of pure epoxy and pure polyurea (confirmed via SEM). Loss modulus is inversely related to t_c , educing three general groupings: (a) $t_c = 0$ h; (b) $t_c = 0.5$ h, 1.0 h, 2.0 h, and (c) $t_c = 3.5$ h, 24 h. The fix-fix boundary condition of the beams elicits a dominant translational (longitudinal) first mode of vibration, see previous work by He et al.,⁸ indicating a possible stretching of bonds C-C, C=C, C-N, or C=O to dissipate energy. Furthermore, Figure 5(b) shows that $IEPM$ -0 has the largest storage modulus (comprised of elastic deformation since samples were not loaded post-elastically), indicating strong presence of large enthalpic C=C and C=O bonds in conjunction with C-C, N-H, C-N, and C-O bonds, comprising a rich $IEPM$ constitution at lower t_c in accordance with Table 1, thus, as Figures 4(a), 5(a), and 5(b) support, maximizing ability of $IEPM$ structures to transfer energy (via stretching and bending modes) and enhancing $IEPM$ loss modulus (material damping) and bond strength, where stored energy expended during motion of

molecules is recovered.

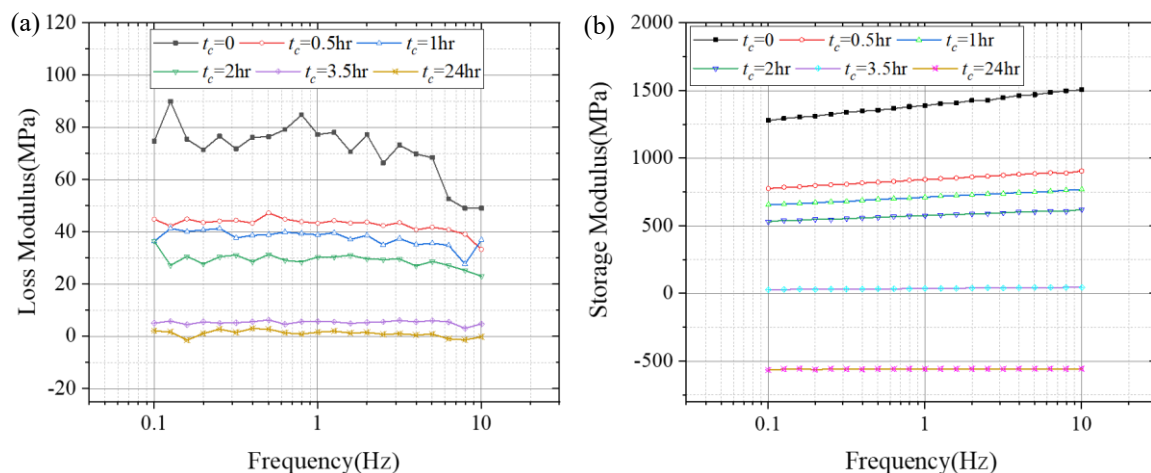


Figure 5. DMA results of six 0-IEPM- t_c test samples (with adjoined epoxy), measuring (a) loss modulus; and (b) storage modulus

Inverse relationship of t_c and chemical bond richness, including influence of stretching and bending bonds, is supported via SEM results. Figure 6 depicts various C -IEPM- t_c microstructures, where $t_c = 0$, see Figure 6(a), produces largest IEPM width (~ 30 μm according to SEM), and loss modulus and storage modulus (Figure 5). For IEPM comprised of larger t_c , e.g., $t_c = 2.5$ h, Figure 6(b), and $t_c = 24$ h, Figure 6(c), loss modulus and storage modulus of IEPM are substantially less, correlating to less IEPM width and quality, where IEPM-24, eliciting no chemical reaction, shows distinct interfacial gap. Comparison of CF/E and C -IEPM-4 fractographs in Figures 6(d) and 6(e) indicate fracture boundary and in epoxy matrix; conversely, CF/E cracking propagates unstably along fiber-epoxy boundary. Finally, Figure 6(f) depicts a more uniform, or transitional, IEPM structure, observed even at large t_c , e.g., IEPM-3 relative to its IEPM-4 counterpart in Figure 6(g). Similarly, Figures 6(a) - (c) correlate to Figures 5(a) and (b), indicating that loss modulus and storage modulus

of *IEPM* and fracture toughness of *C-IEPM* may be designed per t_c in accordance with the chemical bonds in Table 1 and their molecular vibrational properties.

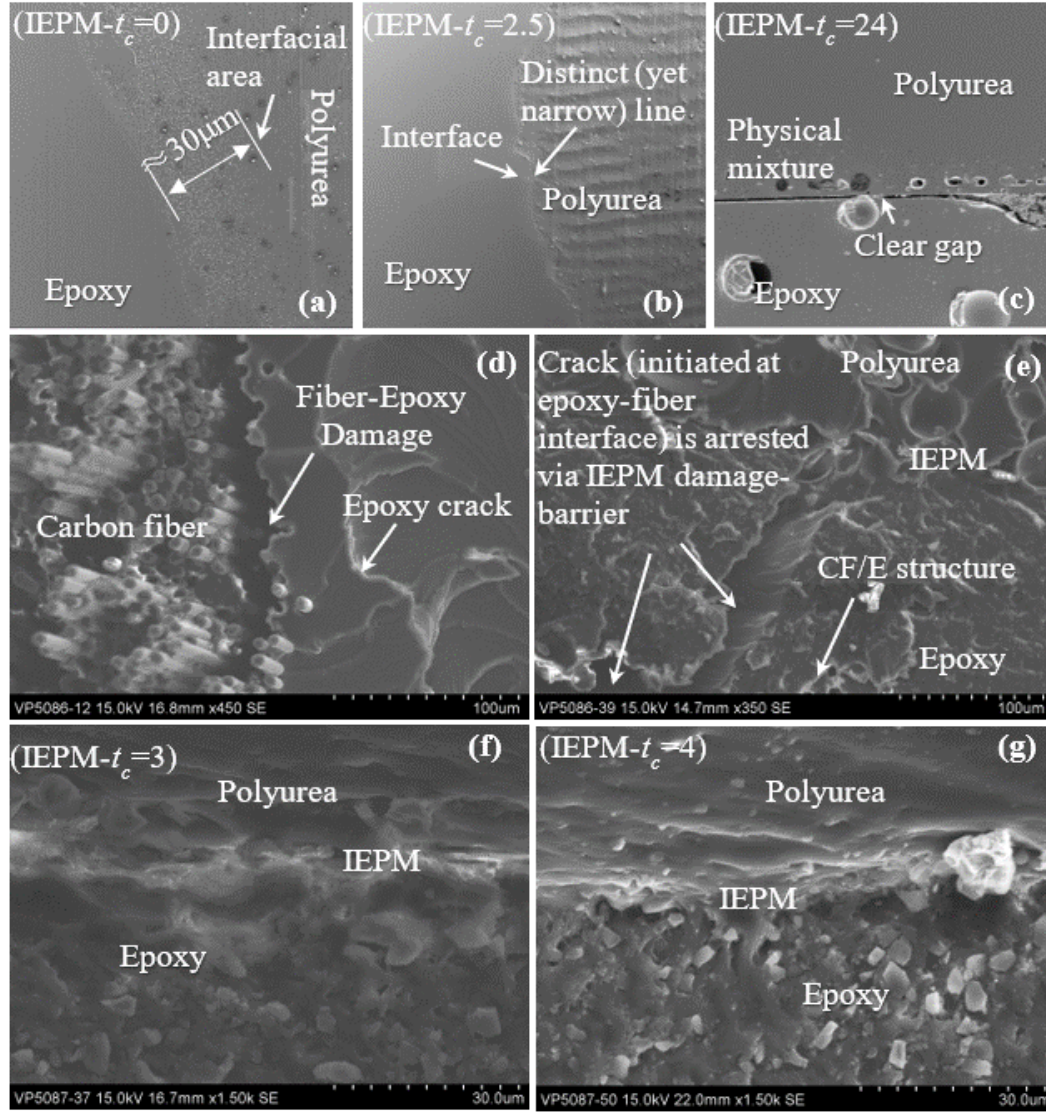


Figure 6. Scanning electron microscope (SEM) images of: (a) - (c) *C-IEPM- t_c* for $t_c = 0$; $t_c = 2.5$, and $t_c = 24$; (d) - (e) fractographs of *CF/E* and *C-IEPM-4*; and (f) - (g) comparison of uniformity and transitionality of *IEPM- t_c* for $t_c = 3$ and $t_c = 4$

Although the amount of -NCO that reacts with epoxide and -NH_2 from epoxy hardener to produce a rich *IEPM* composition of C-C, C=C, N-H, C-N, C=O, and C-O bonds (and influence loss and storage modulus in *IEPM*) is not determined, thus potentially influencing composition of the overlying polyurea, storage modulus of this top-coat polyurea is generally unaffected by t_c (as *IEPM* richness changes); however, at $t_c=24$ h, after completion of exothermic epoxy reaction, T_g and storage modulus of the top-coat polyurea (elastomer) are expectedly larger.

TMA Results and Regeneration of IEPM. TMA Q400 instrument was used to ascertain potential re-reaction of *IEPM-t_c* in four samples, *C-IEPM-t_c* = 2.5, 3.5, and 24, by examining percent Dimensional Change (ΔD) of each sample against rising Temperature (T). TMA results indicate discernable (and unique) glass transition temperature, T_g , for *IEPM-2.5* and *IEPM-3.5*, where re-generativity of the former (at $t_c = 2.5$) also occurs (upward slope after $T_g = 140.66^\circ\text{C}$). However, unique T_g is not evident in *IEPM-24* structure (nor is its re-generation), where T_g is only observed for epoxy and for polyurea. We therefore believe that grafting the functionality of isocyanate-derived polyurea to ongoing epoxide-amine cross-linking, even at higher values of t_c , results in some degree of chemical bonding (and physical mixture), but no chemical bonding at $t_c = 24$ h (using a fully-cured epoxy).

Ballistics-Resistance Results. We demonstrate multi-scopicity using *C-IEPM-b-t_c* ballistics resistant structures under extreme dynamics environment by probing *IEPM* nanostructure to cross-link with a cross-linking evolution (“double” cross-link), eliciting chemical bonding and interface quality. Loss modulus and storage modulus helps to

maximize efficacy of *IEPM* reaction, therefore minimizing number of *IEPM* layers and fiber volume fraction. The first testbed is twenty-five 30.5 cm \times 30.5 cm (12 in \times 12 in) panels, comprising two or four layers of *C-IEPM-b-t_c* (5 sheets of carbon-fiber per layer), subject to five types of ballistics (*b*) caliber cartridges. The results are summarized in Table 2. We considered various *t_c*, two types of polyurea (*PU*) – aliphatic (*AL*) and aromatic (*AR*) – low ($\nu = 534$ cps) and higher ($\nu = 1,367$ cps) viscosity epoxy-resin, and two types of layering architectures (panels using four layers of *IEPM* and panels using two layers of *IEPM*), see the sketch in Table 2. Test results for .44 magnum caliber impacts (rated muzzle energy is 1,036 ft-lbs) show 0% “Pass” rate for four-layer samples when the two inner *IEPM* layers are designed by cross-linking isocyanate-based aliphatic polyurea with epoxide-amine cross-linking at $t_c > 3.0$ h; this is consistent for better-quality *IEPM* that is engendered using low ν (5 samples), compare Figures 2(b) and 2(l). Additionally, back-end layers of *C-IEPM-b-t_c* samples designed with only two layers (sample Nos. 10-15) were perforated, i.e., full projectile (bullet)-perforation, by cartridges with rated muzzle energies exceeding 335 ft-lbs (9 mm Luger). However, against .44 magnum caliber jacketed soft point cartridges, the “Pass” rate of four of the four-layer *C-IEPM-b-t_c* samples (Nos. 18, 19, 22, 23), where two inner *IEPM* were designed using smaller values of t_c ($1.75 < t_c < 2.53$ h), was 100%. DMA of *IEPM-2* ($t_c = 2$ h), see Figure 5(a), reveals a loss modulus 200% larger than that of *IEPM-24*, pure epoxy or polyurea, leading to the higher “Pass” rate. The remaining panels in the all-aliphatic (AL-AL) group, sample Nos. 16-25 where inner *IEPM-t_c* > 2.75 h, show 0% “Pass” rate, accentuating the importance of *IEPM* quality and chemical bond richness, entailing a wider interface. However, subjected to lower muzzle velocity impact (.357 magnum), panels *C-HMC/ IEPM-b-t_c* < 4.0 h, i.e., having

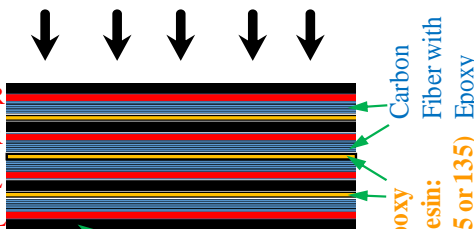
larger t_c , also exhibited no back-end layer perforation.

A comparison of polyurea-type in the formation of *IEPM* reveals that an epoxy-aliphatic PU functional group reaction, see sample Nos. 18 and 19 ($2.07 < t_c < 2.53$ h), passed the .44 magnum impacts, whereas sample No. 3, whose *IEPM* was realized via epoxy-aromatic PU functional group reaction with similar t_c ($t_c \sim 2.5$ h), fails the impact tests. This may be due to the introduction of moisture (and hence urethane linkages) via reaction of isocyanate (methylene diisocyanate) with polyether polyol in *AR PU*, thus hindering reactivity of $-(NCO)$ functional groups with epoxy-based groups, leading to low quality *IEPM*. In this light, sample No. 6 ($t_c = 1.6$), whose four *IEPM* layers were construed as epoxy-*AR PU* functional group reaction, failed the .44 magnum impact.

AFM in Figure 2(k) and NMF in Figure 4(c) show that width and chemical bonding are more prominent in *IEPM* that is derived using low-viscosity epoxy (with “LAM-125” resin) as opposed to medium-viscosity epoxy (with “LAM-135” resin). As a result, the former engenders higher-quality *IEPM*, enhancing panel resistance against .357 magnum impact. An inverse relationship between epoxy viscosity and migration of epoxy species / reactivity is observed by comparing the following samples: Sample No. 3 (low ν) / Pass and No. 2 (medium ν) / Fail; No. 7 / Pass and No. 8 / Fail; No. 16 / Pass and 17 / Fail, and No. 18 / Pass and No. 17 / Fail. The four comparisons are based on similar t_c and the same *PU*.

Table 2

Test results of C-IEPM-b-t_c ballistics-resistant panels; caliber range: .22LR to .44 Magnum

Specimen No.	C-IEPM-b-t _c Ballistics Panels (0.6-in to 0.75-in thick)				Caliber Cartridges (Muzzle Energy, ft.-lbs)				
	Inner Left (PU Type)/ Inner Right (PU Type)	Epoxy (125/226: 534 cps; 135/226: 1,367 cps)	Outer Left (PU Type)/ Outer Right (PU Type)	Epoxy (125/226: 534 cps; 135/226: 1,367 cps)	.22LR (130)	9mm Luger (335)	.45 ACP (365)	.357 Magnum (548)	.44 Magnum (1036)
1	2.53 (AL)/ 2.48 (AL)	135	2.5 (AR)/ 2.5 (AR)	125	Pass	Pass	Pass	Pass	Fail
2	2.53 (AL)/ 2.63 (AL)	135	2.5 (AR)/ 2.5 (AR)	125	Pass	Fail	Pass	Fail	Fail
3	2.45 (AL)/ 2.43 (AL)	125	2.5 (AR)/ 2.5 (AR)	125	Pass	Pass	Pass	Pass	Fail
4	3.37 (AL)/ 3.47 (AL)	125	2.48 (AR)/ 2.5 (AR)	125	Pass	Pass	Pass	Pass	Fail
5	4 (AL)/ 4.25 (AL)	125	2.5 (AR)/ 2.48 (AR)	125	Pass	Fail	Fail	Pass	Fail
6	1.6 (AR)/ 1.62 (AR)	125	2.5 (AR)/ 2.5 (AR)	125	Pass	Pass	Pass	Pass	Fail
7	2.5 (AR)/ 2.87 (AR)	125	2.5 (AR)/ 2.55 (AR)	125	Pass	Pass	Pass	Pass	Fail
8	2.48 (AR)/ 2.5 (AR)	135	2.48 (AR)/ 2.5 (AR)	135	Pass	Pass	Pass	Fail	Fail
9	2.52 (AR)/ 2.62 (AR)	135	2.5 (AR)/ 2.5 (AR)	135	Pass	Pass	Pass	Fail	Fail
10	2.52 (AR)/ 2.57 (AR)	135	<div>Only two IEPM layers in Specimens 10 - 15</div> 	Pass	Pass	Fail	Fail	Fail	
11	2.5 (AR)/ 2.5 (AR)	135		Pass	Fail	Fail	Fail	Fail	
12	2.52 (AR)/ 2.5 (AR)	135		Pass	Fail	Fail	Fail	Fail	
13	2.5 (AR)/ 2.5 (AR)	135		Pass	Pass	Fail	Fail	Fail	
14	2.6 (AR)/ 2.58 (AR)	135		Pass	Fail	Fail	Fail	Fail	
15	2.5 (AR)/ 2.5 (AR)	135		Pass	Fail	Fail	Fail	Fail	
16	3.55 (AL)/ 3.98 (AL)	125/125	2.5 (AL)/ 2.5 (AL)	125/125	Pass	Pass	Pass	Pass	Fail
17	2.75 (AL)/ 2.07 (AL)	135/135	2.5 (AL)/ 2.5 (AL)	135/135	Pass	Fail	Fail	Fail	Fail
18	2.07 (AL)/ 2.47 (AL)	125/125	2.48 (AL)/ 2.5 (AL)	125/125	Pass	Pass	Pass	Pass	Pass
19	2.22 (AL)/ 2.53 (AL)	125/125	2.48 (AL)/ 2.5 (AL)	125/125	Pass	Pass	Pass	Pass	Pass
20	3.35 (AL)/ 3.75 (AL)	125/125	2.67 (AL)/ 2.5 (AL)	125/125	Pass	Fail	Pass	Pass	Fail
21	3.25 (AL)/ 4.2 (AL)	125/125	2.5 (AL)/ 2.47 (AL)	125/125	Pass	Pass	Pass	Fail	Fail
22	1.8 (AL)/ 1.77 (AL)	125/125	2.5 (AL)/ 2.48 (AL)	125/125	Pass	Pass	Pass	Pass	Pass
23	1.75 (AL)/ 1.92 (AL)	125/125	2.5 (AL)/ 2.5 (AL)	125/125	Pass	Pass	Pass	Pass	Pass
24	4.42 (AL)/ 3.22 (AL)	125/125	2.5 (AL)/ 2.5 (AL)	125/125	Pass	Pass	Fail	Fail	Fail
25	3.83 (AL)/ 3.83 (AL)	125/125	2.5 (AL)/ 2.52 (AL)	125/125	Pass	Pass	Pass	Pass	Fail
PASS RATE for four IEPM layer specimens (Spec Nos. 1-9; 16-25)					100.0%	78.9%	84.2%	68.4%	21.1%

Based on the results in Table 2, 40% of *C-IEPM-b- t_c* samples (Nos. 18, 19, 22, and 23) with *IEPM* that were produced using only aliphatic polyurea passed .44 magnum impact; the range of shortest cure times in these samples is $1.75 \leq t_c \leq 2.22$ h while the longest value of t_c is approximately 2.5 h. In accordance with Figures 3(d) – 3(f), Figures 3(g) – 3(i) and Figure 4(b), there appears to be sufficient *IEPM* chemical bonding to sufficiently enhance loss modulus. Thirteen out of 19 panels designed with 4 layers of *IEPM* (and using either *AR* or *AL* agents) pass the .357 impact (which has about 50% muzzle energy of .44 magnum), and because t_c is less critical for lower-energy impacts, 5 out of 7 panels designed with at least one layer of *IEPM- $t_c > 3.0$* passed. Furthermore, 84% of panels (with 4 *IEPM* layers) passed the impact by .45 ACP caliber (about 30% muzzle energy). Finally, only 2 out of 6 panels designed with two *IEPM* layers (*IEPM- $t_c \sim 2.5$*) passed the 9mm Luger impact, and all panels passed low-velocity caliber impact (.22 LR), 130 ft-lbs, including two panels (Nos. 5 and 24) with $t_c > 4.0$ h.

To ascertain consistency with our findings and establish a repeatable link between impact dynamics and *IEPM* quality (relative to t_c and ν), we designed two additional test programs in accordance with Table S3: (A) four panels were manufactured using $t_c = \langle 0, 1.5, 2.5, 24 \rangle$ by sequentially adhering four groups of 5-carbon-fiber layers with *IEPM- t_c* engendered after each 5th layer using medium-viscosity epoxy-resin throughout; and (B) four panels were manufactured as described in text program A for $t_c = \langle 0, 0.5, 1.5, 2.5 \rangle$ using low-viscosity epoxy-resin. Two .45 ACP caliber, two .357 magnum caliber, and two .44 magnum caliber cartridges were fired into each of eight panels. Results are summarized in Table 3 in accordance with Table S3. In test program A, eight out of twelve impacts failed to perforate back-end layers of Sample Nos. A1v and A2v, hence

“Passing,” with the exception of four .44 magnum caliber bullets. A comparison to Sample Nos. 18, 19, 22, and 23 ($1.77 \leq t_c \leq 2.5$) – all which captured .44 magnum caliber bullets, Table 2 – elucidates poor-quality *IEPM* engendered per higher-viscosity (ν) epoxy-resin, see Figure 2(l), t_c notwithstanding. The results are consistent with findings in Figure 7 that evidence regeneration of *IEPM* as temperature continues to increase above the T_g of *IEPM* designed using lower ν . For common ν , comparison of Sample No. A2 ν ($t_c = 1.5$ h) to Sample No. 17 ($2 < t_c < 3$) reveals substantial improvement in impact resistance to .357 magnum and .45 ACP caliber bullets, where $t_c \sim 1.5$ h threshold appears consistent with findings on loss modulus, Figure 5(a). Sample No. A3 ν captured one bullet (.45 ACP); two .44 magnum caliber, two .357 magnum, and one .45 ACP caliber bullets perforated and exited the panel back-end. A comparison to Sample Nos. 1 and 2 (Table 2), where two *IEPM* were engendered using aromatic polyurea but with lower-viscosity resin, reveals panel failure in three out of four impacts: .357 and .44 magnum caliber bullets (both panels survived .45 ACP impacts), implying that albeit a “balance in degree of *IEPM* quality” between polyurea-type and epoxy-resin viscosity, ν may be the more critical design parameter of the two, see also comparison of Sample No. A3 ν to Sample Nos. 8 and 9. Finally, although Sample No. 17 failed .44 magnum, .357 magnum, and .45 ACP caliber impacts, similar to Sample No. A3 ν , Sample No. 18 – using lower ν (and aliphatic polyurea) and similar t_c (~ 2.5) – passed all impact tests. Therefore, while results of panels with *IEPM*- $t_c = 2.5$ may exhibit some inconsistency, considering inherent variability per a “hand-made” manufacturing process, the findings of test program A corroborate Table 2 test results, i.e., that lower t_c (and lower ν , in addition to aliphatic polyurea) engender a desirable *IEPM*. In test program B, we measured the approach impact velocity using a

chronograph, see measured values in Table 3. Only one (.44 magnum caliber bullet) out of twenty-four (24) impacts perforated back-end of one of four test panels (Sample B4, $t_c = 2.5$), confirming that: (1) higher-viscosity epoxy-resin, even at lower t_c (e.g., 0 - 0.5), compromises *IEPM* quality, see Figure 2(1), by reducing *IEPM* chemical bond richness across narrow interface; and (2) securing of .44 magnum caliber bullet requires $t_c \leq 1.5$.

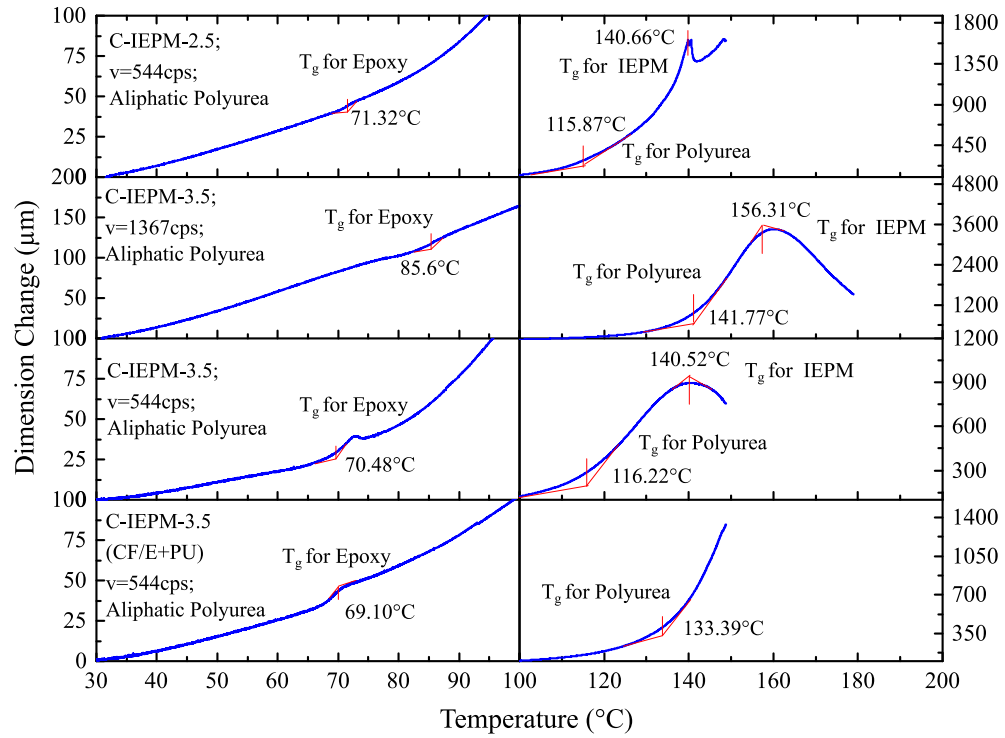


Figure 7. TMA results for three *C-IEPM- t_c* test samples, where we observe T_g for epoxy and polyurea in each sample, but T_g for the interface (chemical bonding) only in *C-IEPM-2.5* and *C-IEPM-3.5*, not in the case when polyurea is applied to fully cured epoxy

Table 3*Ballistics test results for Test Programs A and B*

Panel Design (<i>C-IEPM-b-t</i> , v, aliphatic polyurea)												
Test Program		A (v=1,367 cps)					B (v=534 cps)					
Result: Pass (P) / Fail (F)												
Spec No. (t _c)	Λ1v (0)	Λ2v (1.5)	Λ3v (2.5)	Λ4v (24)	B1 (0)		B2 (0.5)		B3 (1.5)		B4 (2.5)	
Caliber					(vel, fps)		(vel, fps)		(vel, fps)		(vel, fps)	
.45 ACP	P P	P P	P F	F F	P(787)	P(757)	P(783)	P(782)	P(765)	P(813)	P(764)	P(778)
.357 magnum	P P	P P	F F	F F	P(1218)	P(1244)	P(1214)	P(1237)	P(1226)	P(N.R.)	P(1243)	P(1214)
.44 magnum	F F	F F	F F	F F	P(1562)	P(1527)	P(1530)	P(1592)	P(1551)	P(1552)	F(1541)	P(1502)
N.R. - Not Recorded												

N.R. - Not Recorded

IEPM chemical bond richness, identified by nanoscale changes in *IEPM-t_c* affecting chemical bond richness and interface quality, is confirmed via TMA in Figure 7 and via NMF statistics in Figure 4, and via comparison of Figures 3(b) / 3(c) through Figures 3(h) / 3(i), is quantifiably linked to loss modulus (material damping) in *C-IEPM-t_c* (at lower t_c), prohibiting perforated back-end panel damage per impact dynamics. In Figure 7, as T_g for *IEPM* is approached, molecular segmental motions activate, and energy is dissipated via molecular friction (heat) where motions occur with difficulty – noting that material / *IEPM* stiffness decreases (as molecules can move more freely per decline in storage modulus) – signifying increase in loss modulus. Interestingly, not only does *IEPM* quality improve through lower t_c , lower ν , and aliphatic polyurea moieties, but *IEPM* regenerativity, see Figure 7, means its storage modulus / stiffness increases, eliciting a unique systems of high elongation resistance and molecular friction conducive for large impact (shock) dynamics environment.

CONCLUSIONS

A synthesizable Interfacial Epoxy-Polyurea chemically hybridized-Matrix (*IEPM*) was designed for a fibrous (x) hybrid polymeric matrix composite architecture. x -*IEPM*- t_c , characterized by *IEPM* as a function of the curing time (t_c) of a two-part epoxy system (resin-hardener mixture), may be used to dial-in loss modulus properties, leading to macro-scale property design in high-impact dynamics environments. The nanoscale morphology and chemical structure of *IEPM*, after grafting isocyanate-derived polyurea functionality to backbone of evolving epoxide-amine cross-linking, leading to a potential library of designable x -*IEPM*- t_c bulk material properties, were investigated by SEM, AFM, and *nano-IR*. AFM images and FTIR spectra reveal prominent *IEPM* in samples having shorter t_c , elucidating chemical bond richness, and *IEPM* quality (fewer defects/ voids) and width (ranging from 2 μm for longer t_c to 50 μm at $t_c = 0$). Furthermore, NMF statistical modeling was used to identify *IEPM* characteristics using de-convoluted vector spectra and corresponding vector intensity loading maps, revealing a rich composition of chemical bonds particularly across *IEPM*- $t_c=0$, where points consistently displayed simultaneity of polyurea and epoxy higher absorption peaks (1510 cm^{-1} , 1550 cm^{-1} , 1606 cm^{-1} , and 1642 cm^{-1}).

In *IEPM* designed with small t_c , there is strong presence of chemical bond richness that improves interface cohesion (bond enthalpy) and reduces *IEPM* defects. Across *IEPM* width, a three-part reaction between (epoxide) + (amine epoxy hardener) + (isocyanate) introduces critical urea bonds to the epoxy system, via chemical bonding, engendering desirable molecular vibrational properties, specifically C-C stretching, C=C stretching of aromatic rings, N-H bending, C-N stretching, and broad urea carbonyl stretching bonds at

single nanoscale points. The chemistry of *IEPM* nanostructures, supported via statistics of NMF analysis of the IR spectra data and also physically by the tip-size of the nano-IR laser tip (80 nm) which is smaller than polyurea or epoxy molecule size, correlates well to bulk material properties, such as loss modulus, which shows 100% increase for $IEPM-t_c=0$ relative to $IEPM-t_c=0.5$, and glass transition temperature (and *IEPM* re-generativity), per $x-IEPM-t_c$ design.

In a first-series of ballistics test results, forty-percent of ballistics-resistant (*b*) panels, manufactured with four layers of *C-IEPM-b-t_c* that utilized $IEPM-t_c \sim 2$, aliphatic-based polyurea groups, and low-viscosity epoxy-resin, passed .44 magnum caliber impact tests. In order to confirm these results and to explore utilizing *IEPM* chemistry per lower t_c , two additional ballistics test programs were designed, confirming: (1) promising results of the first test for panels designed using lower t_c (per the test program), and (2) *C-IEPM-b-t_c=0*, up to $C-IEPM-t_c \leq 1.5$ (and using low-viscosity epoxy-resin and also aliphatic polyurea), via mechanical energy transferability attribute (loss modulus), positively and consistently precludes perforation of back-end layers by .44 magnum caliber bullets.

ACKNOWLEDGMENTS

This research was partially supported by the Center for Nanophase Materials Sciences (CNMS) at the U.S. Department of Energy's Oak Ridge National Laboratory (ORNL), per Grant Nos. CNMS2017-R80 and CNMS2017-R59. The research was also supported by the Alabama Department of Transportation (ALDOT), project No. 930-935S. The authors would like to thank Dr. Weixing Sun for his efforts to process data and assist with IR analysis and chemical mapping. We also thank Drs. Alison Pawlicki and Songkil Kim for providing the necessary training for us to utilize the *nano-IR* instrument. We also thank Dr. Karren More and Ms. Shawn Reeves for meeting all of our microtoming needs. We also thank Dr. Alexei Belianinov for developing the statistical code for the NMF modeling of the IR point spectra. Finally, we thank Drs. Olga Ovchinnikova and Yangyang Wang for allowing access to the *nano-IR* and DMA test equipment, respectively.

ABBREVIATIONS

AFM - Atomic Force Microscopy;

SEM - Scanning Electron Microscopy;

DMA - Dynamic Mechanical Analysis

NMF - Non-negative matrix factorization;

IR - Infrared;

IEPM - Interfacial Epoxy-Polyurea hybridized-Matrix;

x-IEPM- t_c - x-Hybrid-polymeric Matrix Composite (t_c indicates the epoxy cure time; x indicates the fiber-type, where $x = 0$ means ‘no fiber’);

CF/E - Carbon Fiber-Reinforced Epoxy (for a carbon reinforced polymer, CFRP);

ME.T - Mechanical Energy Transfer;

SV - surface-to-volume ratio;

DGEBA - bisphenol A diglycidyl ether;

IPDI - isophorone diisocyanate;

MDI - methylene diisocyanate;

AL PU - aliphatic polyurea;

AR PU - aromatic polyurea;

REFERENCES

1. Vijayan P., P.; Puglia, D.; Al-Maadeed, M. A. S. A.; Kenny, J. M.; Thomas, S. Elastomer/Thermoplastic Modified Epoxy Nanocomposites: The Hybrid Effect of “micro” and “nano” Scale. *Materials Science and Engineering: R: Reports*, **2017**, 116, 1–29.
2. Department of Energy. Website. Fiber-Reinforced Polymer Composites: Pursuing the Promise. https://energy.gov/sites/prod/files/2015/04/f21/fiber_reinforced_composites_factsheet.pdf **2014**.
3. Industry Experts. Website. Carbon Fibers and Carbon Fiber Reinforced Plastics (CFRP) - A Global Market Overview. February **2014**.
4. Bakis CE, Bank LC, Brown V, Cosenza E, Davalos JF, Lesko JJ, Machida A, Rizkalla SH, Triantafillou TC. Fiber-Reinforced Polymer Composites for Construction—State-of-the-art Review. *Journal of composites for construction*. **2002** May;6(2):73-87.
5. Tarpani, J. R.; Maluf, O.; Gatti, M. C. A. Charpy Impact Toughness of Conventional and Advanced Composite Laminates for Aircraft Construction. *Materials Research* **2009**, 12, 395–403.
6. Han, S.; Chung, D. D. L. Mechanical Energy Dissipation Using Carbon Fiber Polymer–matrix Structural Composites with Filler Incorporation. *Journal of Materials Science* **2011**, 47, 2434–2453.
7. Gardea, F.; Glaz, B.; Riddick, J.; Lagoudas, D. C.; Naraghi, M. Identification of Energy Dissipation Mechanisms in CNT-Reinforced Nanocomposites. *Nanotechnology* **2016**, 27, 105707.
8. Attard TL, He L, Zhou H. Improving Damping Property of Carbon-Fiber Reinforced Epoxy Composite through Novel Hybrid Epoxy-Polyurea Interfacial Reaction. *Composites Part B: Engineering*. **2019** May 1;164:720-731.
9. Zhou, H.; Attard, T. L.; Dhiradhamvit, K.; Wang, Y.; Erdman, D. Crashworthiness Characteristics of a Carbon Fiber Reinforced Dual-Phase Epoxy–polyurea Hybrid Matrix Composite. *Composites Part B: Engineering* **2015**, 71, 17–27.
10. Zhou, H.; Attard, T. L.; Zhao, B.; Yu, J.; Lu, W.; Tong, L. Experimental Study of Retrofitted Reinforced Concrete Shear Wall and Concrete-Encased Steel Girders Using a New CarbonFlex Composite for Damage Stabilization. *Engineering Failure Analysis* **2013**, 35, 219–233.
11. Zhou, H.; Dhiradhamvit, K.; Attard, T. L. Tornado-Borne Debris Impact Performance of an Innovative Storm Safe Room System Protected by a Carbon Fiber Reinforced Hybrid Polymeric-Matrix Composite. *Engineering Structures* **2014**, 59, 308–319.
12. Zhou, H.; Attard, T. L.; Wang, Y.; Wang, J.-A.; Ren, F. Rehabilitation of Notch

Damaged Steel Beams Using a Carbon Fiber Reinforced Hybrid Polymeric-Matrix Composite. *Composite Structures* **2013**, 106, 690–702.

13. Saravanos D. A.; Chamis C. C. Tailoring of Composite Links for Optimal Damped Elasto-Dynamic Performance. Washington D.C.: NASA; **1989**. Report No.: 102094

14. He L, Attard TL, Zhou H, Brooks A. Integrating Energy Transferability into the Connection-Detail of Coastal Bridges using Reinforced Interfacial Epoxy-Polyurea Reaction Matrix Composite. *Composite Structures*. **2019** May 15;216:89-103.

15. Zhou H; Attard T.L. Bridge Girder Damage Quantification and the Retrofitting Techniques. NDE/ NDT for Highways and Bridges, *SMT conference* 2012; 2012 Aug 22-24; New York, NY **2012**.

16. Attard, T. L.; Abela, C. M.; Dhiradhamvit, K. Seismic FRP Retrofit of Circular Single-Column Bents Using a Ductility Wrap Envelope to Alter Failure Modes. *Engineering Structures* **2011**, 33, 1553–1564.

17. Schultz, A. B.; Tsai, S. W. Dynamic Moduli and Damping Ratios in Fiber-Reinforced Composites. *Journal of Composite Materials* **1968**, 2, 368–379.

18. Hazell PJ, Appleby-Thomas G. A Study on The Energy Dissipation of Several Different CFRP-Based Targets Completely Penetrated by a High Velocity Projectile. *Composite structures*. **2009** Nov 1;91(1):103-109.

19. Segal, C.L. High Performance Organic Fibers, Fabrics, and Composites for Soft and Hard Armor Applications. *Int. SAMPE Tech. Conf.* 23, Kiamesha Lake, NY, **1991** Oct. 21-24:651-657

20. Bless SJ, Benyami M, Hartman D. Penetration through Glass-Reinforced Phenolic. *Advanced Materials: Looking Ahead to the 21 st Century*. **1990**:293-303.

21. Evans E, Ritchie K. Dynamic Strength of Molecular Adhesion Bonds. *Biophys J* **1997**;72(4):1541-1555

22. Zhou, H.; Attard, T. L. Rehabilitation and Strength Sustainability of Fatigue Damaged Concrete–encased Steel Flexural Members Using a Newly Developed Polymeric Carbon–fiber Composite. *Composites Part B: Engineering* **2013**, 45, 1091–1103.

23. Dhiradhamvit, K., and Attard, T. L. Sustainable Energy Dissipation and Evolutionary Viscous Damping in Wood-Frame Structures Proc.*1st Intl Conf on Construction, Architecture and Engineering*, Athens, Greece, **2011** June 20, 21.

24. Attard, T. L. and Dhiradhamvit, K. Development of a New Lightweight ‘Rubberized-Carbon’ Composite for New or Already-Damaged Structures Proc. *Near-Collapse Buildings Conference and Workshop*, Texas A&M University, **2010** April 28-29.

25. Sun, W.; Wu, H.; Tan, X.; Kessler, M. R.; Bowler, N. Silanized-Silicon/Epoxy

Nanocomposites for Structural Capacitors with Enhanced Electrical Energy Storage Capability. *Composites Science and Technology* **2015**, 121, 34–40.

26. Visconti, S.; Marchessault, R. H. Small Angle Light Scattering by Elastomer-Reinforced Epoxy Resins. *Macromolecules*, **1974**, 7, 913–917.

27. Xiao, K.; Ye, L. Effects of Rubber-Rich Domains and the Rubber-Plasticized Matrix on the Fracture Behavior of Liquid Rubber-Modified Araldite-F Epoxies. *Polymer Engineering & Science*, **2000**, 40, 2288–2298.

28. Zhang, K.; Wang, L.; Wang, F.; Wang, G.; Li, Z. Preparation and Characterization of Modified-Clay-Reinforced and Toughened Epoxy-Resin Nanocomposites. *Journal of Applied Polymer Science*, **2003**, 91, 2649–2652.

29. Liu, T.; Tjiu, W. C.; Tong, Y.; He, C.; Goh, S. S.; Chung, T.-S. Morphology and Fracture Behavior of Intercalated Epoxy/Clay Nanocomposites. *Journal of Applied Polymer Science*, **2004**, 94, 1236–1244.

30. Zhang, X.-H.; Zhang, Z.-H.; Xu, W.-J.; Chen, F.-C.; Deng, J.-R.; Deng, X. Toughening of Cycloaliphatic Epoxy Resin by Multiwalled Carbon Nanotubes. *Journal of Applied Polymer Science*, **2008**, 110, 1351–1357.

31. Hillmyer, M. A.; Lipic, P. M.; Hajduk, D. A.; Almdal, K.; Bates, F. S. Self-Assembly and Polymerization of Epoxy Resin-Amphiphilic Block Copolymer Nanocomposites. *Journal of the American Chemical Society*, **1997**, 119, 2749–2750.

32. Grubbs, R. B.; Dean, J. M.; Broz, M. E.; Bates, F. S. Reactive Block Copolymers for Modification of Thermosetting Epoxy. *Macromolecules*, **2000**, 33, 9522–9534.

33. Li, T.; He, S.; Stein, A.; Francis, L. F.; Bates, F. S. Synergistic Toughening of Epoxy Modified by Graphene and Block Copolymer Micelles. *Macromolecules*, **2016**, 49, 9507–9520.

34. Hassan, T.; Rizkalla, S. Investigation of Bond in Concrete Structures Strengthened with Near Surface Mounted Carbon Fiber Reinforced Polymer Strips. *Journal of Composites for Construction* **2003**, 7, 248–257.

35. Aidoo, J.; Harries, K. A.; Petrou, M. F. Fatigue Behavior of Carbon Fiber Reinforced Polymer-Strengthened Reinforced Concrete Bridge Girders. *Journal of Composites for Construction* **2004**, 8, 501–509.

36. Wang, Y. T.; Wang, C. S.; Yin, H. Y.; Wang, L. L.; Xie, H. F.; Cheng, R. S. Carboxyl-Terminated Butadiene-Acrylonitrile-Toughened Epoxy/Carboxyl-Modified Carbon Nanotube Nanocomposites: *Thermal and Mechanical Properties*. *Express Polymer Letters*, **2012**, 6, 719–728.

37. Liu, J., Sue, H.J., Thompson, Z.J., Bates, F.S., Dettloff, M., Jacob, G., Verghese, N., Pham, H. Nanocavitation in Self-assembled Amphiphilic Block Copolymer-modified

Epoxy, *Macromolecules*; **2008**, 41, 7616–7624.

38. Wu, J., Thio, Y.S., Bates, F.S. Structure and Properties of PBO-PEO Diblock Copolymer Modified Epoxy, *Journal of Polymer Science Part B: Polymer Physics*. **2005**, 43, 1950–1965.

39. Inoue T, Narihisa Y, Katashima T, Kawasaki S, Tada T. A Rheo-Optical Study on Reinforcement Effect of Silica Particle Filled Rubber. *Macromolecules*. **2017** Oct 4;50(20):8072-8082.

40. Jaffel H, Korb JP, Ndobu-Epo JP, Guicquero JP, Morin V. Multi-Scale Approach Continuously Relating the Microstructure and the Macroscopic Mechanical Properties of Plaster Pastes during Their Settings. *The Journal of Physical Chemistry B*. **2006** Sep 21;110(37):18401-18407.

41. Boek ES, Wilson AD, Padding JT, Headen TF, Crawshaw JP. Multi-scale Simulation and Experimental Studies of Asphaltene Aggregation and Deposition in Capillary Flow. *Energy & fuels*. **2009** Dec 21;24(4):2361-2368.

42. Sundararaghavan V, Zabarar N. A Multi-Length Scale Sensitivity Analysis for The Control of Texture-Dependent Properties in Deformation Processing. *International Journal of Plasticity*, **2008**, 24(9):1581-1605.

43. Leventis, N., Sotiriou-Leventis, C., Zhang, G., & Rawashdeh, A. M. M.. Nanoengineering Strong Silica Aerogels. *Nano letters*. **2002**; 2(9), 957-960.

44. Leventis, N. Three-dimensional Core-shell Superstructures: Mechanically Strong Aerogels. *Accounts of chemical research*. **2007**; 40(9),874-884.

45. Leventis, N. and Lu, H.. Polymer-crosslinked Aerogels. *In Aerogels Handbook*, Springer, New York, NY.**2011**. (251-285).

46. Leventis, N., Sotiriou-Leventis C, Mulik S, Dass A, Schnobrich J, Hobbs A, Fabrizio EF, Luo H, Churu G, Zhang Y, Lu H. Polymer nanoencapsulated mesoporous vanadia with unusual ductility at cryogenic temperatures. *Journal of Materials Chemistry*. **2008**;18(21):2475-2482.

47. Zhang, G., Dass, A., Rawashdeh, A.M.M., Thomas, J., Counsil, J.A., Sotiriou-Leventis, C., Fabrizio, E.F., Ilhan, F., Vassilaras, P., Scheiman, D.A. and McCorkle, L., Isocyanate-crosslinked silica aerogel monoliths: preparation and characterization. *Journal of Non-Crystalline Solids*, **2004**. 350, pp.152-164.

48. Ilhan, F., Fabrizio, E.F., McCorkle, L., Scheiman, D.A., Dass, A., Palczar, A., Meador, M.B., Johnston, J.C. and Leventis, N., Hydrophobic Monolithic Aerogels by Nanocasting Polystyrene on Amine-modified Silica. *Journal of Materials Chemistry*, **2006**.16(29):3046-3054.

49. Meador, M.A.B., Fabrizio, E.F., Ilhan, F., Dass, A., Zhang, G., Vassilaras, P., Johnston,

J.C. and Leventis, N., Cross-linking amine-modified Silica Aerogels with Epoxies: Mechanically Strong Lightweight Porous Materials. *Chemistry of Materials*, **2005**, 17(5): 1085-1098.

50. Buchmeiser, M.R., Sinner, F., Mupa, M. and Wurst, K., Ring-opening Metathesis Polymerization for the Preparation of Surface-grafted Polymer Supports. *Macromolecules*, **2000**; 33(1): 32-39.

51. Mohite, D.P., Larimore, Z.J., Lu, H., Mang, J.T., Sotiriou-Leventis, C. and Leventis, N., Monolithic Hierarchical Fractal Assemblies of Silica Nanoparticles Cross-linked with Polynorbornene via ROMP: a Structure–property Correlation from Molecular to Bulk through Nano. *Chemistry of materials*, **2012**; 24(17): 3434-3448.

52. Yang, K.; Wu, S.; Guan, J.; Shao, Z.; Ritchie, R. O. Enhancing the Mechanical Toughness of Epoxy-Resin Composites Using Natural Silk Reinforcements. *Scientific Reports*. **2017**, 7(1): 11939.

53. Demir B, Henderson LC, Walsh TR. Design Rules for Enhanced Interfacial Shear Response in Functionalized Carbon Fiber Epoxy Composites. *ACS applied materials & interfaces*. **2017** Mar 27; 9(13):11846-57.

54. Chang, Raymond. Chemistry 10th Edition. *JA KUBU*, **2010**.

55. Brandrup J, Immergut EH, Grulke EA, Abe A, Bloch DR, editors. Polymer handbook(Vol. 89). *New York: Wiley*; 1999 Feb.

56. Yates CR, Hayes W. Synthesis and Applications of Hyperbranched Polymers. *European Polymer Journal*. 2004 Jul 1;40(7):1257-1281.

57. Ramin MA, Le Bourdon G, Heuzé K, Degueil M, Buffeteau T, Bennetau B, Vellutini L. Epoxy-Terminated Self-Assembled Monolayers Containing Internal Urea or Amide Groups. *Langmuir*. **2015** Feb 24;31(9):2783-2789.

58. Zumdahl S. S.; Zumdahl S. A.; Chemistry (5th edition), Houghton Mifflin College Div, 2004.

59. Ying, H.; Cheng, J. Hydrolyzable Polyureas Bearing Hindered Urea Bonds. *Journal of the American Chemical Society* **2014**, 136, 16974–16977.

60. González, M. G.; Cabanelas, J. C.; Baselga, J. Applications of FTIR on Epoxy Resins - Identification, Monitoring the Curing Process, Phase Separation and Water Uptake. *In Infrared Spectroscopy - Materials Science, Engineering and Technology*; InTechOpen, **2012**.

61. Chowdhury, R. A.; Hosur, M. V.; Nuruddin, M.; Tcherbi-Narteh, A.; Kumar, A.; Boddu, V.; Jeelani, S. Self-Healing Epoxy Composites: Preparation, Characterization and Healing Performance. *Journal of Materials Research and Technology* **2015**, 4, 33–43.

62. Wang, S.-K.; Sung, C. S. P. Fluorescence and IR Characterization of Cure in Polyurea, Polyurethane, and Polyurethane–Urea. *Macromolecules* **2002**, 35, 883–888.
63. Gao C, Jin YZ, Kong H, Whitby RL, Acquah SF, Chen GY, Qian H, Hartschuh A, Silva SR, Henley S, Fearon P. Polyurea-functionalized Multiwalled Carbon Nanotubes: Synthesis, Morphology, and Raman Spectroscopy. *The Journal of Physical Chemistry B*. **2005** Jun 23;109(24):11925-11932.
64. File No: PLC/266, Full public report, Polymer in Technologic Varnish 84FI400, *Chemicals Notification and Assessment*, November **2001**.
65. Attard, T.L., and Zhou, H. Damage Absorption of High-Impact Structural Systems using Time-Reaction of Hybridized Epoxy-Polyurea Interfaces,” *Athens Journal of Technology & Engineering*, **2016**; 3(1); 71-88

SUPPORTING INFORMATION

Materials and Methods

IEPM Synthesis. This study focuses on a time-point to apply polyurea to curing epoxy (t_c), utilizing fast-curing non-catalytic two-part aliphatic polyurea (FSS42D Part A: Isophorone Diisocyanate (IPDI) reacts with Polyoxypropylene Diamine; FSS42D Part B (resin): Diamine) - purchased from Versaflex Incorporated, USA - and a low-viscosity epoxy (544 cps) - Bisphenol A Diglycidyl ether (*DGEBA*) epoxy resin (LAM-125 resin) and LAM-226 polyamine hardener - purchased from Pro-Set Inc., USA. In the ballistics testing, we examined two-component aliphatic polyurea and aromatic polyurea, where Part A of the latter was comprised of Methylene Diisocyanate (*MDI*) and Polyether Polyol. Epoxy resin and NH_2 -based hardener were mixed by a volume ratio of 3:1 at room temperature. Effects of epoxy viscosity on *IEPM* were studied by synthesizing *IEPM* using $t_c=0.5$ h and $t_c=2.5$ h with a higher-viscosity epoxy (1,367 cps): LAM-135 resin and 226 hardener. Various combinations of potential chemical reactions are shown in Table S1. Figure S1 depicts a suggested reaction based on the high reaction rate of Reaction 2 and because we found single nanoscale locations to consistently feature both polyurea and epoxy peaks. In the construction of *C-IEPM-b- t_c* panels, carbon fiber sheets (2x2 Twill architecture, 5.78 oz / yd², 550 ksi tensile strength, 0.33 mm fiber thickness) were purchased from ACP Composites, Inc., USA.

Table S1

Possible *IEPM* chemical reactions: curing epoxy / polyurea (pre-polymerized)

Reaction number	Polyurea component	Epoxy component	Reactions being tested	Preliminary Observations	Discussion/ Explanation
1	Part A (diisocyanate)	Resin (DGEBA)	-NCO epoxide	+ No reaction	N/A

			-NCO + -OH		
2	Part A (diisocyanate)	Hardener (polyamine)	-NCO + -NH ₂ (epoxy hardener)	Solidifies in seconds after mixing	-NCO + -NH ₂ rapid reaction
3	Part B (polyamine)	Resin (DGEBA)	Epoxide + - NH ₂ (polyurea part B)	Mixed, no reaction after 24 hours	Additives in epoxy part B accelerate the reaction of epoxide + NH ₂
4	Part A (diisocyanate)	Curing epoxy (3:1 ratio resin: hardener)	-NCO + -NH ₂ (epoxy hardener) at the interface	-NCO on the top, still liquid after 24 hours	Possible -NCO + NH ₂ / - NCO + epoxide reaction at the interface, but no reaction in top layer - NCO
5	Part A (diisocyanate)	Curing epoxy (2:1 ratio resin: hardener)	-NCO + -NH ₂ (epoxy hardener) at the interface	-NCO on the top, still liquid after 24 hours	Possible -NCO + NH ₂ / - NCO + epoxide reaction at the interface, but no reaction in top layer - NCO

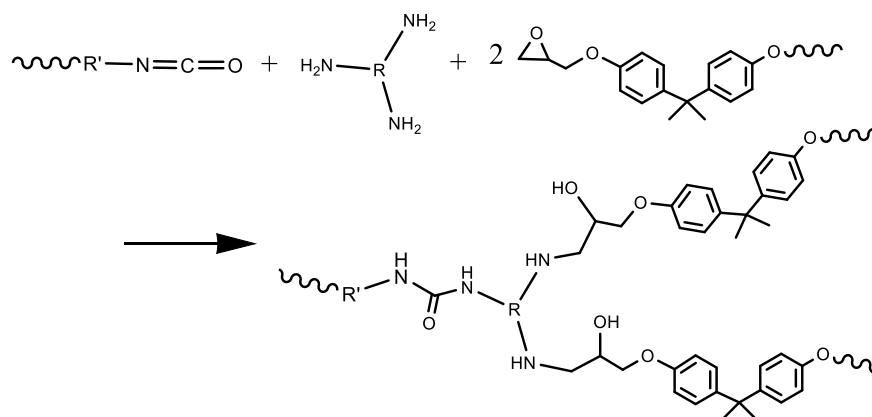


Figure S1. Schematic of suggested reaction, where formation of chemical bonding within the *IEPM* (interface) consists of the three-part reaction: (epoxide) + (amine epoxy hardener) + (isocyanate)

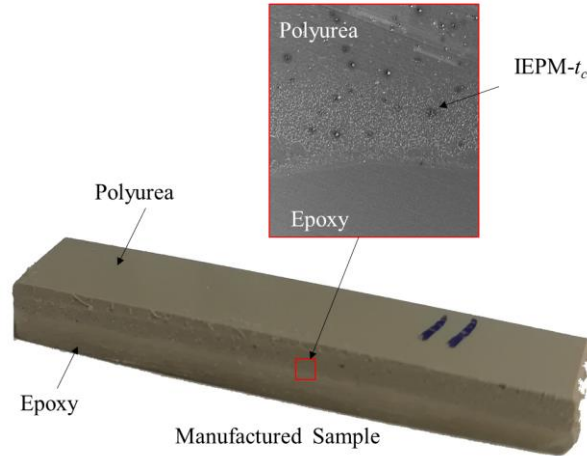


Figure S2. Manufactured 0-IEPM- t_c sample and SEM image of 0-IEPM- t_c

IEPM is a reaction between epoxy and pre-polymerized fast-curing polyurea. Multiple elapsed curing times of epoxy resin (t_c) were selected as time-points (0 h, 0.5 h, 1 h, 1.5 h, 2.5 h, 3.5 h, and 24 h) to spray polyurea on curing epoxy. Figure S2 shows one of the manufactured samples and its SEM image of IEPM. For C-IEPM- t_c fabrication, carbon (C) fiber sheets were immersed in epoxy mixture. For 0-IEPM- t_c fabrication (“x” is 0), the just-mixed epoxy mixture ($t_c=0$), signifying commencing of curing, was poured onto a substrate as the bottom layer. Polyurea was then applied onto curing epoxy at 70 °C using a polyurea spray machine (Reactor E-10, Graco Inc., USA) with a high-pressure spray gun (at 1000 psi and 70 °C). At the conclusion of the spray process, specimens remained in a curing state for 24 h before being cut (via electric table saw) and tested under mechanical loading (*DMA* and up to .44 magnum ballistics testing). The specimens were named in accordance to type of fiber (“x”) that was used and t_c , see Table S2. Specimens that utilized LAM 135 / 226 were designated as C-*IEPM*-0.5v and C-*IEPM*-2.5v. Specimens that were constructed as ballistics panels were designated as x-*IEPM*-b- t_c (b = ballistics) and were manufactured as follows: Using two wood-constructed frames as support-structures, two

groups of five fiber sheets were individually epoxied. The last layer was sprayed with polyurea, engendering “inner” *IEPM* reaction; the back-side of the first layer was not sprayed. Aromatic and aliphatic polyurea cures after approximately 10 sec and 90 sec, per manufacturer recommendation. Five additional fiber layers, intermittently epoxied, were applied to the two cured polyurea surfaces. The last layer was sprayed with polyurea, engendering “outer” *IEPM* reaction at approximately $t_c = 2.5$ h. The two "inner-outer" half-panels were epoxied together, back-fiber-side to back-fiber-side. The four-layer panel was removed from its adjoined wood frame.

Table S2

Specimen names and corresponding parameters

Specimen Name	t_c (hr)	IEPM Width (μm)	Fiber Type (‘x’)
0-IEPM-0	0	50	0
0-IEPM-0.5	0.5	30	0
0-IEPM-1	1	10	0
0-IEPM-1.5	1.5	< 2	0
0-IEPM-2.5	2.5	< 2	0
0-IEPM-3.5	3.5	< 2	0
0-IEPM-24	24	0	0
C-IEPM-0.5V	0.5	< 10	C (Carbon), 2-layer
C-IEPM-2.5V	2.5	< 2	C(2-layer)
C-IEPM-0	0		C(2-layer)
C-IEPM-0.5	0.5		C(2-layer)
C-IEPM-1	1		C(2-layer)
C-IEPM-1.5	1.5		C(2-layer)
C-IEPM-2.5	2.5		C(2-layer)
C-IEPM-3.5	3.5		C(2-layer)
C-IEPM-24	24		C(2-layer)
C-IEPM-b- t_c	t_c varies		C(4-layer/2-layer)

Characterization. Scanning electron microscopy (*SEM*), (Zeiss, USA), was implemented to observe the fracture surfaces of x-HMC / *IEPM*- t_c cross sections to study the thickness and morphology of interface. Atomic force microscope (*AFM*) and nano-

Infrared Spectroscopy (nano-IR) were carried out to study the morphology and chemical composition of the interface area respectively (Nano-IR2, Anasys Instruments, USA). All *AFM* and nano-IR measurements were carried out in contact mode using commercially available Au coated Si cantilevers with a nominal resonance frequency of 13 ± 4 kHz, spring constant of 0.07-0.04 N/m, and 50 nm radius of curvature. Prior to nano-IR characterization, the specimens were trimmed and cut to a dimension of 1mm by 1mm by 200 nm using Microtome (Zeiss, USA).

Mechanical properties of six *x-HMC/ IEPM-t_c* specimens, see Table S3, were measured using Dynamic Mechanical Analyzer (*DMA*). Bar specimens were cut to size 30 mm by 7 mm and tested in single cantilever mode at room temperature using a RSA-G2 Solids Analyzer instrument (USA). In order to identify *IEPM* properties, we effectively isolated *IEPM* in each *0-IEPM-t_c* specimen via multi-layered parallel Generalized Maxwell Model (epoxy, polyurea, and *IEPM*). Using measured DMA results for pure polyurea and pure epoxy, shown in Figure S3, we normalized test results according to a Thickness Factor, *m*, using each sample's thickness and the maximum thickness of the group of six samples, to account for experimental variation¹.

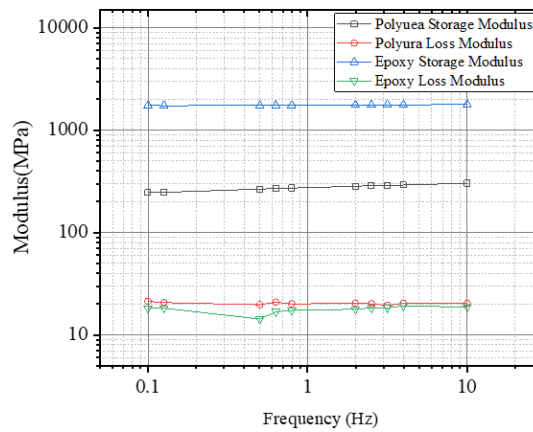


Figure S3. DMA results of pure polyurea and pure epoxy, Set-up of Test Program B, including wood-constructed support structure, chronograph, and *C-IEPM-b-t_c* test panel

Microtoming reveals Shifting of nano-IR Spectra Peaks

The 1090 cm^{-1} absorption peak shifts to 1115 cm^{-1} in *0-IEPM-2.5*, see Figure 2(i), which could be explained by weak hydrogen bonding with absorbed water during the microtome process. However, since nano-IR point spectra were not collected on the “black holes” in Figure 2(h), this does not appear to be the case. Furthermore, the 1090 cm^{-1} peak was not observed to shift in *0-IEPM-0* Figures 1(d) and 1(e), *0-IEPM-0.5* Figure 2(c), and *0-IEPM-1*, see Figure 2(f).

Non-Negative Matrix Factorization (NMF). A line of 100 points was selected to perform nano-IR spectral analyses from pure-epoxy region, across the *IEPM*, to pure-polyurea region for all *x-IEPM- t_c* specimens. We rearranged the nano-IR spectra of all points per *IEPM* to form a nano-IR spectra matrix **V** and used Non-Negative Matrix Factorization (*NMF*) to de-convolute the spectra using matrix **W** (wave number spectra) and intensity matrix **H** by $V = W \times H$. All three matrices have no negative elements. Each vector in **W** is a de-convoluted vector of a single IR spectrum along the line of nano-IR scanning points. We de-convoluted, i.e., statistically decompiled, the original non-normalized IR data into 6 Vectors, i.e., a combination of the 6 Vectors would result in the original “convoluted” spectra; six Vectors provided sufficient statistical insight into the chemical bonding as a function of t_c .

Ballistics-Resistant Panels.

The National Institute of Justice² defines panel failure as full perforation by projectile per minimum initial projectile velocity.³ Passing is quantified using 'back face signature,' or greatest extent of indentation in the backing material, caused by the non-

perforating impact on armor. In our study, x - $IEPM$ - b - t_c ballistics panels (thickness: 1.25 cm to 1.91 cm; 0.5 in to 0.75 in) were manufactured using 'hand lay-up' procedure. Each panel consisted of either four layers of $IEPM$ or two layers of $IEPM$ using combinations of t_c , polyurea type (aliphatic or aromatic), and epoxy-resin (low or medium viscosity). Each four-layer $IEPM$ panel contained 20 layers of carbon fiber. Each panel was subjected to five calibers: .22LR (long rifle), 9mm Luger, .45Auto/ ACP, .357 Magnum, and .44 Magnum, Table S3. An additional two test programs (A and B for different epoxy-resin viscosity) were also used to check repeatability of results and to confirm correlation between lower t_c on nanostructures and ballistics resistance. Test program B used chronograph (RCBS AmmoMaster Chronograph[®]), placed at ten (10) feet from test panel, to measure the approach impact velocity of cartridges that were fired at twenty (20) feet. Our typical test set-up is shown in Figure S4.

Table S3

Five caliber-rated bullets used for ballistics-impact testing on x - $IEPM$ - b - t_c

Ballistics Brand	Table	Caliber	Bullet Weight (grain)	Bullet Type	Rated Muzzle Velocity (fps)	Rated Muzzle Energy (ft-lbs)
Federal		.22 LR	40	Lead round nose	1200	130
Remington UMC		9mm Luger	115	FMJ	1145	335
CCI Blazer		.45 Auto	230	FMJ	845	365
CCI Blazer Brass		.357 magnum	158	JHP	1250	548
Remington UMC		.44 magnum	180	JSP	1610	1036



Figure S4. Set-up of Test Program B, including wood-constructed support structure, chronograph, and $C\text{-IEPM-}b\text{-}t_c$ test panel

Reference

1. Lee-Sullivan P, Dykeman D. Guidelines for performing storage modulus measurements using the TA Instruments DMA 2980 three-point bend mode: I. Amplitude effects1. *Polymer Testing*. **2000** Apr 1;19(2):155-64.
2. Armor PB. Ballistic Resistance of Personal Body Armor NIJ Standard–0101.04. **2008**
3. Abrate S. Impact on Composite Structures. *Cambridge university press*; **2005** Aug 22.

CONCLUSIONS

An experimental testing program was developed to analyze six connection-detail design schemes in coastal bridges, to ascertain their structural integrity and plausibility of reduce each girder's susceptibility to local cracking during major hurricane events. The test-bed for each test girder included a periodic wave-force function, consisting of simultaneous surge (vertical / hydrostatic) and wave (lateral and vertical / hydrodynamic) forces in accordance with the existing I-10 bay-way AASHTO bridges in Mobile, Alabama. The six, single-span Test Girders (TG, $\frac{1}{4}$ scale) were designed using the following connection-details: (1) 'Pre-Katrina,' or 'as-is' mechanical connections prior to the 2005 Hurricane Katrina event; (2) 'Post-Katrina,' utilizing through-bolt threaded anchors for the concrete girders; (3) conventional carbon-fiber reinforced epoxy (CF/E)-wrapped connection-details that included pre-Katrina-designed mechanical connections; and (4) – (6) Carbon-fiber Interfacial Epoxy-Polyurea Matrix (C-IEPM) at different t_c (2.5 hr and 1.5 hr) applied to zero, one, or two girder-ends eliciting different boundary conditions, with or without existing pre-Katrina-designed mechanical connections.

C-IEPM is a new composite based on the modification of traditional CF/E, where IEPM interfacial film was annexed to CF/E via chemical reaction between curing epoxy and polyurea moieties. A calculated Hurricane Katrina wave function was dynamically applied to the six test girders. Pre-Katrina TG, Post-Katrina TG, and C-IEPM_0 TG connection-details failed after approximately one-half of the load cycle duration; within 0.5 sec after the initial shear failure of the connection-details, the girders severed from their

respective cap-beams. Although C-IEPM_1 TG exhibited about 2.5 to 3 times greater strength than Pre-Katrina TG, Post-Katrina TG, and C-IEPM_0 TG, C-IEPM_1 TG also failed in less than one full load cycle.

Although the connection-details in C-IEPM_2 TG and CF/E TG were able to achieve the maximum wave load (160.1 kN), CF/ E TG was deemed to have effectively failed during cycle No. 1 as it was unable to recover, or re-achieve, the maximum force during the load plateauing stage and experienced excessive damage, including fiber breakage. However, because of an aggrandized quantity of fiber and re-orientation of materials axes, the reserve strength and deflection recovery helped the girder recover a portion of the energy during subsequent loading cycles until catastrophically detaching from its cap-beam supports. Conversely, C-IEPM, formulated with a reaction between epoxy and polyurea moieties to engender a high-quality IEPM, infused significant material damping via damping ratio of 4.87% (versus 1.18% for CF/E) to the connection, therefore limiting the damage of the girder to local cracking after 12 wave-load cycles. The final conclusions of the study are summarized as follows:

- CF/E TG is unable to dissipate sufficient energy per loading cycle, experiencing significant girder rotation and fiber delamination. As the damage accumulated, the force-deflection hysteresis remained transient until the girder catastrophically failed
- C-IEPM_2 TG provides sufficient energy dissipation and fracture toughness (fracture energy), thus localizing damage to the fiber, matrix, and concrete in the connection. The anelastic behavior of the connection and hyperelastic response of the girder help to stabilize its hysteresis after load cycle No. 3 or load cycle No. 4,

characterizing its survival. After 12 load cycles, C-IEPM_2 TG experienced only localized damage.

- A Generalized Maxwell Model is constructed using DMA experimental data, which accurately expresses the epoxy, polyurea and IEPM properties.
- A parallel epoxy/ IEPM and polyurea system conservatively computes the IEPM's progenerated viscoelasticity.
- Epoxy curing time (t_c) has a large influence on the loss modulus contribution by IEPM which enhances energy transferability in x-IEPM composite. Lower values of t_c institute enhanced material damping and bond strength between epoxy (which provides stress-transferring paths for CF/E) and polyurea. Curing time (t_c) is recommended less than 2 hours, considering the construction time, if C-IEPM is used for onsite construction for the connection of the bridge connections,
- In IEPM designed with small t_c , there is strong presence of chemical bond richness that improves interface cohesion (bond enthalpy) and reduces *IEPM* defects. Across IEPM width, a three-part reaction between (epoxide) + (amine epoxy hardener) + (isocyanate) introduces critical urea bonds to the epoxy system, via chemical bonding, engendering desirable molecular vibrational properties, specifically C-C stretching, C=C stretching of aromatic rings, N-H bending, C-N stretching, and broad urea carbonyl stretching bonds at single nanoscale points. The chemistry of IEPM nanostructures, supported via statistics of NMF analysis of the IR spectra data and also physically by the tip-size of the nano-IR laser tip (80 nm) which is smaller than polyurea or epoxy molecule size, correlates well to bulk material properties, such as loss modulus, which shows 100% increase for IEPM-

$t_c=0$ relative to IEPM- $t_c=0.5$, and glass transition temperature (and IEPM re-generativity), per x -IEPM- t_c design.

C-IEPM is a viable option for minimizing bridge-damage under extreme coastal hurricane forces. Requiring a minimal quantity of carbon-fiber, C-IEPM minimizes damages due to hurricane induced loads to local cracking, thereby potentially extending the life-span of vulnerable coastal bridges.

LIMITATION OF THE RESEARCH

The study shows that C-IEPM has good potential for application in the strengthening of bridge connections against hurricane-induced wave and surge load. However, there are still some limitations in the presented study.

The $\frac{1}{4}$ scale girder cannot fully represent the prototype. Further analyses need to be done with full-size specimens or entire bridge spans. The real dynamic hurricane wave loads impact angle and location are unpredictable. Though the simulated hurricane wave load in the lab considered the wave load's period, it is still a quasi-static loading that aims to represent realistic maximum forces to which the connection will be subjected.

For the presented strengthening method using CFRP (CF/E and C-IEPM) wrapping the as-is mechanical connections is a good concept. But this wrapping method is not practical in the field because the span-to-span gap is too small to permit wrapping the girder ends. Also, due to limitations of testing time and availability, the wrapping method is not fully optimized.

All research conducted in the lab and did not consider the on-site environmental influence. How to control the epoxy curing time and environmental temperature is a question that needs to be solved, but was not an objective of this research. Environmental factors like wind and sunlight will also influence the manufacture, and deserve further study with regard to C-IEPM. The interface study is based on the matrix sample. The presence of fibers needs to be considered for further study, since the the presence of fibers will likely influence the mixing of epoxy and polyurea in the interface zone.

LIST OF GENERAL REFERENCES

- [1] Padgett J, DesRoches R, Nielson B, Yashinsky M, Kwon OS, Burdette N, Tavera E. Bridge damage and repair costs from Hurricane Katrina. *Journal of Bridge Engineering*. 2008 Jan;13(1):6-14.
- [2] Office of Coastal Management, National Oceanic and Atmospheric Administration (NOAA); 2018. <https://coast.noaa.gov/states/fast-facts/hurricane-costs.html>
- [3] National Institute of Building Science, Natural Hazard Mitigation Saves Study, 2019 <https://www.nibs.org/page/mitigationsaves>
- [4] Padgett JE, Spiller A, Arnold C. Statistical analysis of coastal bridge vulnerability based on empirical evidence from Hurricane Katrina. *Structure and infrastructure engineering*. 2012 Jun 1;8(6):595-605.
- [5] Douglass, S. L., Chen, Q. J., Olsen, J. M., Edge, B. L., and Brown, D. (2006). "Wave force on bridge decks," Final Rep., Prepared for U.S. DOT, Federal Highway Administration (FHWA), Office of Bridge Technology, Washington, DC.
- [6] Tanaka Y, Kawano H, Watanabe H, Nakajo T. Study on cover depth for prestressed concrete bridges in airborne-chloride environments. *PCI Journal*. 2006 Mar 1;51(2):42.
- [7] Kettl DJ. On risk and disaster: Lessons from Hurricane Katrina. University of Pennsylvania Press; 2006 Jan 9.
- [8] Stearns M, Padgett JE. Impact of 2008 Hurricane Ike on bridge infrastructure in the Houston/Galveston region. *Journal of Performance of Constructed Facilities*. 2011 Feb 11;26(4):441-52.
- [9] https://www.fox10tv.com/news/mobile_river_bridge_and_bayway/aldot-presents-plan-for-i--bridge-and-bayway-tolls/article_392a9af2-a8a8-11e9-9eca-4797f84bab03.html
- [10] G. Ed Ramey Alvin Sawyer, III Joel G. Melville, Hurricane surge surface wave forces on deck-girder bridges and design and retrofit options for these bridges, 2008, <http://www.eng.auburn.edu/files/centers/hrc/930-687.pdf>
- [11] Bradner C, Schumacher T, Cox D, Higgins C. Experimental setup for a large-scale bridge superstructure model subjected to waves. *Journal of waterway, port, coastal, and ocean engineering*. 2010 May 13;137(1):3-11.

- [12] Do TQ, van de Lindt JW, Cox DT. Performance-based design methodology for inundated elevated coastal structures subjected to wave load. *Engineering structures*. 2016 Jun 15;117:250-62.
- [13] Cai Y, Agrawal A, Qu K, Tang HS. Numerical investigation of connection forces of a coastal bridge deck impacted by solitary waves. *Journal of Bridge Engineering*. 2017 Oct 18;23(1):04017108.
- [14] Robertson IN, Yim S, Tran T. Case study of concrete bridge subjected to hurricane storm surge and wave action. *Solutions to Coastal Disasters 2011* 2011 (pp. 728-739).
- [15] Lehrman JB, Higgins C, Cox D. Performance of highway bridge girder anchorages under simulated hurricane wave induced loads. *Journal of Bridge Engineering*. 2011 Apr 25;17(2):259-71.
- [16] Sea Level Rise and Storm Surge Impacts on a Coastal Bridge:I-10 Bayway, Mobile Bay, Alabama, 2016,
https://www.fhwa.dot.gov/environment/sustainability/resilience/ongoing_and_current_research/teacr/index.cfm
- [17] Yuan P, Xu G, Chen Q, Cai CS. Framework of practical performance evaluation and concept of interface design for bridge deck–wave interaction. *Journal of Bridge Engineering*. 2018 May 11;23(7):04018048.
- [18] Tekalur SA, Shukla A, Shivakumar K. Blast resistance of polyurea based layered composite materials. *Composite Structures*. 2008 Jul 1;84(3):271-81.
- [19] Zhou H, Attard TL, Wang Y, Wang JA, Ren F. Rehabilitation of notch damaged steel beams using a carbon fiber reinforced hybrid polymeric-matrix composite. *Composite Structures*. 2013 Dec 1;106:690-702.

APPENDIX: MODIFIED DOUGLASS FUNCTION

Based on the maximum hurricane-induced, the wave elevation information. The maximum hurricane wave loads could be estimated using modified Douglass function.

Estimated Wave Forces on I-10 Bridge During Mock Hurricane Katrina, Case C

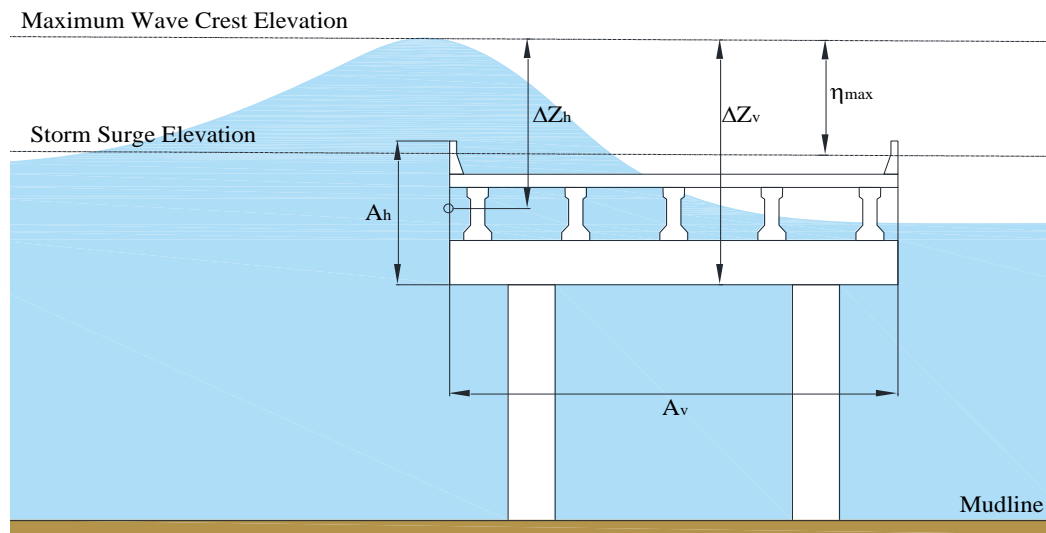


Figure A1. Modified Douglass Function definition

First step: the assumption of sea state

$$\text{MSL} = 0.00'$$

$$\text{Mudline} = -5.00'$$

$$21.50' \text{ Storm Surge}$$

$$8.80' \text{ Significant Wave Height}$$

$$\text{Elevation of Centroid of Deck} = 20.62' \text{ (3.5' Above Top of Cap)}$$

Second step (key): calculating wave forces using Modified Douglass equation

Calculations:

$$\eta_{\max} = 0.78 * (1.4 * 8.80) = 9.61'$$

$$\text{Maximum Wave Crest Elevation} = 21.50' + 9.61' = 31.10'$$

$$A_h = 65' \times 7' = 455 \text{ ft}^2$$

$$A_v = 65' \times (43'/2) = 1397.5 \text{ ft}^2$$

$$\Delta_{zv} = \text{smaller of } 31.10' - 18.12' = 12.98'$$

or

$$24.12' - 18.12' = 6.00'$$

$$\Delta_{zv} = 6.00'$$

$$\Delta_{zh} = \text{smaller of } 31.10' - 20.62' = 10.48'$$

or

$$24.12' - 20.62' = 3.50'$$

$$\Delta_{zh} = 3.50'$$

Vertical Force:

$$F_v = C_v^{mc} F_v^*$$

$$F_v^* = (64 \text{ pcf}) (6.00') (1397.5 \text{ ft}^2) = 536.6 \text{ kips}$$

$$F_v = (1.0) (536.6 \text{ kips}) = 536.6 \text{ kips}$$

Horizontal Force:

$$F_h = \left\{ 1 + C_r \frac{(N-1)}{2} \right\} c_h^{mc} F_h^*$$

$$F_h^* = (64 \text{ pcf}) (3.50') (455 \text{ ft}^2) = 101.9 \text{ kips}$$

$$F_h = [1 + (0.33) ((5-1)/2)] (1.0) (101.9 \text{ kips}) = 169.2 \text{ kips}$$

Overtopping Moment:

*Assume Vertical Force Acts at a Location of $\frac{1}{4}$ Span Width

$$M = F_v \times \frac{1}{4} \text{ Span Width}$$

$$M = (536.6 \text{ kips}) (43\frac{1}{4}) = 5768.9 \text{ kip-ft}$$

These resultant wave forces along with the span DL forces and the combined.

$$F_v = 536.6 \text{ kips}$$

$$F_h = 169.2 \text{ kips}$$

$$M = 5768.9 \text{ kip-ft}$$

Third step: response to a Mock-Katrina Hurricane

Estimated 'DL + Wave' Forces on a Typical Mobile Bay I-10 Span During a Mock-Katrina Hurricane is shown in the following **Figure 3.2**.

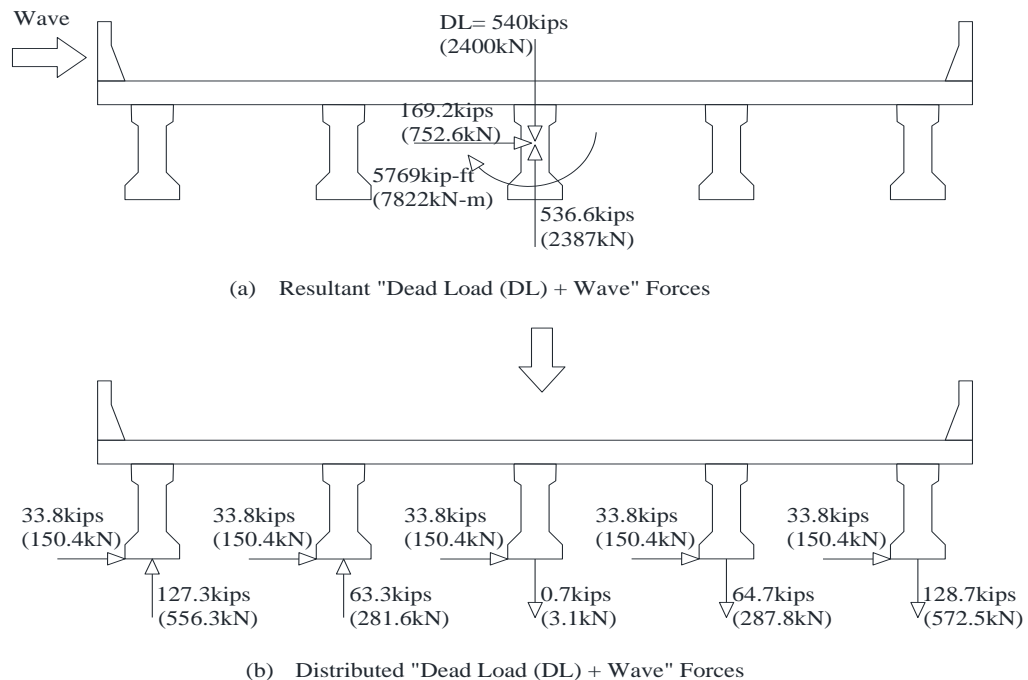


Figure A2. Estimated Wave Forces on I-10 Bridge During Mock Hurricane Katrina, Case C